STARS

Electronic Theses and Dissertations, 2004-2019

2006

Phospholipase A2Mechanism Of Interfacial Activation,An Interdiscliplinary Approach

Kathleen N. Nemec
University of Central Florida

STARS Citation

Showcase of Text, Archives, Research & Scholarship

PHOSPHOLIPASE A2
MECHANISM OF INTERFACIAL ACTIVATION
AN INTERDISCLIPLINARY APPROACH

by

KATHLEEN N NEMEC
B.S. University of Central Florida, 1999

A dissertation submitted in partial fulfillment of the requirements
for the degree of Doctor of Philosophy
in Biomolecular Sciences
in the Burnett College of Biomedical Sciences
at the University of Central Florida
Orlando, Florida

Summer Term
2006

Major Professor: Suren Tatulian

ABSTRACT

Phospholipase A2 (PLA$_2$) is an enzyme that hydrolyzes the *sn*-2-ester bond of membrane phospholipids and liberates arachidonic acid, which is converted to eicosanoids that act as potent mediators of inflammation and allergy. As such this enzyme plays a crucial role in many homeostatic physiological and immunologic processes and disease progression. PLA$_2$s undergo substantial increase in activity upon binding to cellular membranes. This effect of interfacial activation is well recognized, yet its structural and physical aspects are poorly understood. In this work, we have employed the interdisciplinary methods of molecular biology, biochemistry, biophysics, bioinformatics and computational biology, in order to elucidate the structure-function relationships mediating the interfacial activation of human group IIA and group IB PLA$_2$ isoforms. We have evaluated the structural and functional consequences of two conservative, single residue substitutions, located at key membrane-binding and substrate-binding positions of hIIA PLA$_2$. We have also evaluated a human group IB fragment (hIBΔN10), missing the first 10 N-terminal residues which make up the N-terminal alpha helix, as well as a chimeric enzyme substituting the N-terminal alpha helix of hIB PLA$_2$ with that from hIIA PLA$_2$ (hIIA/IB PLA$_2$). We have compared the engineered proteins against both the hIIA and hIB PLA$_2$ native enzymes and their N-terminal peptides, N10-hIB and N10-hIIA, respectively. We have developed and used a novel multidisciplinary approach in order to position the segmentally labeled hIB PLA$_2$ and hIIA/IB chimeric PLA$_2$s at the membrane surface. The results of this work provide significant insight into the understanding of the physical aspects of interfacial activation by determining the precise membrane binding modes of PLA$_2$ isoforms and identifying certain amino acid residues and whole protein segments that play key roles in membrane binding, activation, and involved allosteric conformational effects in PLA$_2$s.

For Earl, Janet and Nick,

and far too many other family and friends

that inspire me to do what I do.

ACKNOWLEDGMENTS

Roman, I couldn't have done it without you, you taught me to think, you encouraged me to fly, you have always been the lift under my airfoil. And ultimately to the One who brought all of you into my life and who will continually bring to me teachers to show me what's important, I am grateful**.**

TABLE OF CONTENTS

LIST OF FIGURES

LIST OF TABLES

LIST OF EQUATIONS

LIST OF ACRONYMS/ABBREVIATIONS

PLA_2	Phospholipase A_2
$shPLA_2$	Homologous secreted isoforms of PLA_2
hIIA PLA_2	Human group IIA Phospholipase A_2
V3W	hIIA PLA_2 mutation with a tryptophan for valine at the #3 position
F5W	hIIA PLA_2 mutation with a tryptophan for phenylalanine at the #5 position
hIB PLA_2	Human group IB Phospholipase A_2
hIBΔN10	Fragment of hIB PLA_2 missing the first 10 N-terminal residues
N10-hIB	Synthetic peptide of the first 10 N-terminal residues of hIB PLA_2
N10-hIIA	Synthetic peptide of the first 10 N-terminal residues of hIIA PLA_2
hIIA/IB	Chimeric PLA_2 composed of the first 10 residues of human group IIA ligated to the hIBΔN10 fragment
pIB PLA_2	Porcine group IB phospholipase A_2
bIB PLA_2	Bovine group IB phospholipase A_2
AppD49	Asp^{49} group IIA isoform from the Eastern Cottonmouth *Agkistrodon piscivorus piscivorus*
LUV	Large Unilamellar Vesicles
POPC	1-palmitoy-2-oleoyl-*sn*-glycero-3-phosphocholine
POPG	1-palmitoy-2-oleoyl-*sn*-glycero-3-phosphoglycerol
DPPC	1,2-dipalmitoyl-*sn*-Glycero-3-Phosphocholine
DPPG	1,2-dipalmitoyl-*sn*-glycero-3-phosphoglycerol
DHTPC	diheptanoyl-thio-phosphatidylcholine
BisPy-PC	1,2,bis-(1-pyrenedecanoyl)-*sn*-glycero-3-phosphocholine

Br$_2$PC	1-palmitoy-2-stearoyl-(n,n+1) dibromo-*sn*-glycero-3-phosphocholine
Py-PE	1,2-dioleoyl-*sn*-glycero-3-phosphoethanolamine-N-(1-pyrenesulfonyl)
FPE	N-(fluorescein-5-thiocarbamoyl)-1,2-dihexadecanoyl-*sn*-glycero-3-phosphoethanolamine
10DN	10-doxylnonadecane
DTNB	5,5'-dithio-bis-(2-nitrobenzoic acid)
TFE	Trifluoroethanol.
RET	Resonance Energy Transfer
CD	Circular Dichroism
FTIR	Fourier Transform Infra-Red spectroscopy
ATR FTIR	Attenuated Total Reflection FTIR
HDX	Hydrogen-Deuterium eXchange
R^{ATR}	Dichroic Ratio
IBS	Interface Binding Surface

CHAPTER ONE: INTRODUCTION

Biological membranes are composed of a fluid lipid bilayer interspersed with the hydrophobic domains of proteins and other biomolecules. The bilayer itself is made up of a combination of glycerophospholipids, sphingolipids, and sterols, with glycerophospholipids as the major component. Glycerophospholipids are amphipathic molecules composed of a glycerol backbone with a polar head group and two hydrocarbon chains. The head group, such as choline, ethanolamine, serine, glycerol, or inositol, is attached through a phosphodiester bond to the *sn-3* position of the glycerol backbone (Figure 1). In mammalian tissues phosphatidylcholine (lecithin) is the predominant membrane phospholipid. In bacteria, the major membrane phospholipid is phosphatidylglycerol. The hydrophobic components of the glycerophospholipid are long chain fatty acids attached by ester bonds at the other two positions of the glycerol backbone. The *sn-1* position is usually occupied by a 16 or 18 carbon, saturated fatty acid or long chain alcohol, attached to the glycerol by either an ester or an ether bond, respectively. The *sn-2* position is usually occupied by an 18 to 20 carbon, unsaturated fatty acid residue linked by an ester bond. Some common fatty acids found in biological membranes are presented in Table 1. Besides serving as a structural component of the bilayer, the glycerophospholipids sequester signal transduction second messengers within their functional groups. Phospholipases A1, A2, C and D participate in signal transduction by cleaving specific ester bonds of the glycerophospholipids releasing unique second messengers. The class of second messenger depends on the type of fatty acid, head group, phosphate or lysophospholipid released. Figure 2 shows the specific ester bonds cleaved and representative hydrolysis products for each of these phospholipases.
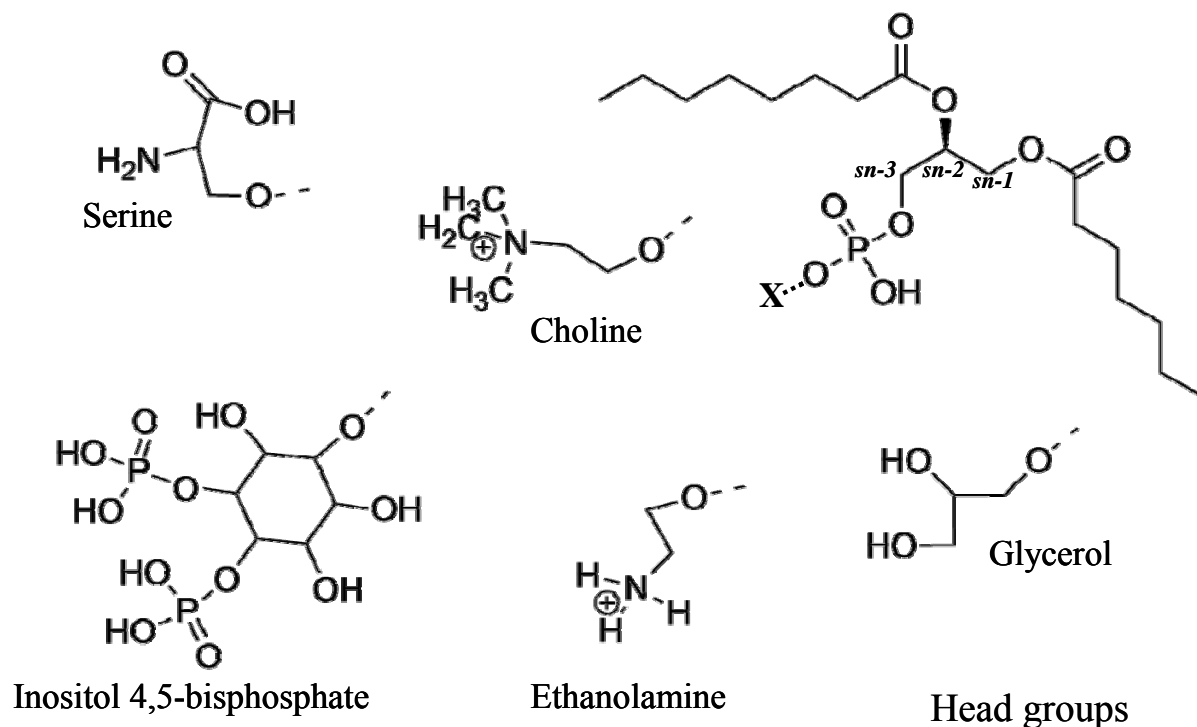
Figure 1 Glycerophospholipids
The head group of the glycerophospholipid (X) determines the overall electrostatic nature of the lipid. Phosphatidyl-choline and -ethanolamine are zwitterionic lipids, -glycerol and -serine are anionic, and -inositol 4,5-bisphosphate has a net charge of -4 at pH 7.

Table 1 Fatty Acids

#Cs	Common Name	Systematic Name	Symbol	Structure
Saturated fatty acids				
12	Lauric acid	Dodecanoic acid	12:0	$CH_3(CH_2)_{10}COOH$
14	Myristic acid	Tetradecanoic acid	14:0	$CH_3(CH_2)_{12}COOH$
16	Palmitic acid	Hexadecanoic acid	16:0	$CH_3(CH_2)_{14}COOH$
18	Stearic acid	Octadecanoic acid	18:0	$CH_3(CH_2)_{16}COOH$
20	Arachidic acid	Eicosanoic acid	20:0	$CH_3(CH_2)_{18}COOH$
22	Behenic acid	Docosanoic acid	22:0	$CH_3(CH_2)_{20}COOH$
24	Lignoceric acid	Tetracosanoic acid	24:0	$CH_3(CH_2)_{22}COOH$
Unsaturated fatty acids (all double bonds are *cis*)				
16	Palmitoleic acid	9-Hexadecenoic acid	16:1	$CH_3(CH_2)_5CH=CH(CH_2)_7COOH$
18	Oleic acid	9-Octadecenoic acid	18:1	$CH_3(CH_2)_7CH=CH(CH_2)_7COOH$
18	Linoleic acid	9,12-Octadecadienoic acid	18:2	$CH_3(CH_2)_4(CH=CHCH_2)_2(CH_2)_6COOH$
18	α-Linolenic acid	9,12,15-Octadecatrienoic acid	18:3	$CH_3CH_2(CH=CHCH_2)_3(CH_2)_6COOH$
18	γ-Linolenic acid	9-Hexadecenoic acid	18:3	$CH_3(CH_2)_4(CH=CHCH_2)_3(CH_2)_3COOH$
20	Arachidonic acid	5,8,11,14-Eicosatetraenoic acid	20:4	$CH_3(CH_2)_4(CH=CHCH_2)_4(CH2)_2COOH$
24	Nervonic acid	15-Tetracosenoic acid	24:1	$CH_3(CH_2)_7CH=CH(CH_2)_{13}COOH$

Saturated and unsaturated fatty acids commonly found in glycerophospholipids.
Adapted from Biochemistry, by Garrett and Grisham [1].

PLC products

Phosphatidyl
Inositol   =>

Inositol
phosphate

+

Diacylglycerol

PLD products

Phosphatidyl-
glycerol   =>

Glycerol

+

Phosphatidic
acid

PLD

PLC

PLA$_1$

PLA$_2$

PLA$_1$ products

Phosphatidic
acid   =>

Free Fatty Acid   +

Lysophospholipid

PLA$_2$ products
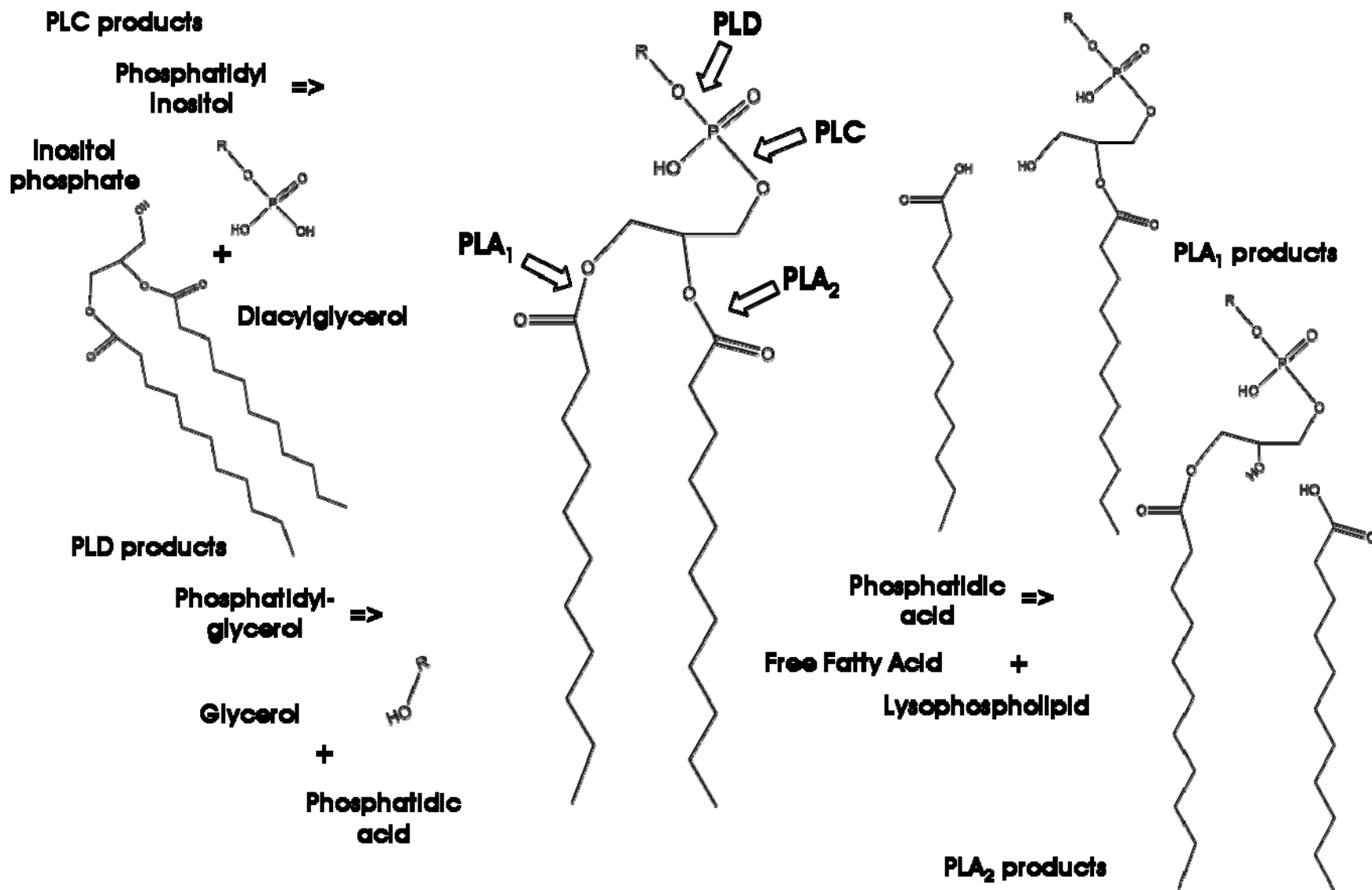
Figure 2 Phospholipase Cleavage Sites
Representative hydrolysis products and cleavage sites for Phospholipases A1, A2, C and D

3

Phospholipases are classified as interfacial enzymes, because the interaction between the water soluble enzyme and its water insoluble substrate must occur at the interface between the aqueous solvent and aggregated phospholipids. Phospholipase A2 (PLA$_2$), analogous to trypsin or lysozyme in solution enzymology, is considered the prototype for the characterization of interfacial enzymes [2]. For PLA$_2$, the substrate aggregates are found in the form of small mixed micelles, such as dietary lipids and bile salts [3], intermediate heterogenous aggregates such as LDL or HDL [4; 5; 6], or the large continuous surfaces of biological membranes such as intracellular nuclear membranes [7; 8]; extracellular plasma membranes [9; 10]; localized intestinal lumina [11; 12]; or mobile erythrocytes [13; 14] and bacteria [15; 16; 17]. The global regulation of this enzyme is related to its general function: snake venom PLA$_2$ is injected from salivary glands into prey; honey bee venom PLA$_2$ is injected from the venom gland as a defense mechanism; pancreatic PLA$_2$ is secreted as a zymogen into the digestive tract [18; 19] to assist in the metabolism of dietary lipids; and synovial PLA$_2$ (originally isolated from the synovial fluid of patients with rheumatoid arthritis), is secreted in tears to protect the eye from bacterial infection [20; 21]. The local or molecular mechanism regulating the interaction of PLA$_2$ with its substrate is related to its molecular function: cytosolic PLA$_2$ (cPLA$_2$) is constitutively expressed and regulated by phosphorylation [22; 23; 24]; secreted PLA$_2$s (sPLA$_2$) are regulated by localized expression [25] or shuttling to internal vesicles by heparin sulfate mediated endocytosis [26]; as first responders for the innate immune system, sPLA$_2$s are sequestered in granulocytes [27; 28]; or localized to potential avenues of entry such as the mucous membranes of the respiratory [29; 30; 31] and gastrointestinal tracts [32], or in skin keratinocytes [33].

As seen in Figure 2, the hydrolysis products for PLA$_2$ are a lysophospholipid and a free fatty acid. The most significant products of PLA$_2$ hydrolysis, as it pertains to human health and

disease, are arachidonic acid [34; 35] and a lysophospholipid that can be further metabolized into platelet activating factor [1]. Arachidonic acid is the precursor to eicosanoids such as prostaglandins, leukotrienes, and thromboxanes. As their name implies, these products were first identified in prostate glands, leukocytes, and thrombocytes. The eicosanoids mediate many diverse physiologic functions such as reproduction [36], blood pressure [37], smooth muscle contractions [38; 39], blood clot formation [40], and the classic symptoms of inflammation: rubor, tumor, calor, dolor (redness, swelling, heat and pain) [41; 42]. PLA_2 has been implicated in many disease states which correlate to aberrations of its native function: asthma [29; 43], arthritis [44], Crohn's disease [45; 46], premature labor [47], cancer progression [48; 49], and neurodegenerative diseases[50].

Because of the pivotal role of PLA_2s in inflammation, allergy and tumorigenesis, these enzymes have been the focus of extensive research. Much is understood about the general properties of these enzymes however, each new result adds to the expanding complexity of the PLA_2 paradigm. From an initial classification of two types of PLA_2s, venom and pancreatic, has grown a superfamily of interrelated enzymes. Hydrolysis of the *sn*-2 ester bond of glycerol phospholipids is the only characteristic shared by every member of the PLA_2 superfamily, which have been classified into groups according to common features such as amino acid sequence, disulfide bonding pattern, size, cellular location or catalytic requirements for calcium. The groups presently established, and some of the general characteristics, including the common sources of the enzyme, are presented in Table 2.

Table 2 Phospholipase A2 Superfamily

	GROUP: designation	SIZE KD	Ca²⁺ req	Disulfide bridges	Archetype/other common sources
Secreted	IA: sPLA$_2$	~14	mM	7	Cobra
	IB: sPLA$_2$	~14	mM	7	Pancreas
	IIA: sPLA$_2$	~14	mM	7	Human: synovia and platelets, tears/ Rattlesnakes, vipers; mammals
	III: sPLA$_2$	~14 (h:55)	mM	5	Honey Bee/ Lizard/ Scorpion
	V: sPLA$_2$	~14	mM	6	Human/ mammal heart, lung, macrophage/ Primary PLA$_2$ in mouse
	IX: sPLA$_2$	~14	<mM	6	Marine snail
	X: sPLA$_2$	~14	mM	8	Human spleen, thymus, leukocyte
	XII sPLA$_2$	~18	mM	7?	Zebrafish/ human heart, kidney, skeletal muscle
Cytosolic	IV: A cPLA$_2$ α	85	<μM		Human platelets/ rat kidney
	IV: B cPLA$_2$ β	114	<μM		Human pancreas, liver, heart, brain
	IV: C cPLA$_2$ γ	61	none		Human heart, skeletal muscle
	VI A1: iPLA$_2$ A	84-85	none		Human pancreatic islets
	VI A2: iPLA$_2$ B	88-90	none		Human pancreatic islets
	VI B: iPLA$_2$ γ	88	none		Human pancreatic islets
	VII: PAF-AH	45	none		Human plasma
	VII: PAF-AH (II)	40	none		Human plasma
	VIII: PAF-AHIb α$_1$	26	none		Bovine brain
	VIII: PAF-AHIb α$_2$	26	none		Bovine brain
XI		~13	N/A		Green rice sheets

Phospholipase A2 superfamily sorted by cellular location. Designation: secreted: sPLA$_2$, cytosolic: cPLA$_2$, calcium independent: iPLA$_2$, and Platelet-activating factor acetylhydrolase: PAF. Compiled from reviews by Dennis, Murakami and Singer [51; 52; 53]

Because of their significance to health and disease, we have directed the focus of this work on two human PLA_2 paralogs, the pancreatic group IB (hIB PLA_2), and the synovial group IIA (hIIA PLA_2). These two enzymes share a highly conserved primary sequence [54] with the other members of groups I, II, V and X, which will be referred to in this work as $shPLA_2$ (homologous $sPLA_2$). The high sequence homology between these isoforms results in nearly superimposable three dimensional structures, consisting of three alpha helices and a small antiparallel beta sheet. Figure 3, a schematic representation of hIIA PLA_2, illustrates the general relationship between the secondary structure and primary sequence. This same relationship can be applied to any other $shPLA_2$ through a core numbering system (Table 3), which is based on bovine IB PLA_2 in order to facilitate comparisons between isoforms [54]. The first 10 – 12 amino acids make up the amphipathic N-terminal alpha helix (H1), followed by a loop containing several residues that contribute to substrate binding and calcium coordination. The second alpha helix (H2), residues 40-58, contains the catalytic residue His^{48}. H2 is followed by a short loop of surface interacting residues, as well as Lys^{69} (Tyr^{69} in hIB PLA_2), a key participant in substrate stabilization. The loop is followed by a beta sheet, spanning residues 74-85. One of the cysteines unique to group IB PLA_2 (Cys^{77}) connects the beta sheet through a disulfide bridge to the other group specific cysteine in the N-terminal helix (Cys^{11}), functionally connecting the two structures. The apparent allosteric relationship between membrane binding and enzyme activation, mediated by the group IB PLA_2 N-terminal helix [55; 56], could be the effect of this group specific structure. The third alpha helix (H3), residues 91-109, contains the catalytic residue Asp^{99}, as well as four cysteines that anchor H3 to H2 and the calcium binding loop. The C-terminal loop contains a short extension unique to group IIA PLA_2, linked by a disulfide bridge to H2 through a group II specific cysteine at its terminus.
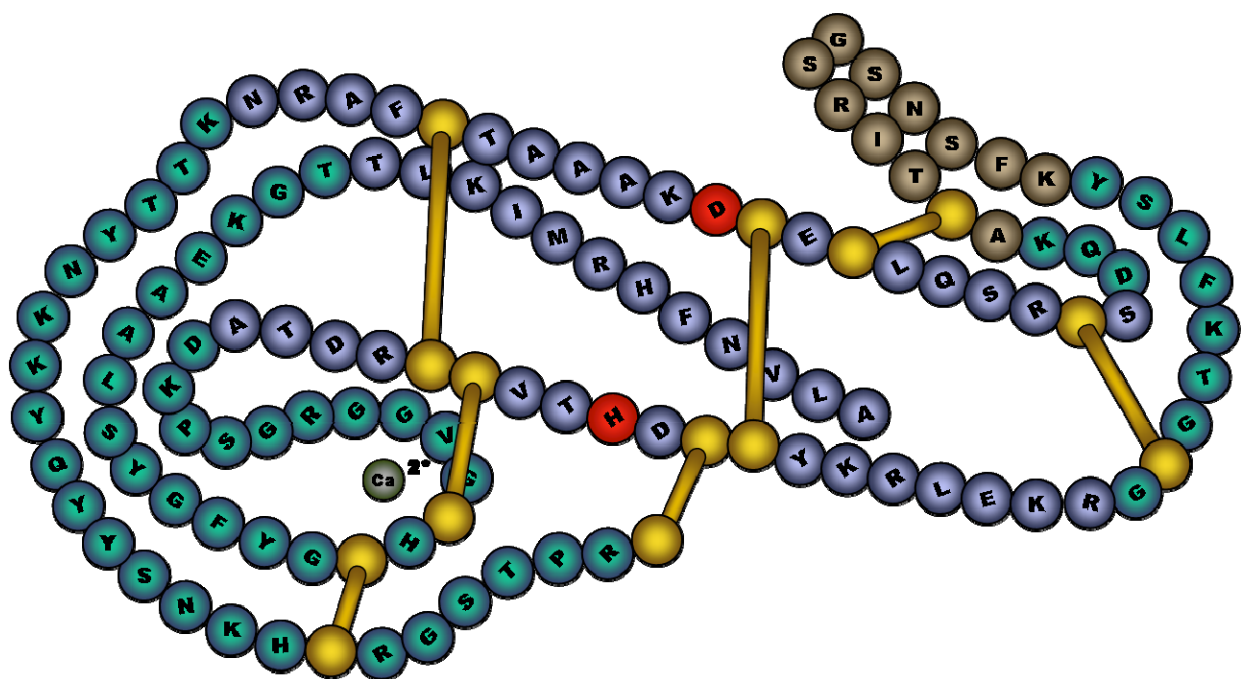
Figure 3 hIIA PLA$_2$
The alpha helical residues are blue, beta sheet residues are brown, loops are green and disulfides gold.
The active site residues are shown in red. Refer to body of text for further details.

The tertiary structure, as revealed by both X-ray and NMR methods, is relatively oblong with a nearly planar surface which interacts with the aggregated substrate, called the interfacial binding surface (IBS) [57]. The substrate enters the enzyme through an opening located on the IBS into the substrate binding channel. The entrance is surrounded by a 'collar' of hydrophobic residues facilitating entry by the hydrophobic substrate. The catalytic site, located along one wall of the substrate binding channel, includes a calcium ion cofactor which also coordinates the substrate *sn*-3 phosphate group. The other wall of the channel is made up of residues lining the internal face of the N-terminal helix. Several hydrophobic residues from H2 and H3 make up the length of the channel, which terminates at a small opening on the dorsal surface of the enzyme.

Table 3 Sequence alignment

Bovine IB serves as the core sequence numbering system, human IB and IIA PLA$_2$ numbering are also presented

Two similar mechanisms have been proposed for the specific catalysis by shPLA$_2$s. The first is analogous to the triad mechanism of serine protease [58], and the second is a proposed calcium-coordinated oxyanion mechanism [59]. The catalytic triad mechanism for shPLA$_2$ (Figure 4), consists of His[48], Asp[99] and a conserved water molecule (*w*6). In this scenario, the *sn-2* carbonyl of the phospholipid substrate is coordinated by the active site calcium, inducing a dipole across the carbonyl making it energetically favorable for a nucleophilic attack. The Asp[99] is hydrogen bonded to the εNH of His[48], which acts as a general base to deprotonate the conserved water, generating the attacking OH⁻ nucleophile. The attacking hydroxide nucleophile facilitates the formation of a tetrahedral intermediate, which quickly decomposes as the proton is transferred from the His[48] δN to the *sn-2* O⁻ of the lysophospholipid leaving group. The rate limiting step is presumed to be the formation of a tetrahedral intermediate while the δN of H[48] is protonated.

The oxyanion mechanism (Figure 5) is similar to the catalytic triad mechanism, with the exception of a second conserved water (*w*5) which is coordinated to the active site calcium. This water becomes the attacking nucleophile through *w*6, which is hydrogen bonded to His[48]. The delocalization of electrons across the hydrogen bond network: Asp[99]-His[48]-*w*6-*w*5-Ca^{2+}, facilitates the transfer of the proton from *w*5 to *w*6, and then from *w*6 to the leaving group. In this mechanism, the decomposition of the tetrahedral intermediate is the rate limiting step. A molecular dynamics simulation of this process [59] using only *w*6, demonstrated the movement of the water from the *w*6 to the *w*5 positions, before a proximal water moved into the *w*5 position.
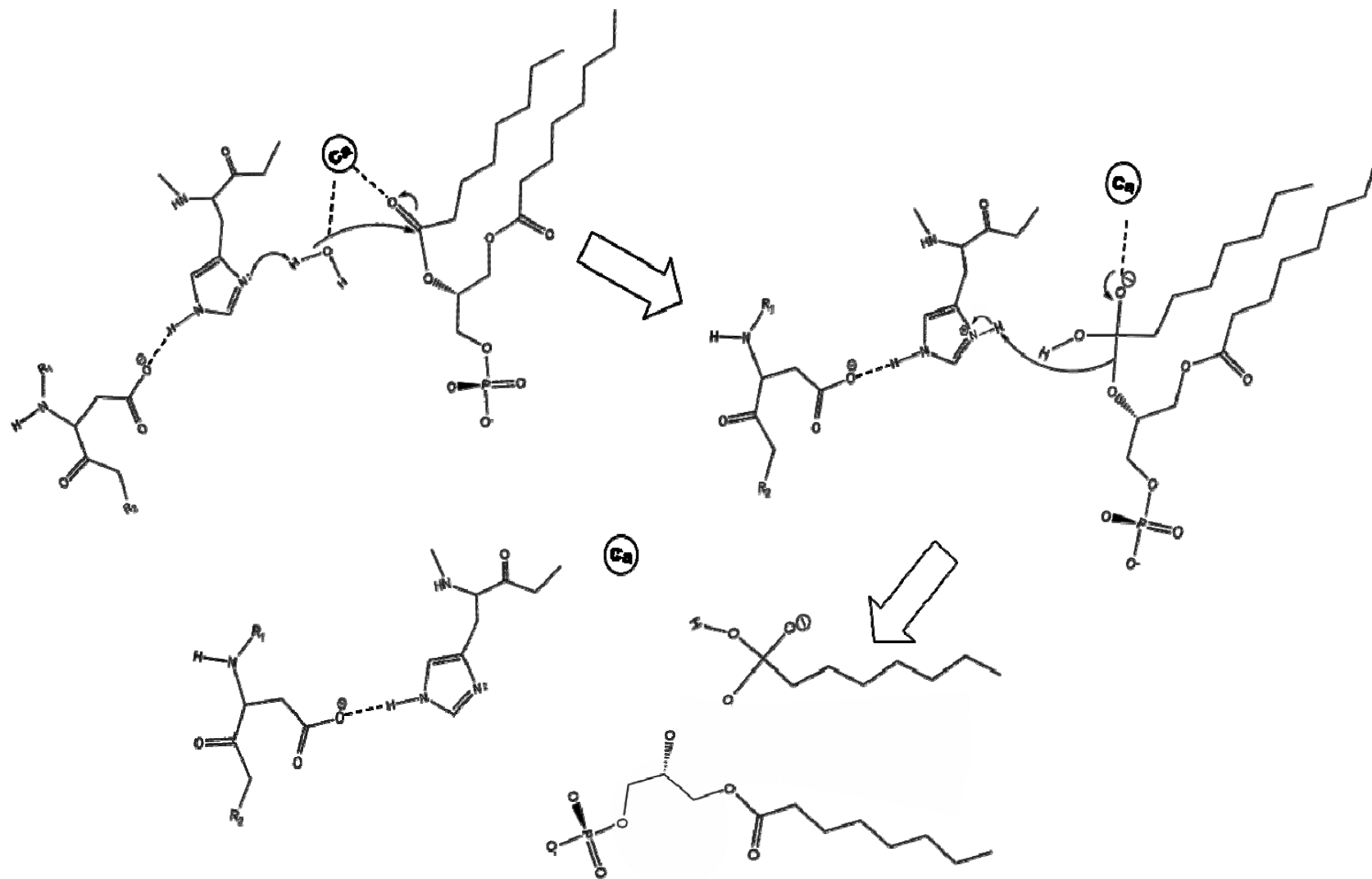
Figure 4 Catalytic mechanism I
Catalytic Triad mechanism with a conserved water as nucleophile.
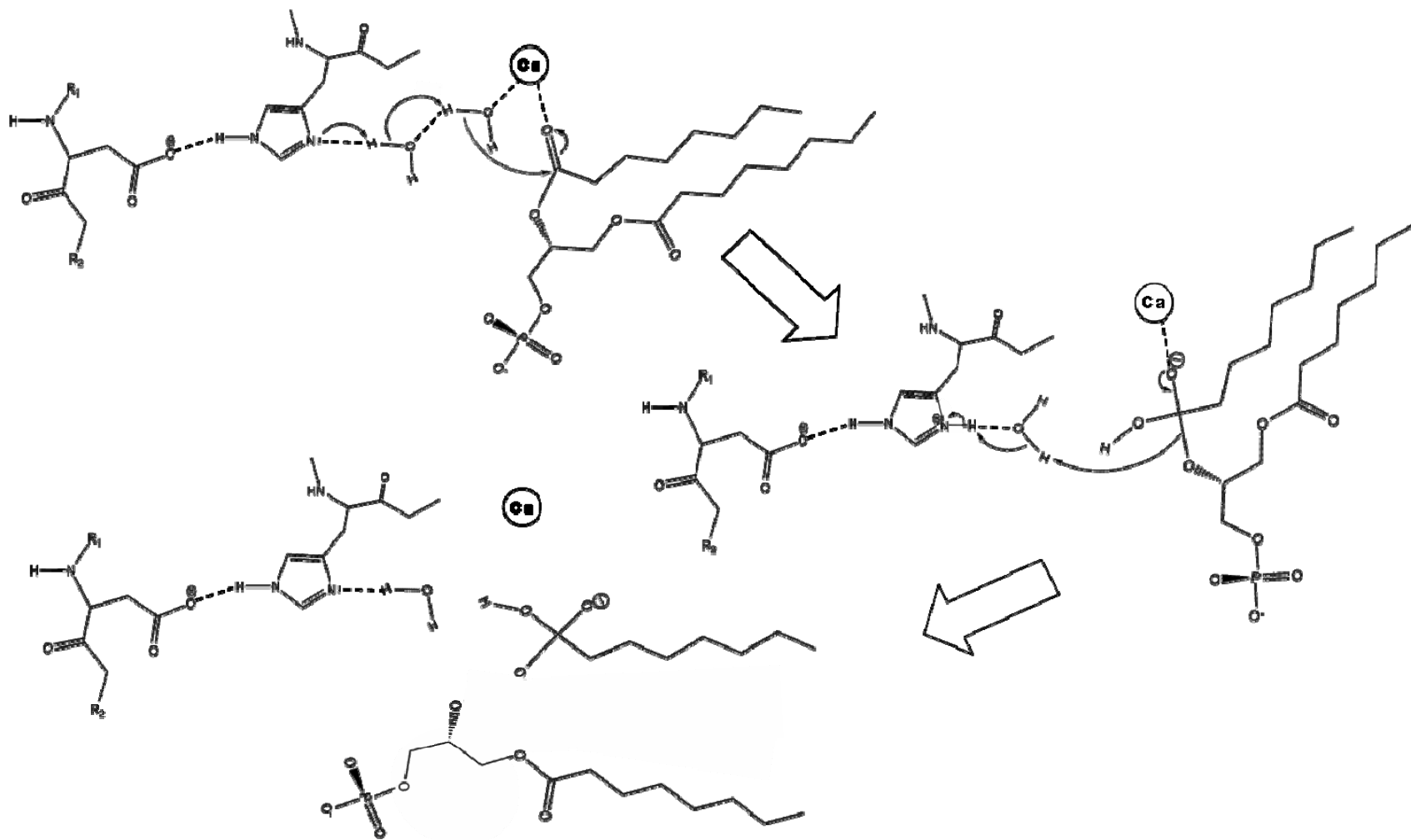
Figure 5 Catalytic mechanism II
Oxyanion mechanism with two conserved water molecules, the second water acts as nucleophile.

The catalytic activity of these enzymes is directly related to its substrate specificity. As interfacial enzymes, the binding of a single substrate to the catalytic site is dependent upon effective binding of the enzyme to the aggregate containing the single substrate such as micelles or membranes. Therefore the overall rate of hydrolysis is a reflection of not only the catalytic activity of the enzyme, but of the preliminary binding step as well. The Michaelis-Menten kinetic paradigm is used to evaluate water soluble enzymes and their water soluble substrates. An expanded kinetic scheme has been proposed for interfacial enzymes, incorporating the prerequisite binding step [60] (Figure 6).
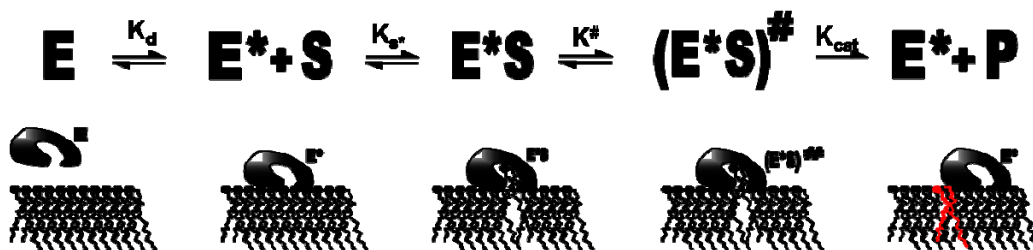
Figure 6 Kinetic scheme
Schematic diagram of the interaction between an interfacial enzyme and its aggregated substrate. E* denotes the membrane bound enzyme, S the single phospholipid substrate and P the products, shown in red. K_d is the dissociation constant, K_{s*} the constant for the association of the monomeric substrate with the enzyme, $K^{\#}$ the constant for interfacial activation, and K_{cat}, the constant for the rate of catalysis.

Through the kinetic dissection of the shPLA$_2$ isoforms, the maximum reaction velocity, binding affinities for substrate and inhibitors, and responses to reaction conditions have been identified [2]. Various substrate specific modulators of enzymatic function, such as liquid ordered or gel phases of the aggregate [61], surface topography [62; 63], or headgroup charge [15; 64], have been identified. What has yet to be defined is the specific mechanism(s) by which the physical nature of the substrate induces an observable change in the catalytic rate of the enzyme: starting with a low to moderate rate, followed by a sudden burst of activity at the maximum rate, coined interfacial activation.

For group I and II PLA$_2$s, this apparently induced activation is pronounced on zwitterionic aggregates, for which these sPLA$_2$s have a low binding affinity. The accelerated activity is shown to be mediated by the buildup of anionic products within the aggregate [65], leading to a tighter binding of the enzyme through interactions with cationic residues on the IBS. However, the tightness of the interaction does not necessarily induce an increase in activity, as site specific mutations have resulted in enzymes that bind tighter than the wild type, but have a lower specific activity [66; 67]. Atomic resolution structures, revealing either no or small structural changes in enzymes with or without bound substrate analogs or inhibitors [66; 68; 69], resulted in conflicting conclusions as to structural changes mediating interfacial activation. Many substrate associated and enzyme associated contributors have been identified, but as yet no unifying mechanism has been proposed. By focusing on two well characterized human sPLA$_2$ isoforms, pancreatic group IB and synovial group IIA, this work endeavors to elucidate the subtle structural determinants of function at the enzyme-substrate interface, in order to provide insight into the understanding of interfacial activation at a molecular level.

Between the homologous groups of sPLA$_2$s (I, II, V and X), there are several characteristic differences in primary structure, as well as several invariant residues which are specific for a particular group or species. These relatively small structural differences contribute to unique functional specificities. For example, group IB enzymes demonstrate a low to moderate activity toward zwitterionic substrates [55; 70], but human group IIA, a highly cationic enzyme, does not bind to zwitterionic substrates, but only demonstrates appreciable membrane binding and activity when the membranes contain at least 15 mol% of anionic lipids [71]. This affinity for anionic lipids enables hIIA PLA$_2$ to act as an effective antimicrobial in human tears[16], hydrolyzing bacterial membranes which have a high content of phosphatidylglycerol, an anionic

lipid. The differences in function and specificity of the shPLA$_2$s are mediated by isoform-specific amino acid residues found in the non-homologous regions of the enzymes. It is these types of subtle differences that make the shPLA$_2$ enzymes an excellent model for studying structure-function relationships.

The N-terminal 10-12 residues of group I and II PLA$_2$s constitute a functionally important amphipathic alpha helix. The N-terminal helix contributes to membrane binding through several cationic and nonpolar residues along one face of the helix, and to substrate entrance into the active site cleft by several hydrophobic residues along the opposite face of the helix (Figure 7). The conserved hydrophobic residue at position 3 enhances binding to zwitterionic lipids such as phosphatidylcholine (PC), a major constituent of the outer leaflet of plasma membranes. A tryptophan in this position is unique to the group IB PLA$_2$ isoform: all other shPLA$_2$s have a valine or other hydrophobic residue in the third position. Mutation of the Trp^3 of bovine group IB PLA$_2$ to Ala caused a 3 to 7 fold decrease in activity of the enzyme toward dimyristoyl-phosphatidylmethanol (DMPM) membranes or diheptadecyl PC micelles [72]. Conversely, the introduction of a Trp into the 3rd position of hIIA PLA$_2$, which lacks the ability to bind to neutral membranes, resulted in a mutant with a relatively high affinity to bind to and hydrolyze PC membranes [73; 74; 75]. Interestingly, Trp mutations of the other seven nonpolar residues that constitute the hydrophobic collar of hIIA PLA$_2$, had little or no increased activity [74]. The enhanced activity of the Trp^3 mutant towards zwitterionic substrate was interpreted in terms of Trp mediated stronger binding of the enzyme to the membrane [73; 74]. The collective data however are inconsistent, with a wide range of binding affinities and rates of activity, including variations in affinity toward anionic substrates in various forms such as micelles or LUVs.
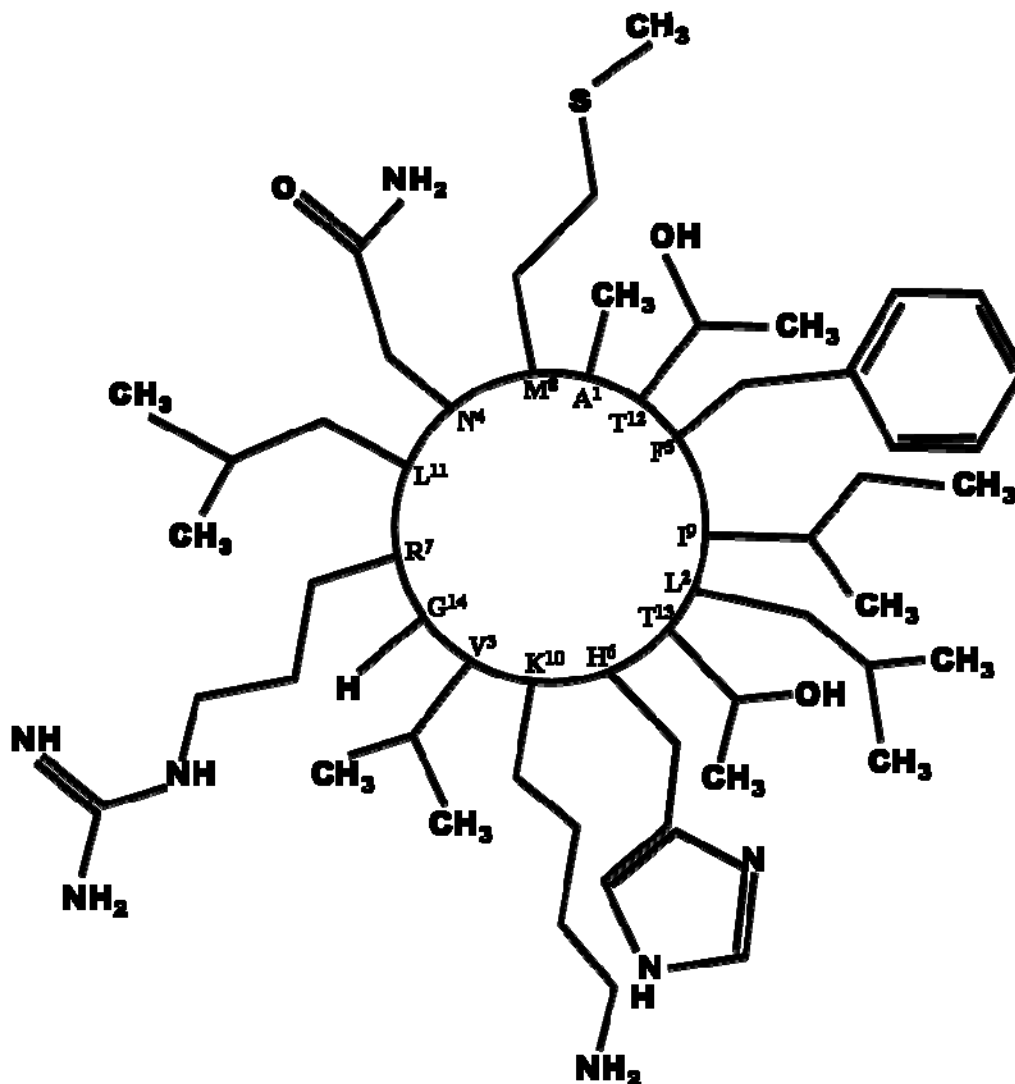
Figure 7 hIIA PLA$_2$ N-terminal helix
Shiffer-Edmundson wheel projection of the N-terminal helix of hIIA PLA$_2$.The first residue (Ala[1]) is near the top of the wheel, the membrane interacting residues from Lys[7] to Leu[2], are at the bottom.

The specific catalytic activity of the enzyme is dependent upon the substrate binding to the enzyme's active site. Two residues, Phe[5] and Ile[9] are invariant in all but group V shPLA$_2$s. A single study of bovine IB PLA$_2$, substituting Phe[5] by hydrophobic or aromatic residues of either smaller or larger size, reported reduced activity for all mutants [76]. Atomic-resolution structures of group I and II PLA$_2$s with bound substrate-mimic inhibitors, show intimate van der Waals contacts between the side chain of Phe[5] and the hydrophobic moieties of the bound inhibitor [77;

[78; 79; 80], suggesting that Phe^5 may serve to facilitate a productive enzyme-substrate interaction. These mutational studies clearly underscore the functional importance of Trp^3 and Phe^5.

The focus of this work has been to define structure-function relationships involved in interfacial activation of human group IB and IIA PLA$_2$s upon binding to aggregated substrate, using an interdisciplinary approach combining molecular, biochemical, biophysical and computational methods. In order to determine the precise membrane binding modes of group I and II PLA$_2$s, we have created a semisynthetic, segmentally isotope labeled hIB PLA$_2$, as well as a chimeric PLA$_2$ (hIIA/IB PLA$_2$) containing the first 10 N-terminal residues of hIIA PLA$_2$ ligated to a fragment of hIB PLA$_2$ (hIBΔN10 PLA$_2$) lacking the first 10 residues [81; 82]. Two single residue mutants of hIIA PLA$_2$ substituting Trp^3 and Phe^5 with tryptophan (V3W, F5W), have been produced in order to elucidate the mechanism by which a minor structural change: a single amino acid substitution, can cause dramatic functional changes in the catalytic activity of these relatively small, stable enzymes. We have employed lipid aggregates in a variety of forms: micellar, vesicular, and supported bilayers, varying the compositional concentrations of negative lipids, in order to search out the subtleties of behavior of native and mutant group I and II PLA$_2$ molecules. The functional roles of the native Trp^3 were evaluated through parallel experiments with hIB PLA$_2$. We have determined structural consequences for the substitution of a phenylalanine for a bulkier tryptophan in the substrate binding pocket of human group IIA PLA$_2$.

Our results present considerable methodological advances for the determination of the precise membrane binding mode of peripheral membrane proteins; uncover isoform-specific membrane binding modes, as well as conformational and stability changes in shPLA$_2$s during membrane binding; and identify dramatically different activity and conformational changes in hIIA PLA$_2$ induced by Trp mutations of closely located residues. The latter are interpreted in

terms of distinct effects of Trp at the membrane-binding *versus* substrate-binding sites of hIIA PLA$_2$ on conformational changes accompanying the interfacial activation of the enzyme. The results of this work identify the N-terminal helix of group I and II PLA$_2$s as a regulatory site of the enzyme, and implement the idea that not only the membrane binding strength, but depth of membrane insertion and especially the orientation of the enzyme to the membrane, are critical determinants for the function of shPLA$_2$s.

CHAPTER TWO: MATERIALS AND METHODS

Materials Miniprep and PCR recovery kit were obtained from Qiagen (Valencia, CA); primers designed to incorporate point mutation were from Molecula (Herndon, VA); pGEM-T vectors and DH-5α bacteria were from Novagen (Madison, WI); and restriction enzymes were from Amersham (Piscataway, NJ). The sPLA$_2$ activity kit was from Cayman Chemical (Ann Arbor, MI) and the Silver Stain kit from Invitrogen (Carlsbad, CA).

The lipids, 1-palmitoy-2-oleoyl-*sn*-glycero-3-phosphocholine (POPC); 1-palmitoy-2-oleoyl-*sn*-glycero-3-phosphoglycerol (POPG); and 1-palmitoy-2-stearoyl-(6,7) dibromo-*sn*-glycero-3-phosphocholine (Br$_2$PC), brominated at positions 6-7, 9-10, or 11-12; were from Avanti Polar Lipids (Alabaster, AL). 1,2,bis-(1-pyrenedecanoyl)-*sn*-glycero-3-phosphocholine (BisPy-PC), and N-(fluorescein-5-thiocarbamoyl)-1,2-dihexadecanoyl-*sn*-glycero-3-phospho-ethanolamine (FPE) were from Molecular Probes (Eugene, OR). The bacterial vector with the human group IIA PLA$_2$ gene, mutated at the first position from Asparagine to Alanine to facilitate removal of the initiator methionine in *E. coli* (N1A hIIA PLA$_2$), was kindly provided by Prof. David Wilton (University of Southampton, UK). All proteins have been lyophilized out of pure water and resuspended in the appropriate buffers for each experiment. Experimental buffer composition was 50 mM HEPES (pH 7.4 at 25 °C), 100 mM NaCl, 1 mM NaN$_3$, 1 mM EGTA, unless otherwise stated. Due to the highly cationic nature of the hIIA PLA$_2$ isoform, all glassware, plastic tips and tubes were first coated with Sigmakote (Sigma, St Louis, MO), to reduce loss of protein by adsorbtion to any contact surfaces. The hIB PLA$_2$ N-terminal peptide: N10-hIB (Ac-Ala-Val-Trp-Gln-Phe-Arg-Lys-Met-Ile-Lys-NH$_2$), and the hIIA PLA$_2$ N-terminal peptide: N10-hIIA (Ac-Asn-Leu-Val-Asn-Phe-His-Arg-Met-Ile-Lys-NH$_2$) were synthesized by

Advanced ChemTech (Louisville, KY) and were ~99% pure as confirmed by HPLC and mass-spectrometry. All other chemicals were obtained from Sigma (St. Louis, Mo).

Production of Recombinant Proteins The plasmid containing the N1A hIIA PLA$_2$ gene was extracted and purified from the original *E. coli* clone and sequenced, using a Beckman-Coulter CEQ 2000 XL DNA sequencer (Fullerton, CA). The sequence was analyzed to determine the flanking restriction sites and primers designed to incorporate point mutations into the N1A hIIA PLA$_2$ gene. PCR was employed to generate the mutated target gene, using the original plasmid as template, and the following forward primers: V3W: 5'-TACAT ATG GCC CTG TGG AAC TTC CAC CGT ATG-3', F5W: 5'-TACAT ATG GCC CTG GTA AAC TGG CAC CGT ATG-3'. The same reverse primer was used for both reactions: 5'-TCA TCG ATA AGC TTC ACT ATT AGC-3'. The PCR product was inserted into pGEM-T easy vector, sequenced and amplified in *E. coli* DH-5α. The target was subcloned into the expression vector pET-21a (+) (NdeI/HindIII restriction sites) and used to transform BL21 (DE3) expression line. As the first amino acid substitution does not modify the structure or other properties of hIIA PLA$_2$, the N1A clone is designated hIIA PLA$_2,$ and the 3rd and 5th position tryptophan mutants by the single mutation reference V3W and F5W respectively. Production of human group IB PLA$_2$ and its fragment minus the first 10 residues (hIBΔN10) by recombinant DNA manipulation techniques is described in Qin et al., 2004 [83]. Ligation of the N10-hIB peptide and the N10-hIIA peptide to the hIBΔN10 fragment, which had been uniformly labeled with ^{13}C, to generate segmentally labeled full length hIB PLA$_2$ and a chimeric hIIA/IB PLA$_2$ protein is described in Tatulian et al., 2005 and Qin et al., 2005 [81; 82].

Expression and purification of hIIA PLA$_2$ The human IIA PLA$_2$ protein was expressed in a minimal medium enriched with ^{15}N-labeled ammonium chloride (^{15}NH$_4$Cl) and ^{13}C$_6$-D-glucose as sole metabolic nitrogen and carbon sources, for NMR experiments. The minimal medium consisted of 6.8 g/L Na$_2$HPO$_4$, 3.0 g/L KH$_2$PO$_4$, 0.5 g/L NaCl, 1.0 g/L ^{15}NH$_4$Cl, which was first autoclaved before supplementing with a sterile solution of ^{13}C$_6$-D- MgSO$_4$*7H$_2$O, CaCl$_2$*2H$_2$O, Thiamine, FeSO$_4$*7H$_2$O, and carbenicillin at final concentrations of 2.0, 0.494, 0.0147, 0.01, 0.01, 0.2 mg/mL, respectively. hIIA PLA$_2$, V3W and F5W for biophysical experiments were expressed in standard LB media, with 0.2 mg/mL carbenicillin. The expression protocol, adapted from Othman et al.,1996[84], was modified in order to optimize the yield of hIIA PLA$_2$. The condensed protocol is as follows: Each expression was initiated by the selection of several large single colonies from 1% ampicillin plates. The plates were cultured from glycerol stocks stored at -80 °C and incubated overnight at 37 °C. Forty mL for each liter of culture media was inoculated and incubated overnight at 37 °C on an orbital shaker set to 250 rpm. The overnight culture was transferred into the expression media. After recording the initial OD$_{600}$, the culture was incubated at 37 °C, 250 rpm. Expression was induced with IPTG, 1mM final concentration, when the corrected OD$_{600}$ was $\approx$ 0.6 (corrected OD$_{600}$ = OD$_{600}$ - OD$_{600}$ initial). Cells were cultured at 37 °C for 6 hrs after induction, before reducing the temperature to 27 °C and incubated overnight. The cells were harvested by centrifugation at 6,000 rpm for 10 minutes, and supernatant discarded. Purification of inclusion bodies out of the bacterial cells consisted of lysing the cells and washing the pellet four times. The first two washes were facilitated by sonication (on ice, 2 minutes on, 2 minutes off; three times) using a Sonic Dismembrator (Fisher Scientific, Suwanee, GA), and the third with stirring at ambient temperature for 20 minutes. The inclusion bodies were pelleted after each wash by centrifugation (12,000 rpm, 4 °C, 30 min) and

21

the supernatant discarded. The washes consisted of 50 mM Tris-HCl (pH 8.0 at 4 °C), 50 mM NaCl, 1 mM EDTA, 1 mM NaN_3, supplemented with: 1) 0.4% Na-deoxicholate, 0.4% Triton X-100, 0.2 mg/mL lysozyme, 1x stock protease inhibitor; 2) 0.8% Na-deoxicholate, 0.8% Triton X-100 and 1x stock protease inhibitor; 3) 1% Triton X-100; and 4) Tris-HCl buffer alone. The purified inclusion bodies were subsequently denatured in a solution of 6 M Guanidine HCl and 5% β-mercaptoethanol in the Tris-HCl purification buffer, with stirring, at 4 °C overnight. The refolding of the protein was mediated by gradual dialysis against 0.9 M Guanidine HCl in a 25 mM Tris-HCl buffer (pH 8.0 at 4 °C), supplemented with 5 mM $CaCl_2$, 5 mM L-Cysteine (4x 2L, ~8 hrs each, with stirring at 4 °C). After refolding, the refolding buffer was exchanged by dialyzing against a low salt binding buffer: 20 mM Tris-HCl (pH 7.4 at 4 °C), 2.5 mM KCl. The final purification consisted of a two step column chromatography scheme utilizing an ÄKTA purifier 100 and chromatography columns from Amersham Biosciences (Piscataway, NJ). After centrifugation (12,000 rpm, 30 min, 4 °C), then the solution passed through a 2 μm syringe filter. The solution was loaded onto a 20 mL heparin column and washed with three column volumes of the binding buffer. The protein was eluted with a linear concentration gradient of a high salt elution buffer: 20 mM Tris-HCl (pH 7.4 at 4 °C), 1.5 M KCl. The active fractions were identified using the $sPLA_2$ activity kit from Cayman Chemical and pooled. The sample volume was reduced to 2 mL, using Amicon YM-3000 concentrators (Millipore) and loaded directly onto a HiLoad 16/60 Superdex 75 column, without exchanging the high salt buffer for the size exclusion buffer. The protein was eluted from the superdex column at 0.5 mL/min with a size exclusion buffer: 20 mM Tris-HCl (pH 7.4 at 4 °C), 25 mM KCl, and fractions checked for PLA_2 activity. Purity was determined using SDS-PAGE (15% polyacrylamide) and visualized by silver staining. Only pure, active fractions were collected, pooled and dialyzed against pure water,

Milli-Q filtered (ddH$_2$O). The final protein concentration was checked using the OD$_{280}$ and the protein was lyophilized and stored at -80 °C.

Determination of extinction coefficients One mg of pure protein was weighed and dissolved in 1 mL ddH$_2$O. The OD$_{280}$ was measured using a 0.4 cm path length, quartz cuvette on a Carey 100 double-beam spectrophotometer (Varian Inc., Palo Alto, CA). The adjusted molecular weight of each protein was calculated from the respective sequences. The extinction coefficients were derived from the equation A = εcl for the hIB PLA$_2$, hIIA PLA$_2$, V3W and F5W proteins.

PLA$_2$ activity against phospholipid micelles Specific activity of each protein was measured using an assay kit specific for sPLA$_2$ from Cayman chemical (Ann Arbor, MI), on a Cary 100 double-beam spectrophotometer (Varian Inc., Palo Alto, CA). The kit consists of diheptanoyl-thio-phosphatidylcholine (DHTPC) substrate, 5,5'-dithio-bis-(2-nitrobenzoic acid) (DTNB) reporter and buffer concentrate. As PLA$_2$ hydrolyzes the thio-lipid substrate, the free thiol at the *sn*-2 position of the lysolipid reacts with the DTNB, liberating the chromophore, 5-thio-2-nitrobenzoic acid that strongly absorbs around 414 nm. Therefore, the signal at 414 nm can be used to quantitatively measure the amount of hydrolyzed lipid, using the extinction coefficient of 5-thio-2-nitrobenzoic acid ε_{414} = 13,600 M^{-1} cm^{-1}. The final composition of the buffer was 25 mM Tris-HCl (pH 7.5), 100 mM KCl, 10 mM CaCl$_2$, 0.3 mM Triton X-100, 0.5 mM DTNB, and 1 mg/mL bovine serum albumin (BSA). The reaction was initiated by the addition of PLA$_2$ to a final concentration of 0.35 µg/mL to the sample cuvette.

Preparation of large unilamellar vesicles A Liposofast extruder (Avestin, Ottawa, Canada) with two stacked 100 nm polycarbonate filters, was used to generate large unilamellar vesicles (LUV) of uniform size. 10 mM stock solutions of lipid in chloroform were aliquoted and

mixed in desired molar ratios. The solvent was removed under a light stream of compressed nitrogen, followed by dessication under vacuum for a minimum of 3 hours. The lipid film was suspended in aqueous buffers and vortexed for 3 minutes. The resulting dispersions were injected through the extruder until clear (19 passes), and the resultant LUVs were used within 4 hours of preparation.

Fluorescence and circular dichroism experiments Fluorescence and circular dichroism (CD) measurements were conducted using a Jasco 810 spectrofluoropolarimeter (Jasco Corp., Tokyo, Japan). This particular model is equipped with an additional photomultiplier tube mounted at 90 degrees for fluorescence measurements and a Peltier water cooled thermostat and stir plate. CD spectra of protein and appropriate controls were obtained using a 0.2 mm optical path-length quartz cuvette. Ellipticity, θ, was measured between 260 and 180 nm, with a band width of 1, scan speed of 100 nm/min and 1 second response time. 10 scans were collected and averaged to enhance the signal to noise ratio. After subtracting the controls, spectra were corrected for protein size (number of residues) and concentration to obtain the mean residue molar ellipticity: $[\theta]$ (see Appendix A, CD). Experimental protein concentration was 5 mg/mL in a 10 mM phosphate buffer (pH 7.4 at 25 °C).

Fluorescence quenching experiments Membrane insertion of Trp residues was determined by fluorescence quenching spectroscopy, using the J-810 spectrofluoropolarimeter described above. The samples were contained in a 4×4 mm^2 rectangular quartz cuvette, with constant stirring. Excitation and emission slits were 4 and 10 nm, respectively. Tryptophans were selectively excited at 290 nm, and the emission spectra were recorded between 300 and 400 nm, followed by spectral correction by subtracting the spectra measured under identical conditions but without the protein or peptide. In experiments of Trp fluorescence quenching with

24

acrylamide, PLA_2 or peptide solutions were prepared in buffers that contained 1 mM EDTA, 50 mM HEPES (pH 7.4) and varying concentrations of acrylamide. Emission spectra were measured, maximum fluorescence intensities without and with the quencher (F_0 and F respectively) were determined. In dual quenching experiments, Trp emission intensity was measured in the presence of lipid vesicles with no quencher (F_0), in the presence of vesicles and with 250 mM acrylamide in the buffer (F_{acrly}), and in the presence of vesicles containing 10 mol% of 10-doxylnonadecane (10DN) with no acrylamide in the buffer (F_{10DN}).

Activity assay against bilayer membranes The activity of PLA_2 toward LUVs was assayed using a fluorescent substrate: 1,2,bis-(1-pyrenedecanoyl)-*sn*-glycero-3-phosphocholine (BisPy-PC) that is labeled with two pyrene fluorophores, one at the end of each of the two acyl chains. The two pyrenes in close proximity to each other emit a strong eximer (excited dimer) signal at 470 nm, and the monomer profile has double maxima at ~380 and ~396 nm (Figure 8).
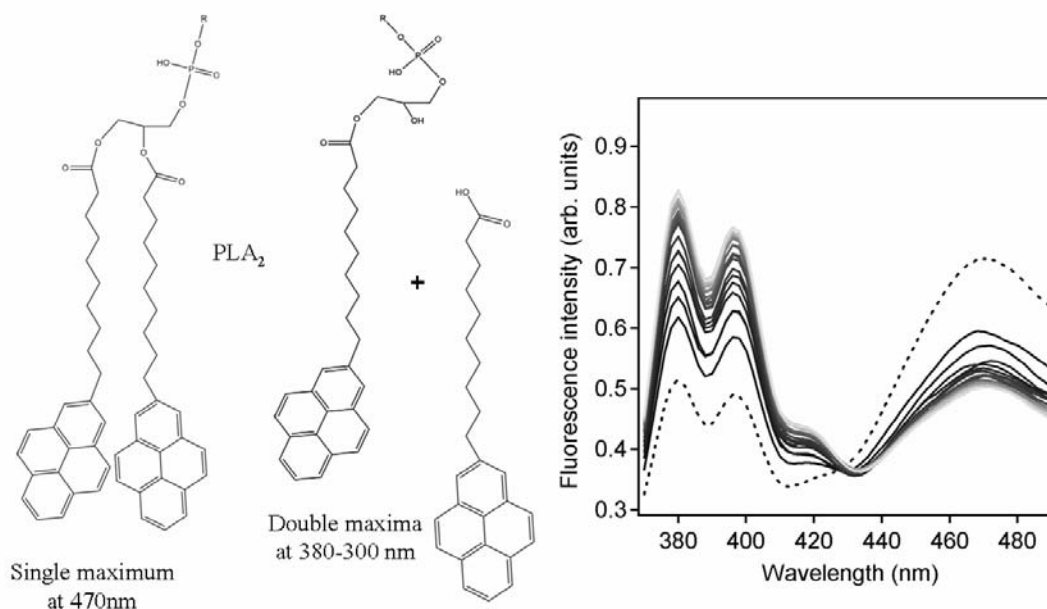
Figure 8 Bis Pyrene
Products of PLA_2 hydrolysis and representative time dependent emission spectra. The initial spectrum before the addition of enzyme is shown as a dotted line and spectra after the addition of

enzyme as solid lines with decreasing intensity for later timepoints. Refer to the body of text as well as appendix A:Bis-Py for further details.

The progress of phospholipid hydrolysis by PLA_2 can be followed by the decrease in the fluorescence intensity at 470 nm and the concurrent increase in the fluorescence intensity at 380 nm [81]. There is not a 1:1 correlation with the increase of monomer signal and concurrent decrease in eximer signal, therefore, enzyme activity is graphically represented as a change in $R_t/R_0 - 1$ over time, where R is the ratio of fluorescence intensities at 380 and 470, and the subscripts 0 and t refer to the ratio at initial and timepoint t, respectively. It should be noted that the monomer to excimer ratio, R, is dependent not only on the total concentration of pyrene, but also the variable half life of the excited-state (Molecular probes manual). The experimental parameters were: 5 mol% of BisPy-PC incorporated into extruded vesicles, in a 50 mM HEPES buffer (pH 7.5), 50 mM NaCl, 1 mM EGTA, 2.2 mM $CaCl_2$. The composition of LUVs was either 80:15 POPC:POPG or pure DPPC, at a final lipid concentration of 0.5 mM. An initial spectra of the substrate was recorded, and the reaction initiated by the addition of enzyme. Excitation wavelength was 347 nm and consecutive emission spectra were recorded between 370 and 490 nm.

Membrane binding measurements by FPE fluorescence This assay is based on the sensitivity of FPE fluorescence to the ionization state of the carboxyl group of fluorescein such that deprotonation increases the emission intensity. When the fluorescein moiety of FPE is located at the interface of a negatively charged membrane, the interfacial environment is more acidic than the bulk phase due to the electrostatic attraction of protons to the anionic membrane. This causes a partial protonation of the carboxyl group of fluorescein, and an attenuation of maximum fluorescence intensity. Adsorption of a cationic protein to the membrane locally reduces the negative surface charge, increasing the emission intensity of proximal fluorescein

moieties. Thus, binding affinity can be calculated from the change in fluorescence intensity, brought about by this deprotonation of fluorescein, as a function of increasing protein concentration [81; 85; 86]. Experimental parameters: 2 mol% FPE was incorporated into 100 nm extruded LUVs composed of 58:40 POPC:POPG (40% PG). The total lipid concentration was 0.175 mM, suspended in 10 mM HEPES buffer (pH 7.4 at 25 °C), 1 mM NaN_3, 1 mM EGTA in a 0.4 cm cuvette, with 4 optically transparent faces. Excitation was at 490 nm, and emission spectra were recorded between 500 and 540 nm, at 25 °C. Excitation and emission slits were 4 and 10 nm, respectively. After recording an initial spectrum of LUV in the buffer, 1 μL aliquots of protein were successively added to the lipid suspension, equilibrated with constant stirring for 2 minutes, and spectra recorded for each protein concentration, [P]. Changes in the peak fluorescence intensity, ΔF, were determined for each [P]. In control experiments, the lipid suspension was diluted stepwise by 1 μL aliquots of buffer, in order to correct the values of ΔF for the effect of dilution on the intensity of FPE emission. For details and comprehensive equations pertaining to data analysis, see Appendix A: FPE.

Membrane binding measurements by RET Binding of the full-length hIB PLA_2, the hIBΔN10 fragment, and the N10-hIB peptide to vesicle membranes was measured by resonance energy transfer (RET) from Trp (for full-length hIB PLA_2 and N10-hIB peptide) or Tyr (for the hIBΔN10 fragment) residues to Py-PE, which was present in membranes at 2 mol%. Vesicles, composed of different proportions of POPC:POPG, were titrated into the protein solution, with continuous stirring, to yield a total lipid concentration from 10 μM to ~1.0 mM. We used a low salt buffer containing EDTA (10 mM HEPES pH 7.4, 1mM EDTA) to prevent lipid hydrolysis during the experiment, and to avoid suppression of electrostatic protein-membrane interactions by high salt concentrations. After each addition of vesicles, the sample was equilibrated for two

minutes with stirring, and emission spectra were recorded. The concentration of N10-hIB peptide and full-length hIB PLA$_2$ was 4 µM while the hIBΔN10 fragment was used at 10 µM concentration. The single tryptophan of the full-length hIB PLA$_2$ or of the N10-hIB peptide was excited at 290 nm and the tyrosines of hIBΔN10 fragment were excited at 275 nm. Parallel control experiments have been conducted in which unlabeled vesicles (without Py-PE) were used to titrate the protein solutions. In these control experiments, protein binding to the vesicles resulted in an increase in the fluorescence emission intensity and/or a blue shift, whereas in RET experiments with Py-PE-labeled vesicles, the emission intensity of the donor decreased and that of the acceptor increased upon addition of vesicles due to energy transfer from Trp or Tyr to Py-PE. Since RET results from short-range (typically 20-30 Å) dipole-dipole interactions between the energy donor and the acceptor [87], detection of RET indicates binding of protein molecules to vesicle membranes.

Tryptophan fluorescence quenching by acrylamide and 10DN Trp emission spectra were measured in the absence or presence of varying concentrations of acrylamide, and maximum fluorescence intensities were determined. The ratio of fluorescence intensities without and with quencher (F_0/F) was plotted against the acrylamide concentration. The slopes of the best fit linear plots were used to determine the Stern-Volmer quenching constants (K_{SV}). In dual quenching experiments, Trp emission intensity was measured in the presence of lipid vesicles with no quencher, in the presence of vesicles with 250 mM acrylamide in the buffer, and in the presence of vesicles containing 10 mol% 10-doxylnonadecane (10DN) with no acrylamide in the buffer, and the dual quenching ratio, R_{DQ}, was determined (Appendix A:DQ). The quenching experiments were performed in a buffer of 50 mM HEPES (pH 7.4) and 1 mM EDTA,

containing 0.5 mM total lipid and 4 µM total protein. Excitation was at 290 nm, and temperature was 25 °C.

Fluorescence quenching by brominated lipids Bromine (Br_2), a natural quencher of fluorescence emission, has been incorporated into the (6,7), (9,10) or (11,12) positions of 1-palmitoy-2-stearoyl-(n,n+1)dibromo-*sn*-glycero-3-phosphocholine (Br_2-PC). The distance of the bromines from the membrane center, calibrated from X-ray diffraction experiments [88] are: 11.0, 8.3, and 6.5 Å for the (6-7), (9-10) or (11-12) Br_2-PC respectively. These molecular rulers were used to determine the depth of insertion of the tryptophan residues into the membrane. Distribution analysis (DA) was employed to calculate depth from the quenching data (Appendix A: DA). Experimental parameters: extruded vesicles composed of 25 mol% of Br_2-PC, 25% POPC and 50% POPG in 50 mM HEPES buffer (pH 7.4, at 25 °C), 1mM EGTA, 1 mM final lipid concentration. Controls were 1:1 POPC:POPG LUVs without Br_2-PC. The final protein concentration was 0.4 µM. Excitation wavelength was 290 nm and emission spectra were recorded between 300 and 400 nm.

Direct transmission FTIR and Attenuated Total Reflection FTIR Direct transmission Fourier transform infrared spectroscopy (FTIR) and polarized attenuated total reflectance FTIR (ATR-FTIR) experiments were carried out using a Vector 22 FTIR spectrometer (Bruker Optics, Billerica, MA). For direct transmission experiments, the lyophilized protein was dissolved in a D_2O (deuterated water) based HEPES buffer and immediately assembled between two CaF_2 windows, with a 25 µm spacer, and spectra were recorded at varying timepoints for 1 hour. Spectra of proteins in H_2O based HEPES buffer were collected using a 6 µm spacer. For ATR experiments, a model 611 Langmuir-Blodgett trough (Nima, Coventry, UK) was used to deposit a POPC monolayer on a germanium internal reflection plate (Spectral Systems, Irvington, NY).

The plate was then assembled into an aluminum flow cell and sonicated vesicles, composed of 70:30 POPC:POPG (30% PG), were injected to form supported phospholipid bilayers. Excess lipid was removed by gently flushing with H_2O buffer. The protein, suspended in H_2O based HEPES buffer was then injected into the ATR cell and permitted to adsorb to the membrane for ~15 min, and spectra at parallel and perpendicular polarizations were recorded. The chamber was gently flushed with 5 mLs of D_2O-based buffer of the same composition and spectra were collected at parallel and perpendicular polarizations for 1 hour. For both direct transmission and ATR-FTIR, time zero was set at first exposure of the protein to D_2O. All spectra were processed and analyzed using Grams/AI V7 software suite (ThermoGalactic, Salem, NH). For second derivative spectra, secondary structure evaluation and kinetics of hydrogen-deuterium exchange (HDX), polarized spectra were first corrected in order to obtain polarization independent spectra by spectral addition using the formula:

$A = A_{||} + 0.8A_{\perp}$

where the corrected absorbance, A, is the sum of the spectrum at parallel polarization and the spectrum at perpendicular multiplied by a scaling factor, 0.8 in these experiments. Amide I and amide II components were identified by curve-fitting using the number and positions of the inverted second derivative peaks as peak centers, and relevant maximum and minimum values for peak height and width parameters. The results of curve-fitting were considered satisfactory when the peak frequencies of all components were within a ± 1 cm^{-1} range of the input frequencies, and when the sum of all components was coincident to the measured spectrum.

CHAPTER THREE: RESULTS

Mutation, expression and purification of hIIA PLA$_2$ PCR primer directed mutation of the N1A hIIA PLA$_2$ gene effectively yielded two mutants incorporating a tryptophan into the 3rd and 5th positions, confirmed by DNA sequencing (data not shown). The modified expression protocol yielded 30, 5 and 25 mg of protein per liter of bacteria culture for the hIIA PLA$_2$, V3W and F5W proteins respectively. The high yield enabled the calculation of the unique extinction coefficient (ε_{280}) for each protein from physical measurements. The resultant extinction coefficients were 10,338 M^{-1} cm^{-1} for hIIA PLA$_2$, 11,416 M^{-1} cm^{-1} for V3W, and 15,486 M^{-1} cm^{-1} for F5W. The two step purification by column chromatography yielded very pure protein samples, which are required for structural analysis. Purity was confirmed by silver stained SDS-PAGE, and specific activities determined using the Cayman sPLA$_2$ activity kit. Only the highly active fractions were pooled, dialyzed against pure water, lyophilized and stored at -80 $^{\circ}$C. The elution of hIIA PLA$_2$ from the Superdex size exclusion column consistently ran as a double peak. 15% SDS-PAGE of the peak fractions revealed proteins of similar size, but markedly different activities. The specific activities from the first peak fractions were negligible, but were substantial in fractions from the second peak, corresponding to longer retention times. The Superdex elution profile of a representative expression of hIIA PLA$_2$, the corresponding silver stained gel and specific activities of each elution fraction and. an overlay of representative elution profiles of hIIA PLA$_2$, V3W and F5W are shown in Figure 9. The V3W eluted with a similar profile as the hIIA PLA$_2$, only shifted toward longer retention times. The F5W mutation eluted as a single broad peak around 85 mL, corresponding to the active fraction of the hIIA PLA$_2$, but demonstrated virtually no activity, therefore only fractions at the center of the peak were pooled and lyophilized.
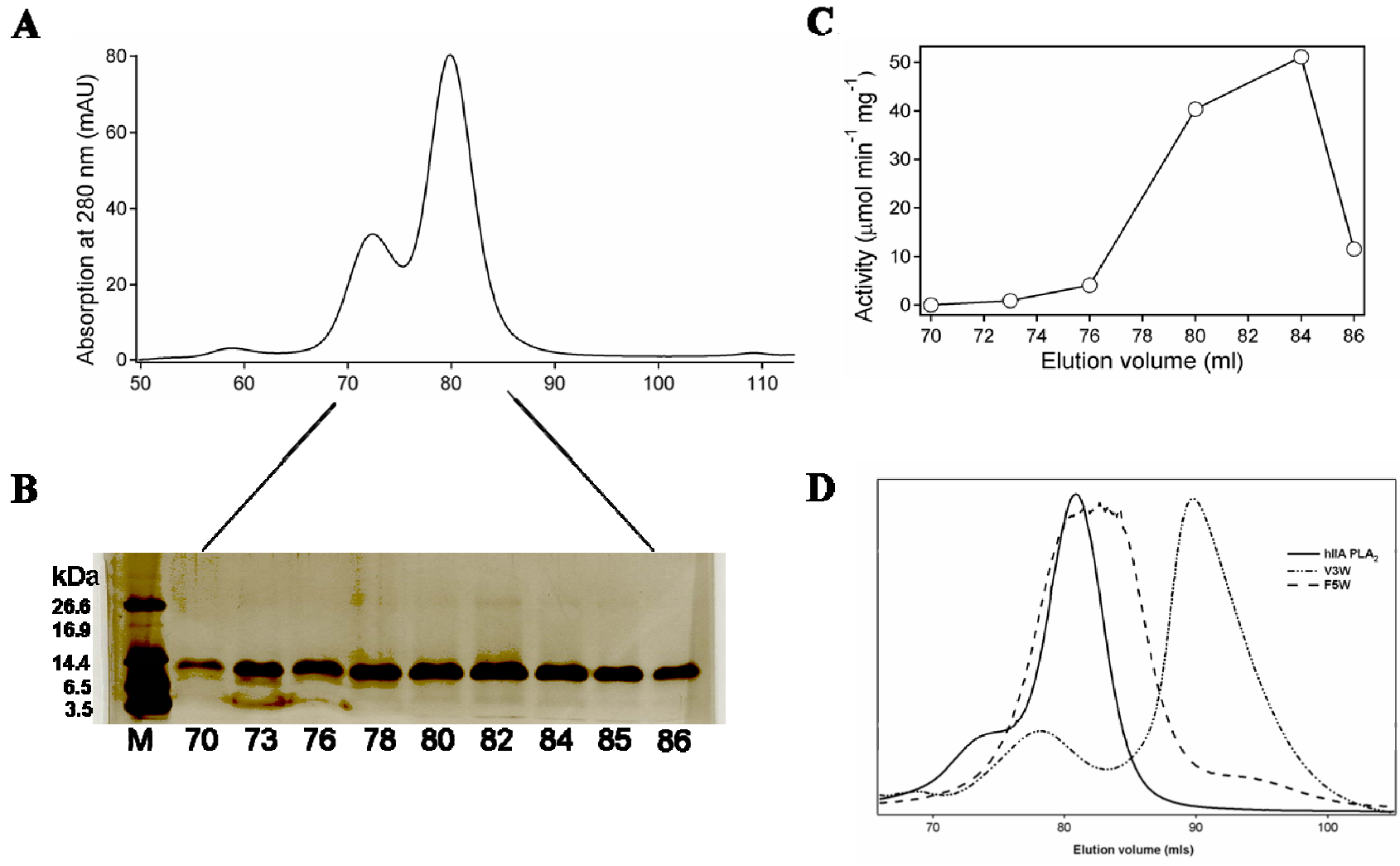
Figure 9 Elution Profile

Additional purification by the Superdex size-exclusion column allowed us to produce highly pure and active PLA_2 samples A) Representative hIIA PLA_2 elution profile, B) silver stained gel of the indicated peak fractions C) activity levels for the respective fractions and D) Overlay of elution profiles for hIIA PLA_2 (solid line), V3W (broken line) and F5W (dashed line)

PLA₂ activity against lipid micelles Comparison of the activities of hIIA PLA$_2$, V3W, F5W and hIB PLA$_2$ toward DHTPC micelles indicated a four fold increase in activity for V3W as compared to hIIA PLA$_2$, and a complete loss of activity for F5W. The rate of the hIB PLA$_2$ was ~35% of the hIIA PLA$_2$ (Figure 10, Table 4). Enzymatic activities of the hIBΔN10 fragment and the chimeric hIIA/IB PLA$_2$ were also assayed using the same parameters. The activity of hIBΔN10, was ~1% of hIB PLA$_2$ (data not shown) and the activity of the chimeric hIIA/IB PLA$_2$ was ~40% of the full-length hIB PLA$_2$ (Figure 10B). The kinetic curves obtained with this assay were linear over at least 10 minutes for all enzymes except V3W. The V3W curve indicates a reduction in lipid hydrolysis as a result of substrate exhaustion, demonstrated by the resumption of the high catalytic activity upon addition of fresh substrate (data not shown).

Although group I/II sPLA$_2$s normally show little activity towards zwitterionic PC membranes, they are active against DHTPC micelles because of their small radius of curvature. The greater curvature is proposed to alleviate surface binding constraints and facilitate the transfer of substrate from micelle to enzyme [89; 90]. The presence of BSA, a fatty acid 'sink' and the conversion of the lysophospholipid in the liberation of the reporter eliminates any contribution to enzyme activity by the build up of negative charge or possible disruption in the micellar surface. In addition, because the concentration of substrate is much higher than the concentration of enzyme, nearly complete binding of enzyme can be assumed. From the kinetic scheme (Figure 6) we can assume that the parameters of this assay have been optimized in order to assess just the catalytic activity of the enzyme. Therefore, the changes in catalytic rate for the V3W or F5W mutant implies either i) a structural change disrupting the catalytic mechanism in the enzyme brought about by the mutation, possible for the internal Trp[5] but unlikely for the external Trp[3]; ii) a change in substrate accessibility or binding to the active site by steric interactions, again a

33

possibility for Trp[5]; or iii) a change in the mode of binding to the micelles, possible for either enzyme as the tendency for tryptophan to sit at the lipid-water interface may initiate an orientational difference between the binding of hIIA PLA$_2$ and the Trp mutants to the micelles.
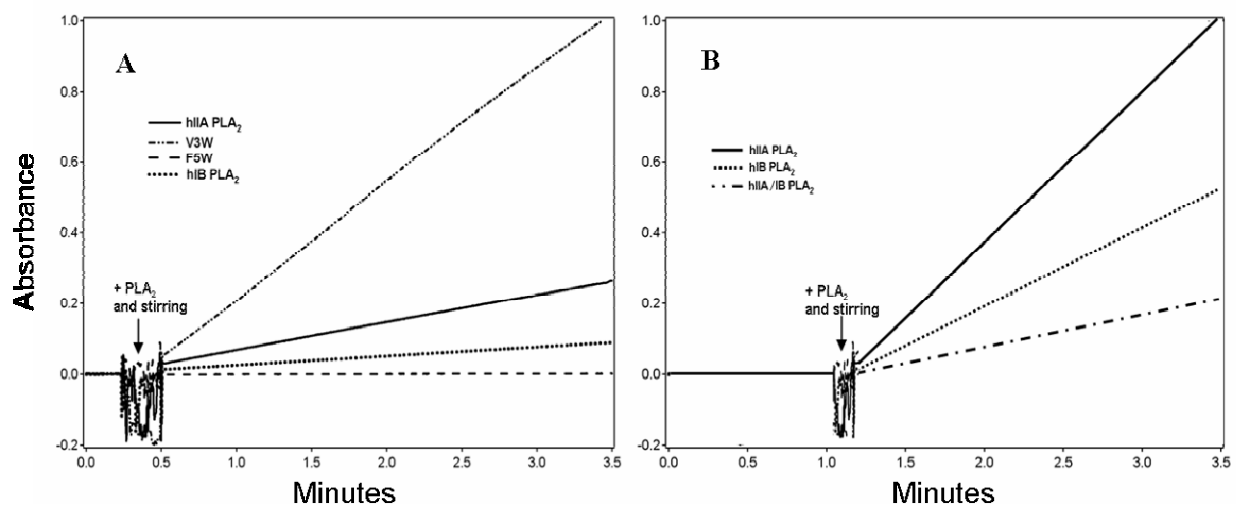
Figure 10 Activity against lipid micelles
A) Activity profile of hIIA PLA$_2$ (solid line), V3W (broken line), F5W (dashed line), and hIB PLA$_2$ (dotted line) final protein concentration was 0.35 µg/mL B) Relative activity of hIIA PLA$_2$ (solid line), hIB PLA$_2$ (dotted line) and chimeric hIIA/IB PLA$_2$ (dash dot) under the same assay conditions as in (A), but with non standardized protein concentrations, therefore curves represent only the relative activity of the chimeric to the parent enzymes.

The low activity of the hIBΔN10 fragment, which lacks the N-terminal helix, may result from several factors also: i) loss of part of the substrate-binding pocket; ii) weaker membrane binding; iii) improper orientation at the membrane surface; or iv) distortion of the structural integrity of the molecule by breaking intramolecular H-bonding and nonpolar interactions. The reduced activity of the chimeric hIIA/IB PLA$_2$ compared to both the hIB PLA$_2$ and hIIA PLA$_2$ indicates that subtle changes in the sequence of the N-terminal helix have significant effect on the enzyme behavior, which underscores the functional importance of the N-terminal helix of group I/II PLA$_2$s.

PLA$_2$	DHTPC micelles	Bis-PyPC activity vs 100% DPPC @38 °C			Bis-PyPC activity vs 15%PG		
	Specific activity umol*min^{-1}*mg^{-1}	initial rate ΔAu/min	intermediate ΔAu/min	max rate ΔAu/min	initial rate ΔAu/min	intermediate ΔAu/min	max rate ΔAu/min
hIIA	3.06	0	0.003 (v_1) 0.03 (v_2)	0.25	0.006	-	0.039
V3W	12.15	0.012	0.1	0.52	1.33	.4 (v_1) .1 (v_2)	0.031
F5W	0.045	0	0	0	0.003	0.009	0.024
hIB	1.07	0	0.18	0.89	0.007	-	0.039

Table 4 PLA$_2$ catalytic activity
The specific activity as measured by the Cayman sPLA$_2$ kit is presented in the first column as μmol per min per mg of enzyme. The activity measured by BisPy-PC labeled vesicles is presented as a relative change, and is given as a change in absorbance over time.

PLA$_2$ activity against lipid bilayers The activities of hIIA PLA$_2$, V3W, F5W and the full length hIB PLA$_2$, were also measured against large unilamellar vesicles (LUVs) labeled with 5 mol% of 1,2,bis-(1-pyrenedecanoyl)-*sn*-glycero-3-phosphocholine (BisPy-PC) in extruded vesicles of pure DPPC, and also against extruded vesicles of 80:15 POPC:POPG (15% PG). The concentration of anionic lipids is near the lower limit of noticeable activity for hIIA PLA$_2$ (18%), in order to separate the kinetic effects due to enhanced binding from the effects due to catalytic efficiency. The hydrolysis of the *sn*-2 bond of the BisPy-PC labeled phospholipids effectively separate the pyrene moieties at the respective ends of the *sn-2* fatty acid and the *sn*-1 lysophospholipid. The hydrolysis was monitored by a reduction in the eximer signal at 470 nm and a parallel increase in the monomer signal at 380 nm. As hIIA PLA$_2$ did not demonstrate any activity toward DPPC LUVs at 25 °C, (in the solid gel phase) for up to 1 hour following PLA$_2$ addition (data not shown), the temperature was increased to 38 °C, close to the gel to liquid-crystal phase transition temperature of DPPC (T$_m$ = 41.5 °C).

Under the conditions near T$_m$, the hIIA PLA$_2$ demonstrated a complex kinetic profile, showing a lag period of approximately 5 min, followed by ~10 minutes of intermediate activity, then a burst of high activity at ~15 minutes. The kinetic profile for V3W showed a brief (2-3 min) intermediate activity followed by very high activity, without a measurable lag time, however the steady state activity was two times the steady state rate of hIIA PLA$_2$. The hIB PLA$_2$ had nearly the same profile as V3W, but with a lag period for the first minute, and an intermediate activity for ~1 min before a burst of activity. The steady state rate for hIB PLA$_2$ was similar to V3W. F5W demonstrated no activity in this assay. Qualitatively different results were obtained with 15% PG LUVs. In this case, hIIA PLA$_2$ and hIB PLA$_2$ had a 1.5 min lag phase, followed by a moderate level of activity. V3W demonstrated very high activity immediately, without any

apparent lag, to a level of ~30 times the maximum rate of hIIA PLA_2, before resolving to a much slower steady state rate.

Surprisingly, F5W showed a ~1.5 minute lag period and a subsequent moderate rate of activity that continued to the end of the assay. The steady state for V3W, hIIA PLA_2 and hIB were approximately equivalent, with F5W at ~ 60% of hIIA PLA_2. Figure 11 presents the kinetic profiles of the three IIA enzymes and includes hIB PLA_2 as a reference for the native Trp^3 in two conditions: against 100% DPPC at 38 °C and against 15% POPG vesicles at 25 °C. The relative rates of activity for each of the rate transitions are presented in Table 4, as a change in absorbance over time.
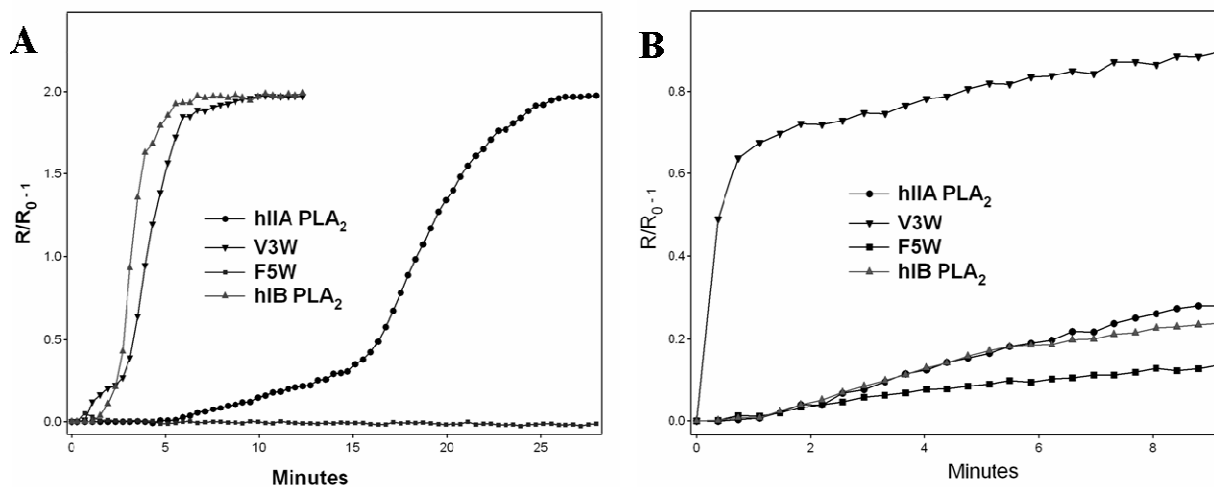
Figure 11 Activity against Lipid bilayers
Activity profiles: A) 100% DPPC at 38 °C and B) 15% POPG, 85% POPC. 2% Bis Pyrene PC was incorporated into the extruded vesicles.

Our data are consistent with earlier findings describing interfacial activation: group hIIA PLA_2 shows no activity against PC membranes in the gel phase (T << Tm) but demonstrates activity near T_m [71; 91]; On zwitterionic (PC) membranes, the onset of high activity of hIIA PLA_2

37

was preceded by a lag phase, which has been interpreted earlier to result from gradual accumulation of the anionic reaction products in the membrane [71; 75; 91]. The lag phase was shown to become shorter and then disappear with increasing fractions of anionic lipids [75; 92]. In a recently published work, hIIA PLA$_2$ preferentially hydrolyzed the liquid phase of a mixed phase substrate, generating a localized increase in negative charge through product accumulation [93]. All existing data suggest that the burst of activity that follows the lag phase is a result of the recruitment of more PLA$_2$ molecules to the membrane. If the sole effect of the presence of Trp^3 in the IBS of V3W is enhanced binding to zwitterionic membranes, and the burst of activity is a result of more enzyme binding, then the reduction or lack of lag phase can be attributed to a greater number of V3W enzymes binding initially. However, Burack et al., 1995[92], demonstrated the bulk of a snake venom group IIA PLA$_2$ was "associated with the membrane at a time well before the abrupt increase in catalytic rate", revealing an inactive membrane bound state. Without quantitative results demonstrating bound and unbound enzyme, binding can only be confirmed by the presence of catalysis, but the absence of catalysis is not necessarily indicative of the lack of bound enzyme. Nevertheless, the establishment of a steady state rate indicates an equilibrium between bound and unbound states of PLA$_2$. Therefore the steady state rate can be viewed as a measure of specific activity alone, or a combination of the rate of binding of a single substrate to the active site, the rate of catalysis, and the rate of product dissociation. The steady state rate for V3W was approximately twice that of hIIA PLA$_2$ on 100% DPPC (38 °C) or nearly identical on 15% PG. It is interesting, that the steady state rate for the hIB PLA$_2$ enzyme was slightly higher (1.7x) than the V3W on 100% DPPC (38 °C), but was similar to V3W on 15% PG. It is also interesting to note that the kinetic profile of V3W on 15% PG could be viewed as an inverse of a lag phase and

subsequent burst of activity. In this light, the increase in product accumulation appears to reduce the rate of activity of V3W to approximate that of the wild type enzyme.

The results presented here are in accord with that published earlier on the V3W mutant. Neglecting the bias caused by aggregation, the earlier experimental results ascribe the changes in binding affinity and activity of V3W [73; 74] to the affinity of tryptophan for membrane interfaces re: V3W is active against aggregated zwitterionic substrate where hIIA PLA$_2$ is not. The rates on other substrates are inconsistent, resulting in ambiguity as to the exact nature of the change, though what was extrapolated was a large increase in activity on low anionic substrates and a modest increase or decrease on high anionic substrates, leading to the conclusion that there must be a multiplicity of effects arising from electrostatic and hydrophobic forces.

As in the Cayman assay, the possible mechanism for the change in catalytic activity of F5W could be i) a structural change caused by the introduction of Trp^5 into the substrate binding pocket; ii) interference in entrance of the phospholipid into the substrate-binding cleft because of bulkier side chain of Trp^5; or iii) a altered mode of membrane binding to the substrate caused by the mutation.

Because binding to the aggregated substrate is the initial step leading to interfacial activation, we will evaluate several aspects of membrane binding: the strength of membrane binding, the mode of membrane binding, the depth of insertion into the membrane, conformational changes induced by membrane binding and finally orientation of the bound enzyme to the membrane.

Strength of PLA$_2$ membrane binding Obtaining an unambiguous dissociation constant (K$_D$) for membrane binding by hIIA PLA$_2$ is problematic. The enzyme does not bind to zwitterionic membranes, and conversely, the binding of anionic membranes is not only strong, but the distribution of positively charged residues over the whole enzyme, not just across the IBS, induces very large, multiple vesicle aggregates [94]. These aggregates promote light scattering, strongly obstructing spectroscopic experiments in the UV region. For example, CD spectra of 0.8 mg/mL hIIA PLA$_2$ with increasing concentrations of 1:1 diether POPC:POPG LUVs in phosphate buffer, resulted in a strong reduction of protein signal by ≥1 mM lipid concentration (Figure 12).
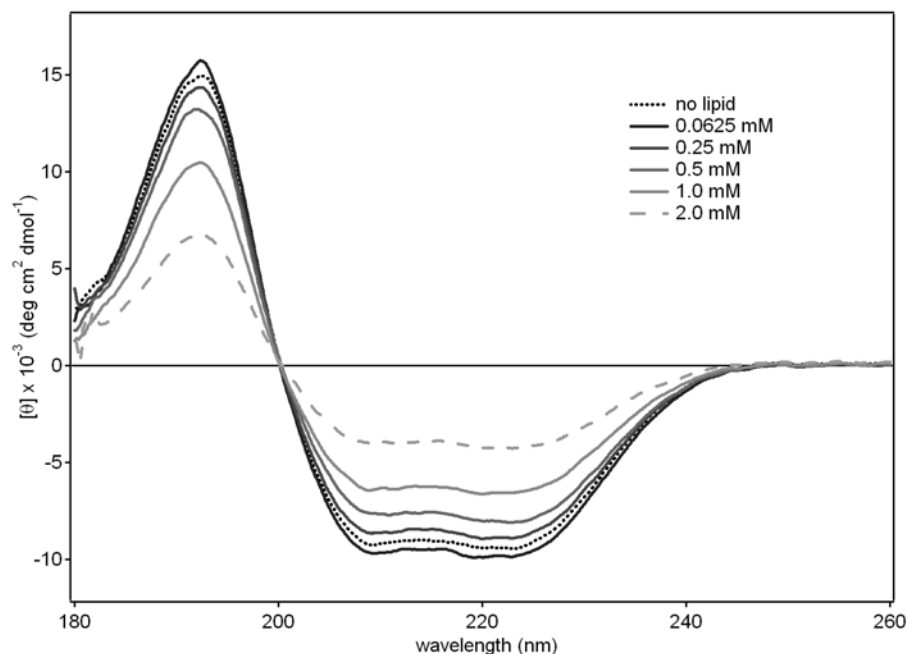
Figure 12 Lipid aggregation effects
CD spectra of 0.8 mg/mL hIIA PLA$_2$ with increasing concentrations of 50% di-ether POPC:POPG. The initial spectrum before the addition of lipid is shown as a dotted line, and subsequent spectra with increasing concentrations of lipids are shown as solid lines decreasing in intensity, with the final spectrum as a broken line.

Vesicle aggregation can be minimized by different strategies, such as high ionic strength buffer, membranes with moderate fraction of anionic lipids, or appropriate protein to lipid molar

ratios. We have used membranes of 58:40 POPC:POPG, (40% PG) with 2 mol% of FPE, at relatively low total lipid concentrations: 175 μM. The protein concentration was gradually increased in increments that yielded measurable changes in the FPE fluorescence signal, yet did not cause significant vesicle aggregation. Aggregation was monitored by the increase in light scattering at right angle at 600 nm (data not shown).

The change in fluorescence was corrected for dilution effects and plotted as a function of protein concentration. Using the formulation found in Appendix A: FPE, theoretical binding isotherms were constructed and corresponding values for K_D and N (the numbers of lipid molecules per protein binding site) were derived, [81]. See appendix A:FPE for further explanation of N. Representative spectra demonstrating the increase in fluorescence due to protein binding, the decrease in intensity due to dilution and the binding isotherms are presented in Figure 13.

The numerical parameters for K_D and N, of hIIA PLA_2, V3W, F5W, hIB PLA_2 and the two synthetic peptides, N10-hIIA and N10-hIB, as well as the chimeric hIIA/IB PLA_2 determined by FPE fluorescence are given in Table 5. Although this procedure yields slightly different values of N for the three group IIA proteins, they are still within a reasonable range of 30-40 lipids per membrane-bound PLA_2 molecule, and are in good agreement with earlier data [81; 83; 95]. The lack of binding of hIIA PLA_2 to zwitterionic membranes, and strong binding to anionic membranes are indicative of a significant electrostatic component in PLA_2-membrane interactions, consistent with earlier data [74; 83; 94; 96; 97].
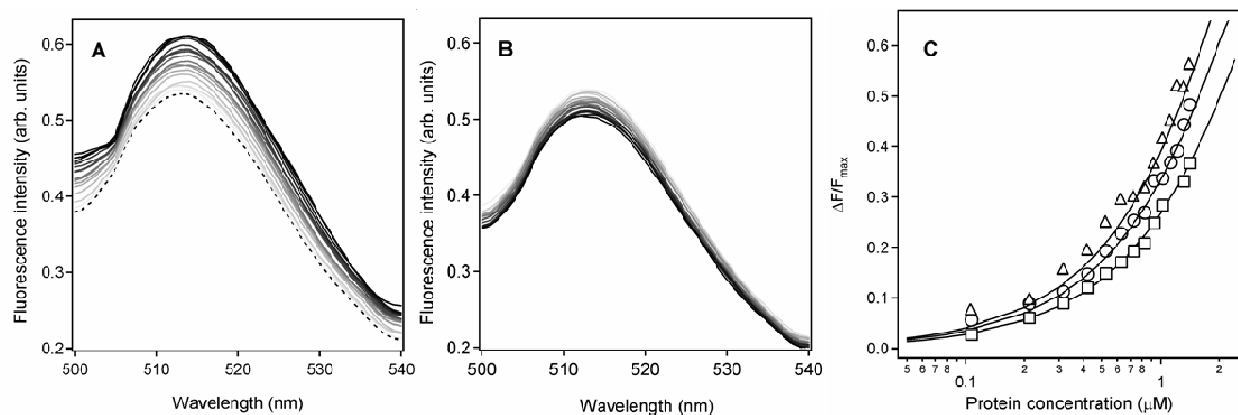
Figure 13 FPE binding curves.
A) Representative spectra of the increase in fluorescence of FPE upon addition of protein. The initial FPE emission spectrum before the addition of protein is represented by the dotted line, and subsequent spectra by solid lines, increasing in intensity, the lightest having the lowest concentration of protein, and the darkest, the highest. B) Dilution effects on fluorescence intensity, again lightest to darkest intensity represents subsequent dilutions, with the darkest at the greatest dilution. C) Simulated binding isotherms of the IIA proteins using the calculated K_D and N values. Experimental data points for hIIA PLA_2 are represented as circles, for V3W as triangles and for F5W as squares.

Table 5 FPE Binding Parameters

PLA$_2$	20% POPG		40% POPG		Change in K_D
	K_D µM	N	K_D µM	N	Fold
hIIA PLA$_2$	2.75	36	0.3	36	9.2
V3W	-	-	0.17	40	-
F5W	-	-	0.5	30	-
hIB PLA$_2$	6.04	36	1.4	36	4.3
IB-N10 peptide	2.5	9	0.6	9	4.2
IIA-N10 peptide	5.72	9	2.5	9	2.3
hIIA/IB PLA$_2$	10.0	36	1.8	36	5.5

Binding parameters K_D and N determined by FPE labeled LUVs containing either 20 or 40 mol% of POPG, and the change in K_D seen with the increase in anionic lipid (last column).

The dissociation constant of hIIA PLA$_2$ for membranes containing 40% PG (K_D = 0.3 µM), is in good agreement with earlier results obtained under similar conditions [81]. In other studies, using different experimental approaches, e.g. sucrose-loaded vesicle centrifugation method, [74] it is reported that hIIA PLA$_2$ did not bind to PC or even to membranes of 82:18 PC:PS (18% PS), but V3W did bind to 18% PS with a K_D of 0.21 mM. On the other hand, using the sucrose-loaded vesicle method, Bezzine et al., 2002 [75] report a nearly 100-fold stronger binding (in terms of K_D) of the V3W mutant to 80:20 POPC:POPS membranes than hIIA PLA$_2$ (K_{DV3W} = 2.6 µM, K_{DhIIA} = 230 µM). Where our data show only a 2-fold stronger binding affinity for anionic membranes of V3W than hIIA PLA$_2$, the anionic lipid in our study is POPG, the major anionic lipid in bacterial membranes, a native substrate for the antimicrobial hIIA PLA$_2$. Singer, 2002, [52] reports a preference of hIIA PLA$_2$ for POPG over POPS, presented as a five fold increase in specific activity toward phospholipid vesicles composed of a single type of lipid: PG or PS. In spite of large quantitative differences in the absolute values of K_D found in the collective hIIA PLA$_2$ data (a possible reflection of varying methods and experimental conditions as well as aggregation effects), what is consistently reported, is an enhancement of membrane binding toward zwitterionic vesicles upon introduction of a single, site specific tryptophan into the interfacial binding surface of hIIA PLA$_2$. Although there are no published data to compare with, we report a weaker binding to anionic membranes of F5W than hIIA PLA$_2$, and interpret the impaired membrane binding in terms of structural perturbations upon interaction with the interface.

Interestingly the K_D for the chimeric hIIA/IB PLA$_2$ was 1.8 µM, indicative of weaker binding. The weaker binding could be the sole cause of the lower activity of the chimeric protein

against micelles, however does not rule out structural perturbations or orientational changes due to the different membrane interacting residues

Binding of the hIB PLA$_2$ the hIB N-terminal peptide (N10-hIB) and its truncated hIBΔN10 fragment, to phospholipid vesicles was quantitatively measured by resonance energy transfer (RET) analysis. Binding of these molecules to 100% zwitterionic membranes was weak and difficult to measure reliably. Therefore, we used large unilamellar vesicles containing 20 or 40 mol% acidic lipid, POPG. These experiments are physiologically relevant because most biological membranes contain acidic lipids within this range. Since human group IB PLA$_2$ has a single Trp at position 3, Trp fluorescence was used as RET donor in analyzing membrane binding of the full-length hIB PLA$_2$ and the N10-hIB peptide, whereas Tyr fluorescence was used in the case of the hIBΔN10 fragment (the protein has nine tyrosines between positions 22 and 123). The energy acceptor was 2 mol% 1,2-dioleoyl-sn-glycero-3-phosphoethanolamine-N-(1-pyrenesulfonyl) (Py-PE) in vesicle membranes in all cases. Titration of protein solution by increasing concentrations of unlabeled vesicles (without Py-PE) resulted in either one or both of the two effects, i.e., an increase in the fluorescence emission intensity and a blue shift. However, the protein fluorescence intensity decreased upon addition of vesicles containing 2 mol% Py-PE, evidently due to energy transfer from Trp or Tyr residues of proteins to Py-PE in vesicle membranes (data not shown). Because of the complex absorption profile of pyrene, this fluorophore can be excited by UV radiation at 270-290 nm, which was used for Tyr or Trp excitation. Therefore, we measured RET on the basis of a decrease in the emission intensity of the energy donor (Tyr or Trp residues of proteins) and not the increase in the emission intensity of pyrene. Since RET is based on short-range (20-30 Å) dipole-dipole interactions between energy

donors and acceptors [87], the observed effect reflects binding of protein molecules to vesicles membranes.

After correction of the RET data for sample dilution and for increase of emission intensity upon binding to unlabeled vesicles, binding isotherms were constructed (Figure 14) as described in Qin et al., 2004 [83]. Analysis of the RET data yielded the dissociation constants (K_D) and N, the numbers of lipid molecules per protein binding site, which are presented in Table 6.
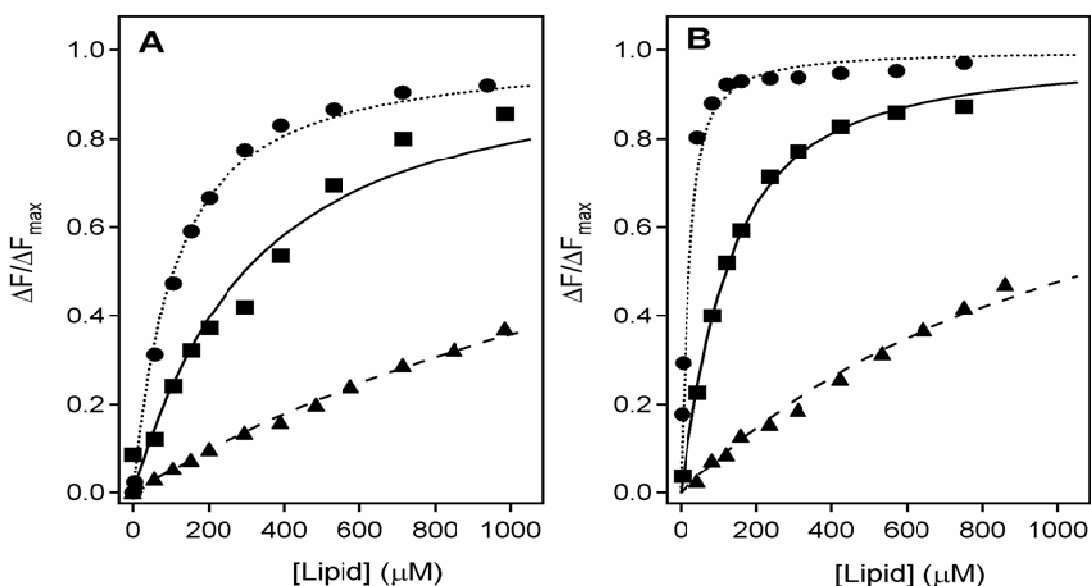
Figure 14 RET binding isotherms
Binding isotherms for hIB PLA_2 (squares), hIBΔN10 fragment (triangles) and N10-IB peptide (circles) on POPC/POPG vesicles containing A) 20% PG and B) 40% PG

These data indicate that the binding of the N10-hIB peptide to membranes is comparable with that of the full-length hIB PLA_2 protein, but the increase in the affinity of the peptide for membranes with increasing fraction of the anionic lipid is steeper compared to the full-length hIB PLA_2. On the other hand, the hIBΔN10 fragment exhibited significantly lower affinity for negatively charged membranes than the full-length hIB PLA_2 and little dependence on the

fraction of the anionic lipid in membranes. This indicates the N-terminal α-helix of hIB PLA_2 contributes to the sensitivity of the enzyme to the negative surface charge of membranes.

Table 6 RET binding parameters

| | 20% POPG | | 40% POPG | | |
	K_D	N	K_D	N	Fold Change in K_D
hIB PLA_2	3.5	36	1.1	37	3.2
IB-N10 peptide	5.8	8	0.65	9	8.9
IBΔN10 fragment	29.0	30	18.5	28	1.6

Determination of K_D by RET, affinity increases with greater fraction of anionic lipids.

The total surface of the IBS of hIB PLA_2 is roughly 1700 Å^2, and the N-terminal helix of hIB PLA_2 provides four residues for the IBS, i.e. Trp^3, Arg^6, Lys^7, and Lys^{10} [60]. Using the accessible areas of 255, 225 and 200 Å^2 respectively for tryptophan, arginine and lysine [98], and assuming that the residues can provide at most half of their total accessible surface area for interaction with membranes, we estimate that the maximum contribution of the four hIB N-terminal residues in the total area of IBS is $0.5(255 + 225 + 400)/1700 \approx 0.26$, i.e., roughly one-fourth of the IBS area is provided by the residues of the hIB N-terminal α-helix. This estimate is supported by the fact that the number of lipids per protein binding site is 36-37 for the full-length hIB PLA_2 and 8-9 for the N10-hIB peptide (Table 6). Thus, although removal of ~¼ of the IBS impairs the membrane binding strength of the protein, the truncated hIBΔN10 fragment still retains substantial affinity for the membrane surface but loses 99% of the enzymatic activity. Apparently, besides the impaired membrane affinity there are other reasons for the dramatic

decrease in the activity of the hIBΔN10 fragment. One obvious reason is that out of six key residues that form the substrate binding pocket of the enzyme (Val[2], Phe[5], Tyr[22], Asn[23], Leu[31], and Tyr[69]) [60], two residues (Val[2] and Phe[5]) are absent in the hIBΔN10 fragment.

The quantitative differences seen between the results from the two separate binding assays are due to the assay conditions, where RET is a straightforward assay, the measurement of the energy transferred from a single Trp to pyrene, the FPE is more qualitative. The overall conclusions that can be drawn from these two assays are: there are group specific differences in binding affinity relative to anionic strength of the membrane; there are no significant differences in the binding affinity of hIIA PLA$_2$ upon either Trp[3] or Trp[5] mutation; and the N-terminal helix enhances the strength of membrane binding.

Mode of PLA$_2$ membrane binding Because fluorescence spectra are sensitive to the degree to which the fluorophores are exposed to the polar aqueous phase or are hidden in the protein body, fluorescence spectroscopy can be used to assess the local microenvironments of selectively excited fluorophores within the global tertiary structure of proteins [87]. Tryptophan fluorescence emission spectra of V3W, F5W and hIB PLA$_2$ in solution are presented in Figure 15. As the hIIA PLA$_2$ does not contain tryptophan, it is not included here. The data obtained from the IB PLA$_2$ isoform is used as a reference for the native Trp[3].
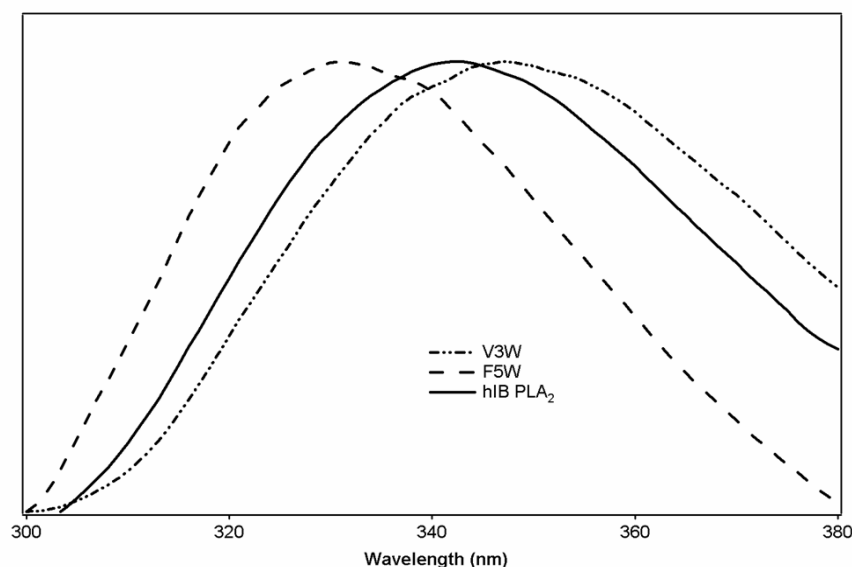
Figure 15 Tryptophan Fluorescence
Tryptophan fluorescence emission spectra of V3W (dashed-double-dotted line), F5W (dashed line) and hIB PLA$_2$ (solid line) in 50 mM HEPES buffer, pH7.4 with 1mM EDTA.

The Trp emission peak was 347, 331, and 342 for V3W, F5W and hIB PLA$_2$, respectively. Lower peak wavelengths correspond to limited exposure of the fluorophores to water and weaker solvent relaxation, resulting in greater emission energies, or frequencies ($E = h\nu$). The blueshift of F5W therefore indicates the Trp[5] is in a more protected environment than the V3W or hIB Trp[3], as expected because of its location in the substrate binding pocket. The ~5 nm difference

48

between the V3W Trp^3 and the hIB Trp^3 indicates a slightly different microenvironment for the two Trp^3 residues. Though both are exposed to solvent, the 5 nm higher wavelength of the Trp^3 of V3W compared to that of the hIB PLA_2 may indicate a more flexible structure of the V3W Trp^3 or a more extensive contact with water.

Trp fluorescence quenching experiments on V3W and F5W with increasing concentrations of the water soluble quencher, acrylamide, were performed in the presence and absence of 1:1 POPC:POPG vesicles (50% PG). Stern-Volmer plots, depicting F_0/F as a function of acrylamide concentration, were generated, and the slopes of the best-fit linear plots have been used to determine the Stern-Volmer quenching constants, K_{SV} (Figure 16).
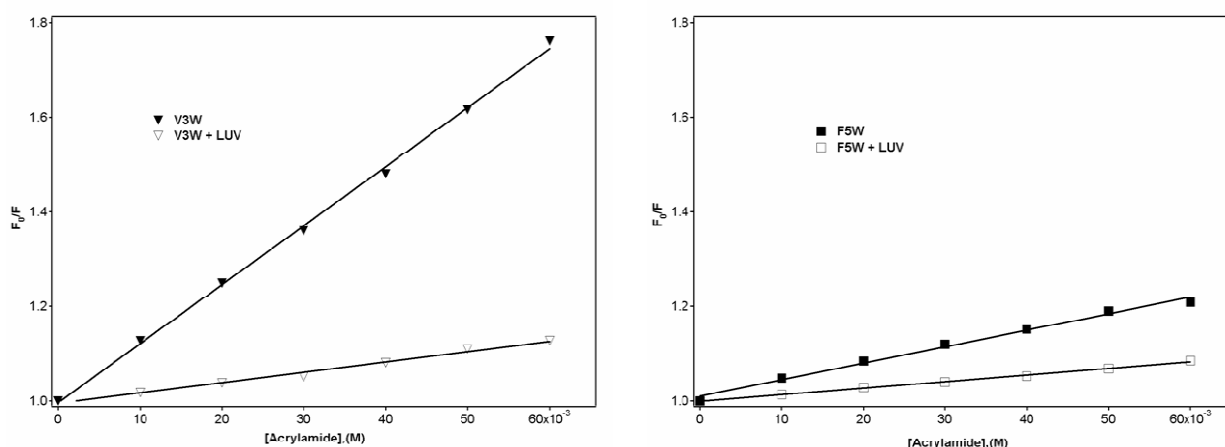
Figure 16 Acrylamide quenching
Stern-Volmer plots of Trp fluorescence quenching by acrylamide of V3W (left) and F5W (right) in the absence or presence of POPC/POPG vesicles. F_0 and F are maximum fluorescence emission intensities without and with the quencher, respectively. F_0/F decreases with the addition of lipids, indicating a reduction in quenching efficiency as Trp^3 is shielded from the aqueous quencher.

The plots demonstrate that both the Trp^3 and Trp^5 fluorescence decreases in a concentration dependent manner with the addition of acrylamide, both in the absence and presence of vesicles containing 50% POPG. The reduction in quenching efficiency in the presence of vesicles indicates an insertion of the Trp residues into the membrane, consequently

becoming partially protected from the effects of acrylamide quenching. The implication of the membrane insertion of Trp^5 is addressed below (depth of insertion results).

Fluorescence spectra of hIB PLA_2 and the N10-hIB peptide were also measured in the absence and presence of lipid vesicles composed of either pure POPC, pure POPG or with 25, 50, or 75 mol% of POPG (Figure 17). In the presence of pure zwitterionic POPC vesicles, there was little change in the peak position of hIB Trp^3 fluorescence from the peak position in the presence of acrylamide alone, confirming that hIB PLA_2 does not bind appreciably to zwitterionic membranes. With increasing proportions of POPG however, the peak fluorescence wavelength (λ_{max}) decreased in a sigmoidal manner, with a max change of ~10nm in the presence of vesicles composed of 100% POPG. The blueshift (decrease in wavelength) of the λ_{max} is indicative of the microenvironment of the hIB Trp^3 changing from a polar aqueous phase, to a less polar environment such as a dehydrated protein-membrane interface, or hydrophobic membrane.
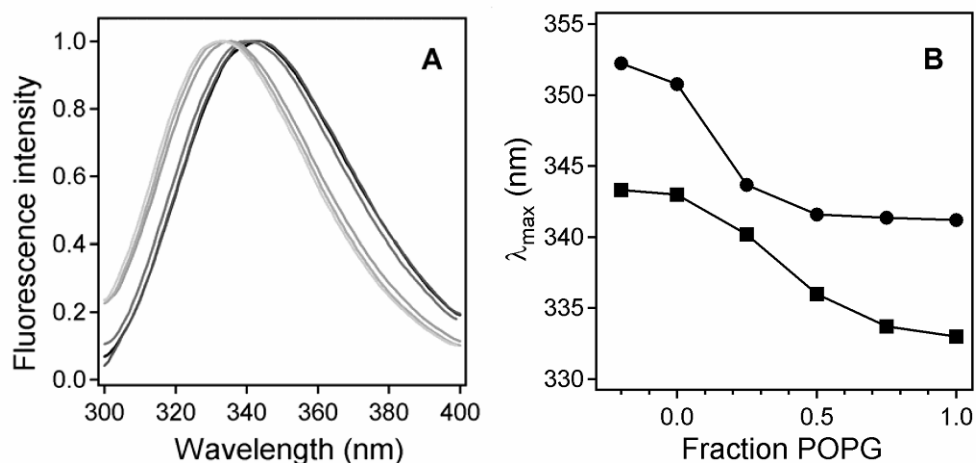
Figure 17 Fluorescence spectra of hIB PLA_2
A: Fluorescence spectra of hIB PLA_2 in the absence (dotted line, which can be hardly discerned because of overlap with the dark solid line) and presence of POPC:POPG lipid vesicles composed of 0.0, 25, 50, 75, and 100 mol% POPG (solid lines changing from dark to light). B: Dependence of the peak wavelength (λ_{max}) of Trp^3 fluorescence spectra of hIB PLA_2 (squares) and the N10-hIB peptide (circles) on the fraction of POPG in membranes. The data points to the left of zero fraction POPG correspond to the Trp^3 emission spectra in the absence of lipid (in solution).

The λ_{max} for the N10-hIB peptide also decreased a total of ~10 nm as the proportion of POPG within the vesicles increased, but unlike hIB PLA$_2$ the λ_{max} of the peptide Trp^3 in solution was higher than the λ_{max} in the presence of vesicles. The peptide also demonstrated a slight shift upon binding to 100% POPC vesicles and reached the maximum blueshift at 50% POPG. The higher λ_{max} for the peptide Trp^3 in the presence (~353 nm) or absence (~343 nm) of vesicles indicates a more polar microenvironment for the identical Trp^3 without the bulk of the enzyme. Stern-Volmer plots were also generated for the full length and N10-hIB peptide Trp^3 acrylamide quenching and K$_{SV}$ obtained (Figure 18).
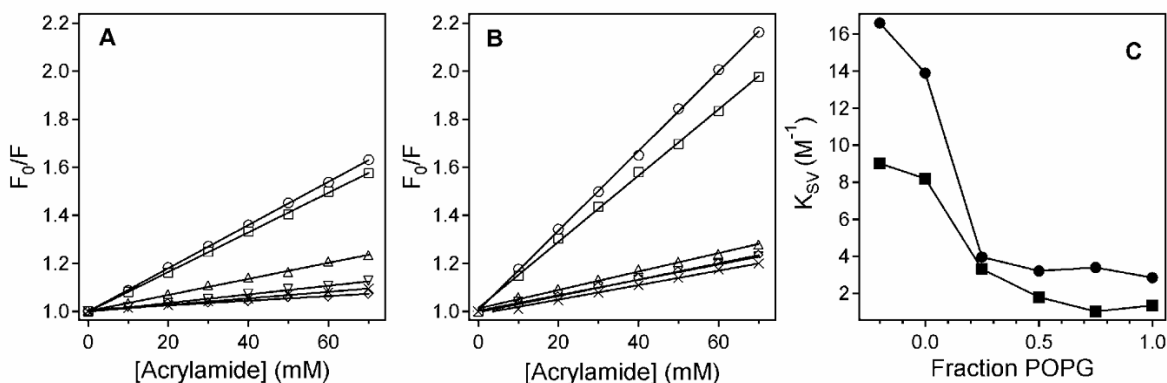
Figure 18 Acrylamide Quenching
Quenching of Trp fluorescence of hIB PLA$_2$ (A) and the N10-hIB peptide (B) by acrylamide in the absence of lipid (circles) or in the presence of 100% POPC (squares), 25% (triangles), 50% (inverse triangles), 75% (rhombs), and 100% POPG (crosses) vesicles. (C) Plots of K$_{SV}$ as a function of the fraction of POPG in POPC/POPG membranes, for hIB PLA$_2$ (squares) and the N10-hIB peptide (circles). The data points to the left of zero fraction POPG correspond to the values obtained in the absence of lipid.

Stern-Volmer constants (K$_{SV}$, an indicator of the efficiency of fluorescence quenching), were obtained from the four Stern-Volmer plots (Appendix A: DQ), and are presented in Table 7. The K$_{SV}$ for the V3W, hIB PLA$_2$ and the N10-hIB peptide Trp^3 free in solution was 12.6, 9.0 and 16.6 M^{-1}, respectively and decreased to 2.2, 1.9 and 3.1 M^{-1} in the presence of vesicles containing 50%

POPG. These results indicate that with increasing membrane anionic surface charge the Trp[3], which is a part of IBS of group IB PLA_2s, becomes less accessible to water-soluble acrylamide. The K_{SV} for the F5W Trp[3] in solution was 3.2 M^{-1}, reflecting the position of the residue within the enzyme, and was reduced to 1.4 M^{-1}, in the presence of 50% PG vesicles indicating an increased shielding effect by the association of the enzyme with the membrane.

Dual quenching experiments in the presence of vesicles containing 50% POPG and either the water-soluble acrylamide (250 mM in the buffer), or the membrane-soluble 10DN (10 mol% in the membranes) were performed (Figure 19). The significant increase in Trp fluorescence intensity in the presence of phospholipid vesicles, accompanied by a blue shift in the fluorescence peak positions of V3W, hIB PLA_2 and N10-hIB peptide is an indicator of efficient membrane binding.

The dual quenching ratios (R_{DQ}), comparing the efficiency of acrylamide quenching to 10DN, were determined (Appendix A: DQ). The R_{DQ} values were 0.78, 0.60 and 0.69 for V3W, hIB PLA_2 and the N10-hIB peptide, respectively (Table 7). These R_{DQ} values reflect a significantly stronger quenching of Trp[3] by the membrane soluble quencher than by acrylamide, indicating an effective insertion of the three different Trp[3] residues into the hydrophobic core of the membrane. Conversely, the R_{DQ} value for the F5W Trp[5] residue was 1.1, reflecting similar quenching by acrylamide than 10DN.

These results demonstrate the intimate contact of the enzyme upon membrane binding resulting from the insertion of Trp[3] into the membrane. We employ another fluorescence quenching method to determine the depth of insertion.
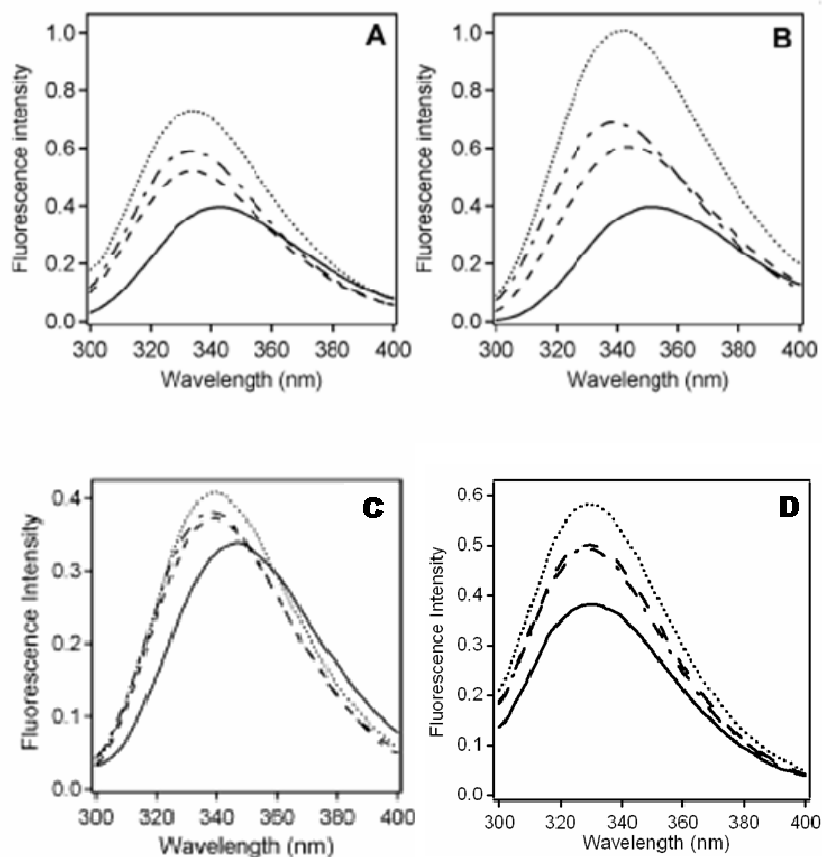
Figure 19 Dual Quenching
(A) hIB PLA2, (B) N10-hIB peptide (C) V3W (D) F5W. Solid lines are free in solution, dotted lines are in the presence of vesicles composed of 50% PG, dashed lines are 50% PG vesicles with 10DN, and dash dot lines are in the presence of 50% PG vesicles and acrylamide.

Table 7 K_{SV} and R_{DQ}

| | | K_{SV} M^{-1} | | | R_{DQ} |
Protein	In solution	POPC	50%PG	POPG	50%PG
hIB PLA$_2$	9.0	8.2	1.9	1.4	.6
N10-IB	16.6	13.9	3.1	2.8	.69
V3W	12.6	-	2.2	-	.78
F5W	3.2	-	1.4	-	1.1

Values of K_{SV} , the measure of acrylamide quenching efficiency and R_{DQ} , the ratio of quenching efficiencies of acrylamide and 10DN on tryptophan fluorescence in solution and in the presence of 100% POPC, 100% POPG and 50% POPG vesicles.

Depth of PLA$_2$ membrane insertion There is emerging evidence that not only the strength of membrane binding, but also the precise mode of membrane binding, including the angular orientation and the depth of insertion, are important determinants of the function of peripheral membrane proteins [81; 82; 99; 100; 101; 102; 103]. On the other hand, partial membrane insertion of PLA$_2$ during interfacial activation is still a matter of debate. We have measured the depth of Trp insertion into LUVs containing 50% anionic lipids for V3W, F5W (Figure 20) and hIB PLA$_2$ (not shown).

Depth was measured as a function of quenching of the intrinsic fluorescence of tryptophan by bromine labeled lipids (Figure 21A), and maximum average depth was determined by distribution analysis (Appendix A: DA). The parameters used to determine the depth of tryptophan are given in Figure 21 B. These results show the V3W Trp^3 inserts into the membrane approximately 9.5 Å from the membrane center, similar to 9.1 Å for the hIB PLA$_2$. The results also show the insertion of the hIIA Trp^5 residue into 50% anionic membrane to a similar depth as the IB.
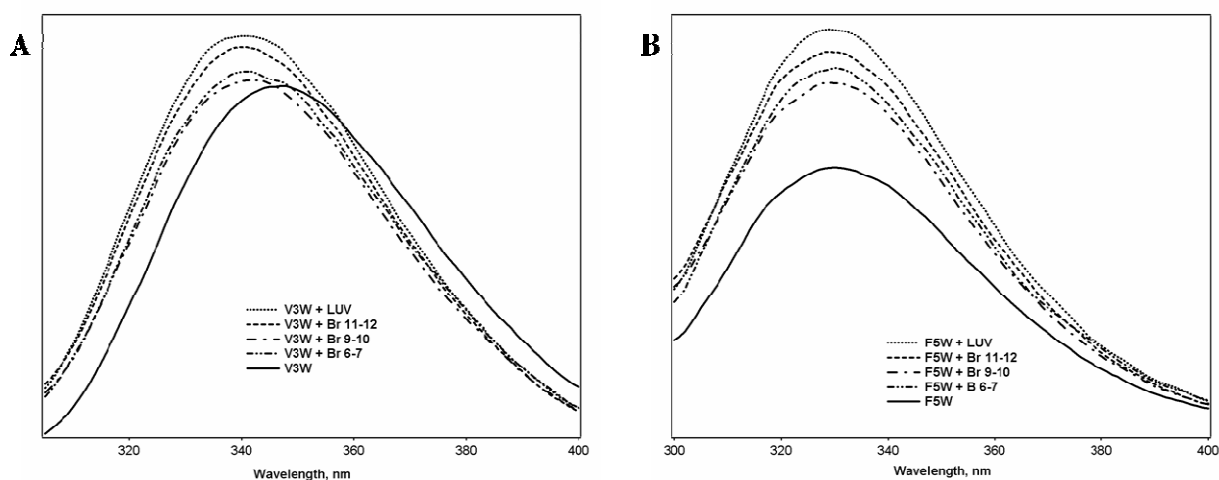
Figure 20 Depth of Tryptophan insertion
A) V3W and B) F5W in solution (solid line) and in the absence (dotted line) and presence of bromine labeled lipids. Br 6-7 dash-dotdot line, Br 9-10 dash-dot line and Br11-12 dashed lines.

6,7-BrPC	9,10-BrPC	11,12-BrPC
11.0 Å	8.3 Å	6.5 Å

1:1 POPC:POPG	h_m (Å)	σ (Å)	S (Å)
V3W PLA$_2$	9.50	1.43	0.52
F5W PLA$_2$	9.1	2.0	0.75
hIBPLA$_2$	9.10	1.70	1.83
bvPLA$_2$	>20	N/A	N/A
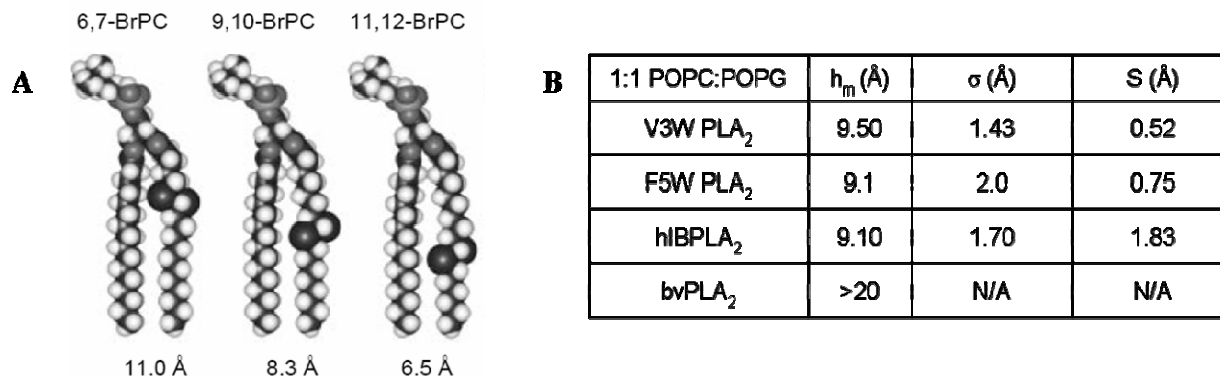
Figure 21 Brominated lipids.
A) Lipids labeled at the 6-7, 9-10 and 11-12 positions with bromine B) DA parameters for V3W, F5W, hIB PLA$_2$, and bee venom (bv PLA$_2$), acting as a negative control; h_m (Å) = mean distance from the membrane center. σ = positional distribution between the fluorophore and quencher, larger values indicate a broader depth distribution, more variation in depth. S = area under distribution curve, it is a function of the efficiency of quenching: a smaller value (less efficiency) indicates a restricted accessibility of the quencher to the fluorophore.

The hIIA PLA$_2$ residues Leu^2, Val^3, His^6, Arg^7 and Lys^{10} have been shown to interact with the membrane. Ile^9 and Phe^5 have both been implicated in substrate binding to the enzyme, inside the binding cleft. Therefore the Trp^5 would have to rotate by at least ~30° in order to interact with the membrane (Figure 7), either by distortion of the first 4 N-terminal residues, or by a twisting and disruption of the entire N-terminal helix, which is unlikely, considering the strength of hydrogen bonding within an alpha helical structure.

However, the mobility of the N-terminal helix *en bloc* has been demonstrated [104]. In the X-ray crystal structures of unbound and substrate-mimic bound hIIA PLA$_2$, the translational movement of the entire N-terminal helix by approximately 1Å is clearly seen. In addition, the results from the acrylamide quenching assay (Figure 16) indicate some accessibility of the Trp^5 to acrylamide when the enzyme is in solution. The steric interaction by the larger Trp^5 could possibly repel the N-terminal helix around the helical axis enough to allow the interaction of Trp^5 with the membrane. The presence of a glycine at position 14 (proline in IB enzymes), would

allow this type of rotation (see Figure 3). The conformational disturbance of the alpha helical structure would then be minimized by the orientation of the entire helix toward the membrane.

This work provides evidence that structurally similar group hIB and hIIA PLA$_2$s, significantly penetrate into membranes.

PLA$_2$ Conformational changes upon membrane binding: CD In order to evaluate the secondary structure of the PLA$_2$ enzymes, far-UV CD spectra of were measured and compared. Circular dichroism allows the qualitative evaluation of secondary structures of molecules. Alpha helix, beta sheet, beta turn, and unordered structures have well defined CD 'fingerprints' (Figure 22).
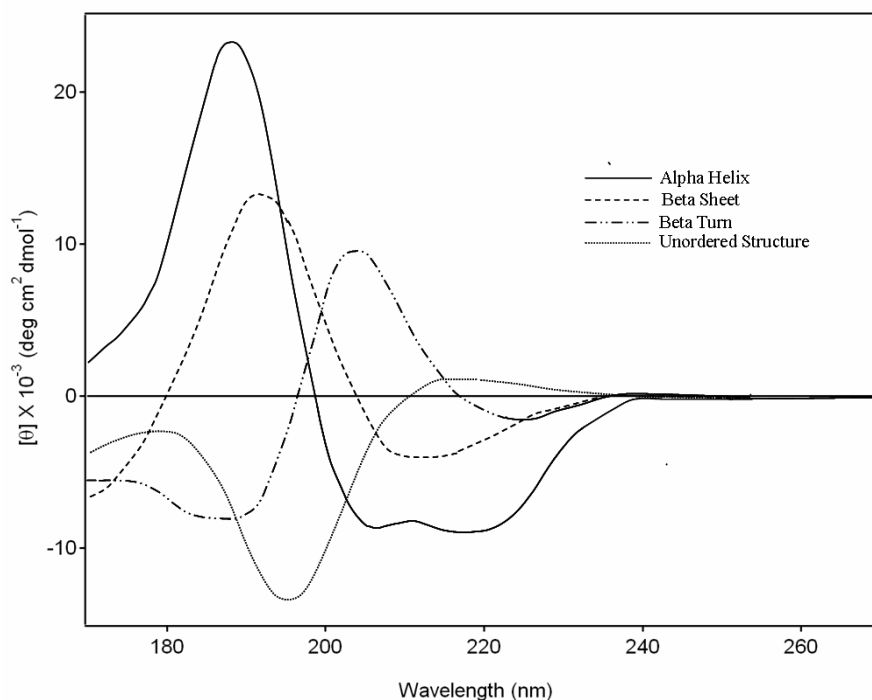
Figure 22 Characteristic CD Spectra
Alpha helix (solid), Beta sheet (dashed), Beta turn (dash dot dot) and unordered structures (dotted line).

The CD spectra for the hIIA PLA$_2$ proteins (Figure 23) exhibit a classical alpha helical profile, with two minima at ~208 and ~222 nm, and a single maximum at ~192 nm. The general similarities of the V3W and F5W to the hIIA PLA$_2$ spectra indicate that neither mutation significantly perturbed the secondary structure of the protein. Similar results were reported by Baker et al., 1998 [73] for the V3W mutation.
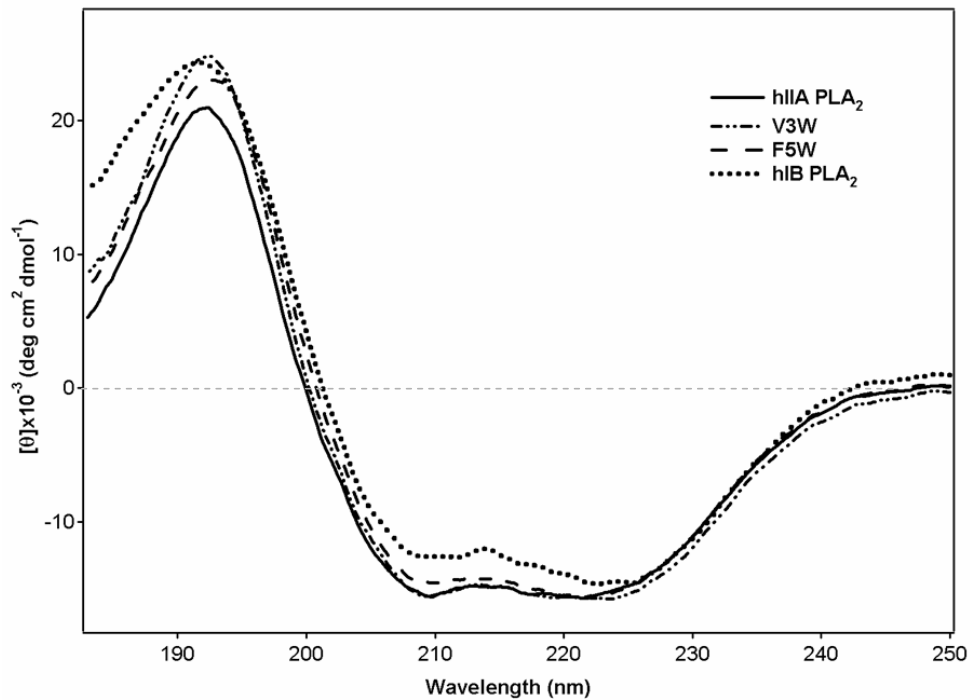
Figure 23 CD spectra of hIIA PLA$_2$, V3W, F5W, and hIB PLA$_2$.
Spectra were recorded in 10 mM phosphate buffer, pH 7.4, at a final protein concentration of 5 mg/mL in a 0.2 cm pathlength cuvette.

It is possible, in light of the above results, that the substitution of a bulkier, more polar Trp on the hydrophobic face of the amphipathic N-terminal helix, which forms one wall of the substrate binding pocket, has perturbed the helical structure of F5W. The slightly higher ellipticity ratio would then be due to the perturbation of a standard a helix conformation. hIB PLA$_2$ also demonstrates a greater shift in ellipticity ratio ($[\theta]_{222}$/ $[\theta]_{208}$) of 1.1, probably due to a difference in the overall content of alpha helices between the IIA PLA$_2$ and IB PLA$_2$ isoforms. Structural analysis from NMR experiments on porcine group IB PLA$_2$ show the first three residues of the N-terminal helix are disordered in solution [105], but upon binding to substrate micelles, the three N-terminal residues conform to a rigid α-helix [80]. Since porcine IB PLA$_2$ free in solution has a less

58

ordered N-terminal helix than the snake venom IIA PLA$_2$ [68], hIB PLA$_2$ may be expected to have a higher value of the $[\theta]_{222}/[\theta]_{208}$ ratio than hIIA PLA$_2$, as detected.

The CD spectra for hIB PLA$_2$ and its IBΔN10 fragment are shown in Figure 24. The two proteins also exhibited an alpha helical profile with a double minima around 223 and 209 nm in the spectra of hIB PLA$_2$ and the hIBΔN10 fragment. The helicity of the full-length hIB PLA$_2$ slightly decreased whereas that of the hIBΔN10 fragment increased in the presence of phospholipid vesicles, the former of which is consistent with NMR data on porcine IB PLA$_2$ in the absence and presence of phospholipid micelles [69; 80; 106]. The CD spectra of the full-length hIB PLA$_2$ and the hIBΔN10 fragment exhibited significantly different line-shapes.
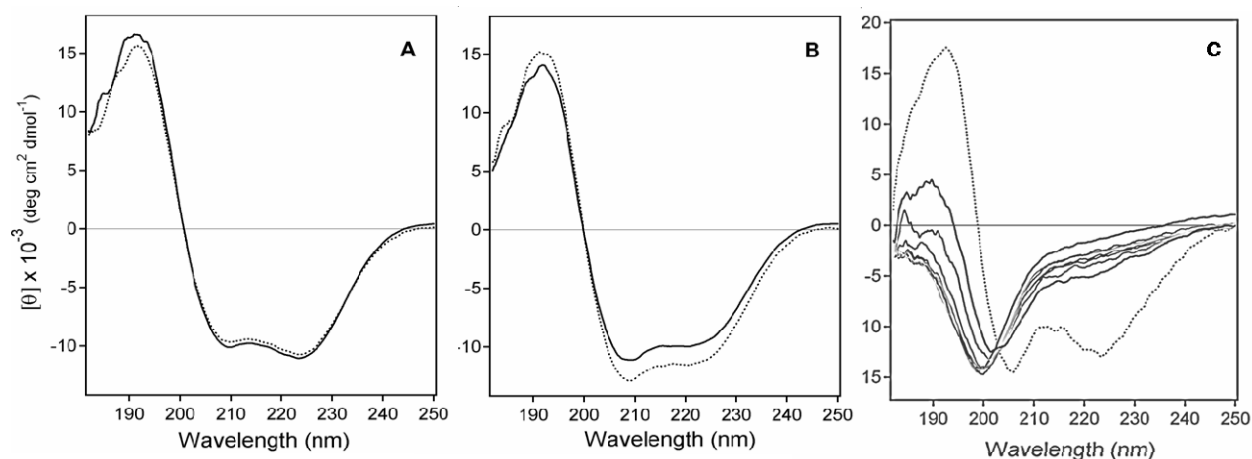
Figure 24 hIB PLA$_2$ CD spectra
CD spectra of A) hIB PLA$_2$ with and without lipid B) its hIBΔN10 fragment with and without lipid and C) the N10-hIB peptide in the presence of increasing concentrations of lipid. For A and B: the solid lines are protein in buffer and the dotted lines are in the presence of nonhydrolyzable ether lipid vesicles di-O-tetradecyl-phosphatidylcholine/di-O-tetradecyl-phosphatidylglycerol at 1:1 molar ratio (1 mM total lipid) 10 μM final protein concentration. C: Lightest curve is the peptide in buffer, Spectra of the N10-hIB peptide in presence of 50% TFE (vol:vol) is shown as a dotted line.

The ellipticity ratio was 1.1 for the full-length hIB PLA$_2$ and 0.87 for the hIBΔN10 fragment free in solution. The ellipticity ratio $[\theta]_{223}/[\theta]_{209}$ is known to increase with increasing flexibility of the helices [107; 108]. Therefore, the difference between the profiles of the CD spectra of

the full-length hIB PLA$_2$ and the hIBΔN10 fragment may indicate increased flexibility of the full-length hIB PLA$_2$ compared to the hIBΔN10 fragment. A decreased flexibility of hIB PLA$_2$ upon removal of the N-terminal 10 residues would predict that the separated N-terminus of the protein in aqueous buffer is likely to be flexible. Indeed, the spectrum of the synthetic N10-hIB peptide in aqueous buffer was characterized by a single minimum around 200 nm, (Figure 24 C) indicating unordered structure for the N10-hIB peptide [109; 110; 111; 112]. The presence of negatively charged lipid vesicles induced increasing fractions of α-helix in the peptide, which probably results from the stabilization of the α-helical conformation by electrostatic interactions between the cationic residues at one face of this amphipathic helix and the acidic lipids. NMR and X-ray studies have shown that the α-helical structure of the N-terminus of porcine pancreatic PLA$_2$ is additionally stabilized by hydrophobic interactions between the nonpolar face of the helix and bound inhibitor or substrate molecules [69; 76; 106].

The CD spectrum of the hIIA/IB PLA$_2$ chimera demonstrated the characteristic alpha helical double minima around 208 and 222 nm, with an absolute value of the mean-residue molar ellipticity at 222 nm ($[\theta]_{222}$) comparable to those measured for group IB and IIA PLA$_2$s (Figure 25). This indicates that the chimeric protein is folded into a structure that comprises ~40% α-helix, which is characteristic of group I/II PLA$_2$s [113; 114]. The shape of the CD spectrum of the chimeric protein was different from those of the group IB and IIA PLA$_2$s, however. The CD spectrum of the IIA/IB PLA$_2$ chimera exhibited an decreased ellipticity ratio $[\theta]_{222}/[\theta]_{208}$ as compared to both hIB PLA$_2$ and hIIA PLA$_2$. Reduced values of the ellipticity ratio $[\theta]_{208}/[\theta]_{222}$ are associated with deviations of the α-helix structure from a standard, rigid helix geometry, e.g. by formation of coiled-coil structures [107; 108] or distorted helices [115]. Although the two internal α-helices of group I/II PLA$_2$s (H2, H3) are nearly antiparallel and disulfide-bonded, they are not

likely to form a coiled-coil structure. The observed feature is therefore more likely to indicate a less flexible conformation of the chimeric hIIA/IB PLA$_2$ compared to the hIB or hIIA PLA$_2$ proteins.

Though no major perturbations in structure are seen with these results, the proposed qualitative differences can be more closely examined by FTIR spectroscopy.
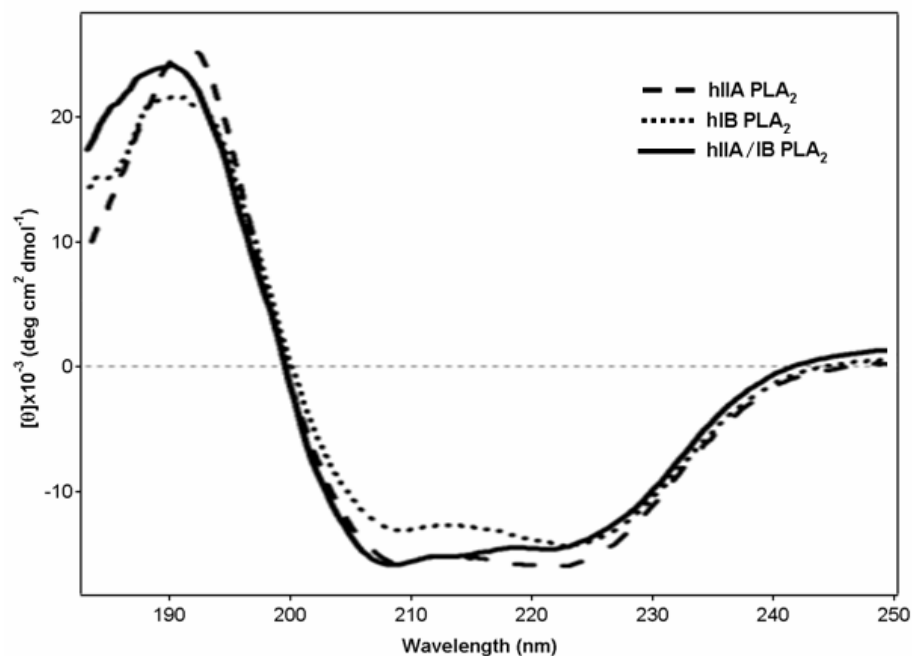
Figure 25 CD of hIIA/IB chimera
CD spectra comparing the chimeric hIIA/IB PLA$_2$ to the parent enzymes. hIIA PLA$_2$ (dashed line), hIB PLA$_2$ (dotted line) and hIIA/IB PLA$_2$ chimera (solid line).

PLA$_2$ Conformational changes upon membrane binding: FTIR The quality and quantity of a protein's secondary structure can be extrapolated from careful evaluation of the amide I absorbance spectra obtained from Fourier transform infrared (FTIR) spectroscopy. The protein backbone atoms that constitute a peptide unit are involved in various complex vibrational modes known as amide modes. Of special interest are the amide I mode and amide II modes 1600-1700 cm^{-1} and 1560-1545 cm^{-1}, respectively (Figure 26).
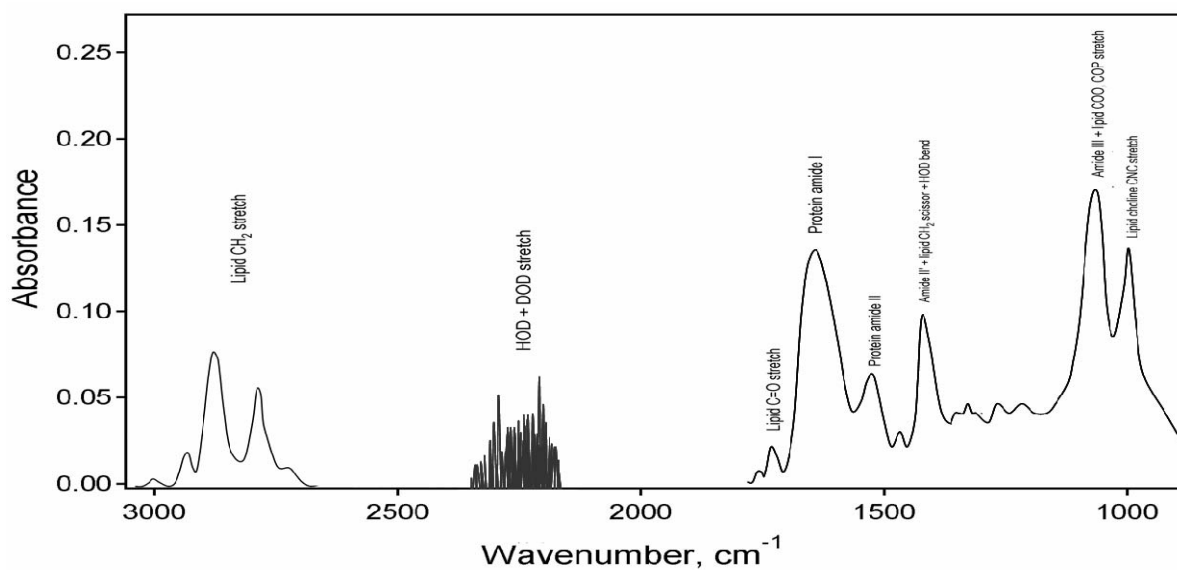
Figure 26 ATR-FTIR absorbance bands
Representative spectrum of a membrane bound protein, the lipid methelene stretch is seen at ~2800-2900, the protein amide I region is between 1700 - 1600 cm^{-1} and the amide II region centers around 1545 cm^{-1}.

By convention, FTIR spectroscopy uses the spatial frequency. i.e., the wavenumber (W) in dimension of cm^{-1}, which is the inverse of the wavelength (λ), W = 1/λ, rather than the temporal frequency (ν) in dimension of s^{-1}. There is a simple relationship between them: $\nu = c/\lambda = cW$, where c is the velocity of light. The amide I mode is mostly comprised of the protein backbone C=O stretching vibration and is very sensitive to the protein secondary structure. The range of amide I absorbance frequencies for secondary structural elements have been well characterized [116] and are presented in Table 8 and Figure 28.

62

Table 8 Amide I peak frequencies

Peak Range	Secondary structure component
1660–1700	γ and β turns
1680–1670	Antiparallel β sheet (high frequency component)
1660–1667	Alpha$_{II}$ helix
1650–1659	Alpha helix
1642–1647	Irregular structures
1636–1630	Antiparallel β sheet (major component)
1625–1615	Intermolecular β sheet
1615–1600	Side chains

Amide I Peak frequency range (in D_2O) and correspondent secondary structure components.
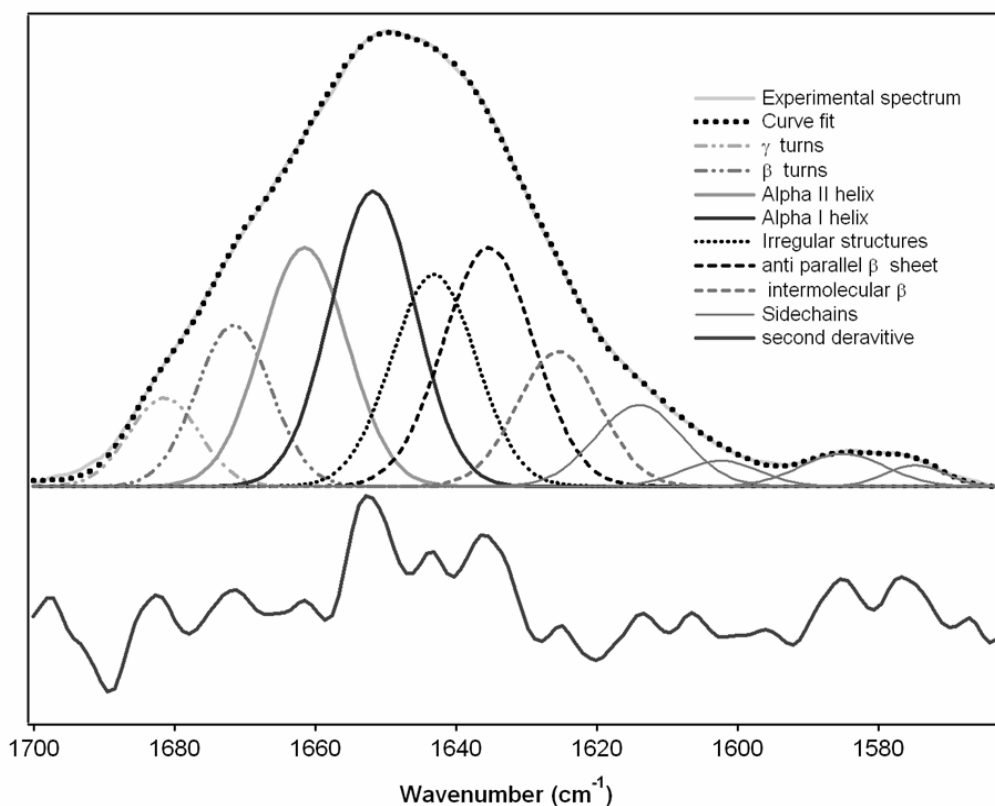
Figure 27 Sample amide I curve fit
Representative amide I peak assignments for secondary structure absorbance bands. The experimental spectrum, (light grey) is deconvolved using the corresponding peaks in the inverted second derivative spectra (solid line bottom). The resultant curve fit, a summation of the individual bands, is superimposed over the experimental curve. The correctness of the fit is demonstrated by the tight correspondence of the two lines.

63

Deuterated water (D_2O) is the solvent typically used in FTIR experiments for protein secondary structure determination, as the H-O-H bending vibrational mode of water absorbs around 1643 cm^{-1} and can eclipse the Amide I spectra, which can confound the deconvolution of the Amide I peak unless very high protein concentrations are used. The larger mass of deuterium in D_2O shifts the bending vibration of the D_2O to a lower frequency, resulting in a solvent-unimpeded Amide I spectra. The amide II mode involves a large contribution from the N-H bending mode and is sensitive to amide hydrogen-deuterium exchange as solvent exposed N-H groups exchange quickly with the D_2O to become N-D (see below, results of HDX kinetics).

ATR-FTIR spectroscopy is uniquely suited for evaluating membrane associated proteins within the unique environment of the membrane-water interface. Unlike the higher resolution techniques of NMR and X-ray crystallography, the qualitative and quantitative structure of the protein in the context of membrane (binding or insertion) can be obtained. The presence of the supported bilayer not only provides the appropriate physiological condition, the nature of ATR-FTIR enables the visualization of only those molecules directly associated with the membrane. Any unbound molecules in the solvent are not within the detection limits of the system, therefore any ambiguity that may arise from a heterogenous population are eliminated.

The Curve fitting results for hIIA PLA_2, V3W and F5W proteins, free in solution and bound to 30:70 POPG:POPC (30% PG) supported bilayers, are presented in Figure 28, the frequencies of the secondary structure components are presented in Table 9, and the proportions of alpha, beta and unordered structures are presented in Table 10.
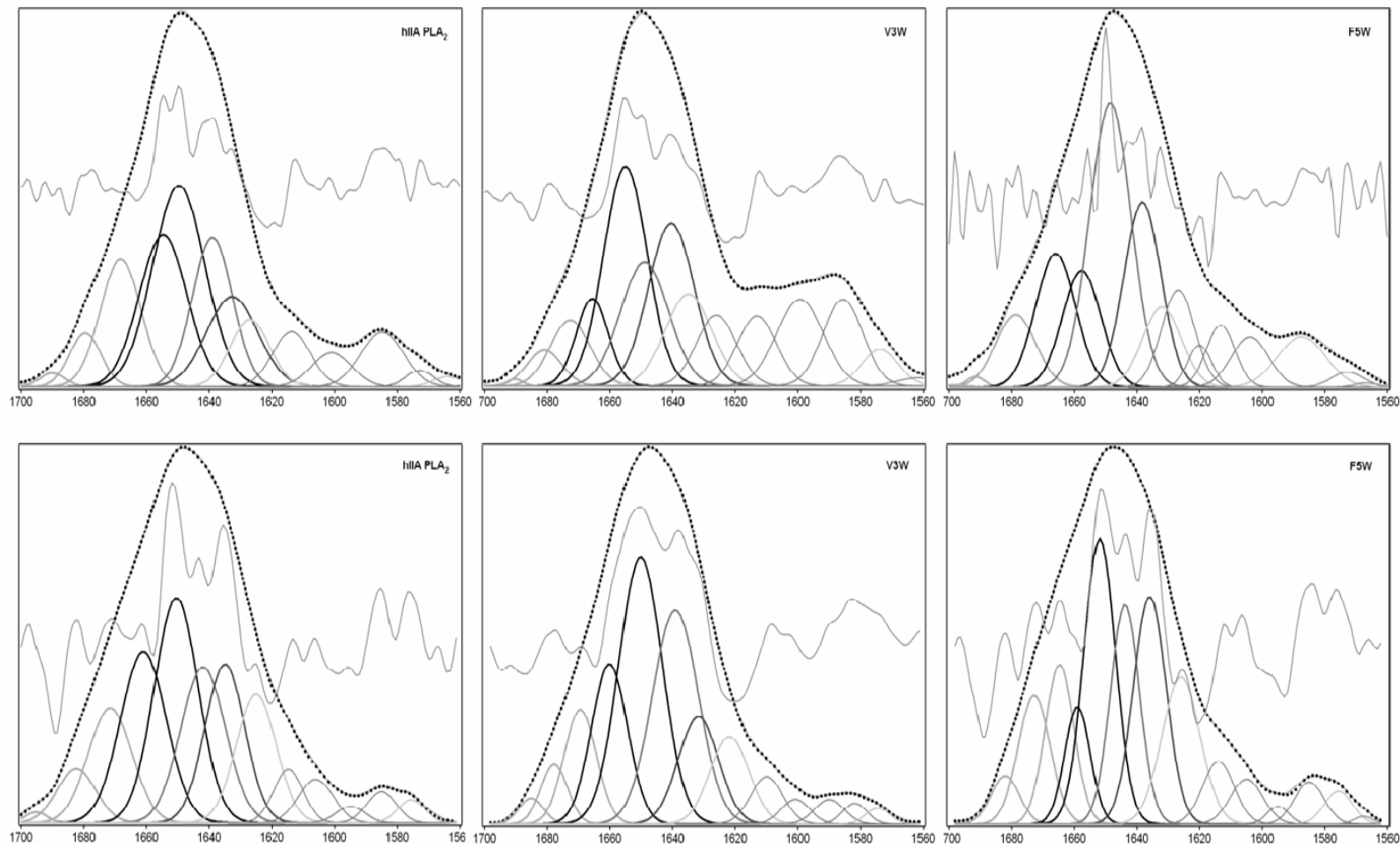
Figure 28 Peak deconvolution

Secondary structure peak fitting of the amide I band for hIIA PLA$_2$ (left), V3W (center) and F5W (right), free in solution (top) and membrane bound (bottom). The alpha helical peaks are centered around 1650 – 1660 cm^{-1} and the peaks representing beta structures are centered around 1635 cm^{-1}. The second derivative spectra, from which the peak center frequencies were obtained is superimposed across the center of the spectra. The splitting of the individual bands can be clearly seen in the second derivative spectra of the proteins that are free in solution (top row).

65

Table 9 hIIA PLA$_2$ FTIR curve fitting results

	hIIA PLA$_2$				V3W				F5W			
	Free in solution		Membrane bound		Free in solution		Membrane bound		Free in solution		Membrane bound	
	ν, cm^{-1}	%	ν, cm^{-1}	%	ν, cm^{-1}	%	ν, cm^{-1}	%	ν, cm^{-1}	%	ν, cm^{-1}	%
	1690.5	0.7	1695.3	0.6	1691.4	0.6	1684.7	1.7	1691.5	1.1	1681.8	2.8
	1679.9	4.2	1682.7	4.7	1680.8	3.4	1677.9	3.7	1678.9	7.5	1673.1	10.4
	1669.3	13.4	1671.2	11.5	1673.1	14.1	1669.3	9.1	1666.4	14.2	1664.4	11.3
Alpha helix →	1654.8	19.0	1660.6	18.1	1654.8	26.1	1660.6	14.0	1657.7	11.6	1658.6	7.4
Alpha helix →	1649.9	28.2	1650.9	22.8	1649.0	15.8	1649.9	28.5	1648.1	30.9	1651.9	20.7
	1639.4	15.5	1642.3	16.1	1640.3	20.3	1639.4	23.9	1638.4	18.0	1644.2	15.8
Beta sheet →	1632.6	11.9	1634.5	14.3	1634.5	11.8	1631.6	10.7	1631.7	8.2	1635.5	18.0
	1626.8	7.1	1624.9	11.9	1625.9	7.9	1622.0	8 .4	1626.9	8.5	1625.8	13.6

Amide I component peak frequencies (ν, cm^{-1}) and fraction of amide I band (%) for hIIA PLA$_2$, V3W and F5W in two conditions.

Table 10 Proportions of secondary structures

FREE IN SOLUTION 1 HR POST D$_2$O

Amide I component	hIIA	V3W	F5W
alpha	47	42	43
beta	13	13	9
other	40	45	48

MEMBRANE BOUND 1 HR POST D$_2$O

Amide I component	hIIA	V3W	F5W
alpha	41	43	28 (39.4)
beta	15	11	19
other	44	46	52

Top: free in solution, bottom: membrane bound; hIIA PLA$_2$ (left), V3W (center) and F5W (right). Compositions for the structural elements correlate with previous values obtained using higher resolution methods for determining tertiary structure showing ~40% alpha helix, ~10% beta sheet and ~50% unordered structure, turns and loops.

The data indicate two components in the alpha helical region for all three proteins free in solution, located at 1655-1658 cm^{-1} and 1650-1648 cm^{-1}, which can be ascribed to unexchanged and deuterated alpha helices, respectively. This assignment results in 41- 47% alpha helix for hIIA PLA$_2$ and V3W, in agreement with high resolution structures of group IIA PLA$_2$s [104; 117]. The data do not indicate major conformational changes caused by the Trp[3] substitution, which agrees with the CD data (Figure 23). For membrane bound hIIA PLA$_2$ and V3W, the higher frequency alpha helical component shifts to ~1661 cm^{-1}, while the other component undergoes little spectral shift. This may reflect structural destabilization of a fraction of alpha helices during membrane binding, resulting in weaker helical hydrogen bonding, stronger backbone carbonyl

bonds, and increased amide I frequencies, as detected earlier for a snake venom group IIA PLA$_2$ [118; 119]. In the case of hIIA PLA$_2$, the alpha helical content appears to decrease slightly upon membrane binding, consistent with weaker helices in the membrane bound state, while no such changes are observed for V3W.

Curve fitting of the amide I bands of the F5W yielded qualitatively different results. For both free in solution and membrane-bound F5W, two components were found in the conventional alpha helical region, one around 1658 cm^{-1}, and the other in the 1652-1648 cm^{-1} region, which are likely to represent the alpha helices with unexchanged and deuterated backbone amide groups. For F5W free in solution, these components constitute 42.5% of the amide I band, which is similar to the helical content for the free in solution hIIA PLA$_2$ and V3W, implying that neither Trp^3 nor Trp^5 substitutions cause significant changes in the protein backbone structure. However, for the membrane-bound F5W mutant these two alpha helical components constitute only 28% of the amide I band intensity, ~14% less than in the protein free in solution. Interestingly, the fraction of components in the 1636-1626 cm^{-1} concomitantly increases by 15% upon membrane binding of the F5W mutant (Table 9). One presumptive interpretation of this result might be a conversion of ~18-19 residues of the protein (15% of 124 residues) from alpha helical conformation to beta structure. However, given the robust three dimensional structure of secretory PLA$_2$s stabilized by multiple disulfides, this is very unlikely to occur. Again, in light of the depth dependent quenching assay, a reasonable interpretation of the amide I curve-fitting results is: upon membrane binding the Trp^5 inserts into the membrane and the interaction with the other two helices is destabilized. The amide I component of the membrane bound F5W at 1664 cm-1 may then be attributed to an α_{II}-type flexible helical structure [120] that absorbs in this infrared region [121; 122; 123]. In this case, the total helical content of

the membrane-bound F5W mutant, found in three alpha helical components, would constitute 39.4%, only 3% (~4 residues) less than the helical structure in the free protein. Combined with the depth dependent quenching and CD results, it would seem that the Trp^5 of the F5W, located on the hydrophobic substrate binding face of the N-terminal helix, interacts with the membrane and thereby causes a structural distortion of the N-terminal helix of the protein upon membrane binding.

In light of these results, the decreased activity of F5W may be determined not by blockage of the substrate entrance into the active site slot, but by a distorted N-terminal helix, which is known to be an indispensable part for PLA_2 activity [83]. The fact that the activity of F5W against zwitterionic phospholipid micelles or vesicles is almost completely lost, but significant activity against anionic membranes is retained, probably results from different modes of binding of the protein to curved interfaces. On micelles, interactions of Trp^5 with the surface is likely to predominate in affecting the mode of binding, while on LUVs, the electrostatic interactions between the cationic residues surrounding the IBS and the anionic membrane predominate, causing the enzyme to adopt a more appropriate mode of membrane binding and enabling access of the substrate to the catalytic site.

PLA$_2$ Conformational changes upon membrane binding: HDX One of the most powerful methods of probing protein dynamic structure is based on the analysis of amide hydrogen-deuterium exchange (HDX) kinetics, which can be measured by FTIR spectroscopy [116; 124]. The amide II band (Figure 26), which involves a major contribution from the amide N-H in-plane bending mode, shifts from ~1545 to 1450 cm^{-1} upon amide deuteration, resulting in a time dependent decrease in the intensity of the band around 1545 cm^{-1}. Each peptide unit in the protein has a unique amide exchange rate, a function of solvent exposure, intramolecular H-bonding, local sequence and microenvironment. Ideally the HDX of a protein of n_{res} amino acid residues should be described using n_{res} -1 rate constants. Although the multiexponential decay of the amide II intensity could be described by a large number of decay (rate) constants, this would not be a feasible approach, as the reliability of their values strongly decreases with increasing numbers of fitting parameters. Alternately, fitting the HDX kinetics with only three populations of amino acid residues: exchange resistant, slow exchanging, and fast exchanging populations, has been shown to be a reasonable approach, in most cases the fractions and rate constants of these populations can be determined reliably [116; 124].

The kinetics of HDX was determined based on the time-dependent decrease in the amide II band intensity around 1545 cm^{-1} (Appendix A: HDX). We have used this approach to characterize the membrane binding induced changes in the dynamic structure of the three hIIA PLA$_2$ proteins, presented in Figure 29. The numerical parameters for the three populations are summarized in Table 11.

The data clearly indicate an increase in the HDX efficiency of all three molecules upon membrane binding, resulting in a 5-10% decrease in the fraction of exchange resistant residues (a$_0$). However, the dynamic conformational changes of F5W are different from hIIA PLA$_2$ and

70

V3W. For the latter two proteins, membrane binding results in an increase in slow exchanging residues (a_1), and a decrease in fast exchanging residues (a_2), with an increase in the rate constants of both slow (k_1) and fast exchanging residues (k_2). The decrease in a_0 and an overall increase in rate constants of HDX can be interpreted in a straightforward manner, in terms of an increased motional flexibility of a proportion of alpha helices in the membrane-bound hIIA PLA_2 and V3W, consistent with the conclusion derived from the amide I curve-fitting data (Table 9).
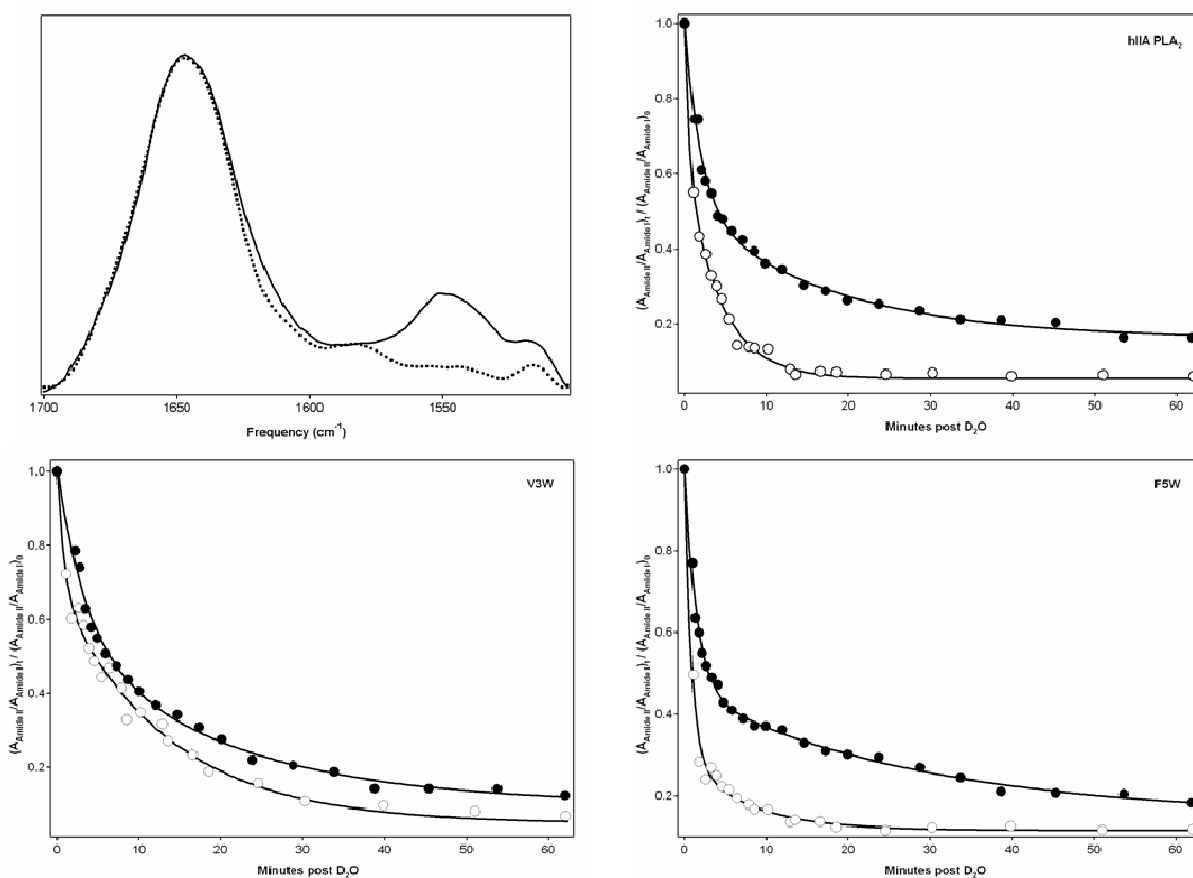
Figure 29 hIIA PLA_2 Hydrogen Deuterium kinetics
Top: (left) Representative spectra of hIIA PLA_2 in H_2O (solid line) and one hour post deuteration (dotted line) illustrating the change in the amide II intensity upon deuteration; and (right) kinetic curves for hIIA PLA_2; bottom: (left) V3W and (right) F5W. Timepoints for enzyme free in solution are closed circles and for membrane bound are open circles.

Table 11 Hydrogen deuterium exchange kinetics

FREE IN SOLUTION

	hIIA PLA$_2$	# N-H	V3W	# N-H	F5W	# N-H
a_0	0.16	20	0.10	12	0.15	19
a_1	0.35	43	0.46	57	0.30	37
a_2	0.49	61	44.00	55	0.55	68
k_1	0.06		0.05		0.03	
k_2	0.51		0.29		0.68	

MEMBRANE BOUND

	hIIA PLA$_2$	# N-H	V3W	# N-H	F5W	# N-H
a_0	0.06	8	0.05	6	0.11	14
a_1	0.59	73	0.64	79	0.18	22
a_2	0.35	43	0.31	39	0.71	88
k_1	0.24		0.08		0.14	
k_2	2.03		1.20		1.21	

HDX parameters for hIIA PLA$_2$ (left), V3W (center) and F5W (right); free in solution (top) and membrane bound (bottom). a_0 are the exchange resistant; a_1 the slow exchange and a_2 the fast exchange populations of amide hydrogens; k_1 and k_2 are the rate constants (min^{-1}) for a_1 and a_2 respectively.

The increase in the fraction of slow exchanging residues (a_1), which is largely compensated by a decrease in the fraction of fast exchanging residues (a_2), most likely results from the seclusion of residues in the dehydrated protein-membrane interface, effectively shielding them from the solvent (note that the D$_2$O buffer was injected subsequent to protein binding to the supported membrane in an H$_2$O buffer).

The 13-14% decrease in fast exchanging residues (a_2) upon membrane binding translates to ~17 amino acid residues that undergo fast HDX in the free protein, but become less accessible to the solvent upon membrane binding. Using an average accessible surface area of 200 Å^2 for amino acids [98], and assuming that nearly half of this area contributes to the protein surface area,

we obtain ~1700 Å^2 for 17 protected residues on the membrane binding face of PLA$_2$, in good agreement with previous estimates of the total area of IBS [60].

Data of the kinetics of amide HDX clearly show that the dynamic behavior of F5W is different from hIIA PLA$_2$ and V3W. For hIIA PLA$_2$ and V3W, the fraction of fast exchanging residues decreases and that of the slow exchanging residues increases upon membrane binding, whereas membrane binding of F5W results in changes in these populations to an opposite direction. On the other hand, the rate constants (k_1, k_2) of all three proteins increased during binding. The substantial increase in the fraction of the fast exchanging residues (a_2), during membrane binding of the F5W is in sharp contrast to the decrease in the fast exchanging residues (a_2) for the other two proteins. From the absence of dramatic differences in membrane binding constants (K_D) of all three proteins (Table 5), it can be inferred that the conformational destabilization, seen in the above results for membrane-bound F5W (Figure 29 and Table 11), is probably significant enough to substantially increase the number of residues that rapidly undergo HDX, even with the partial protection of IBS residues from the solvent. The loss of activity on micelles and the reduced activity on LUVs by F5W can now be attributed to the distortion caused by the interaction of Trp^5 with the aggregated substrate upon binding. However, we have yet to define the large change in catalytic rate observed with the Trp^3 substitution.

The kinetics of amide HDX of the full-length hIB PLA$_2$ and its hIBΔN10 fragment, free in solution and bound to supported membranes, were also determined (Figure 30). Analysis of the HDX kinetics of the full-length hIB PLA$_2$ free in solution showed that $a_0 \approx 2\%$ of all residues were exchange-resistant, $a_1 = 7\%$ were exchanging with $k_1 \approx 0.07$ min^{-1}, and $a_2 = 91\%$ with $k_2 = 3.3$ min^{-1}. In sharp contrast to the behavior of hIIA PLA$_2$ and its V3W mutant, membrane binding of hIB PLA$_2$ results in a decrease in amide HDX efficiency. The membrane-bound hIB

PLA$_2$ indicated an increase in the fractions of exchange-resistant and slow-exchanging residues to ~7% and 13%, respectively, and a concomitant decrease in the fraction of fast exchanging residues to 80%. There is a marked decrease in the efficiency of the amide HDX of hIB PLA$_2$ upon membrane binding implying either a reduced solvent accessibility to the membrane-bound protein or a stabilization of its secondary structure elements. The HDX data of both free and membrane-bound hIBΔN10 fragment were described by the same set of parameters: the fraction of exchange-resistant residues $a_0 \approx 14\%$, $a_1 = 38\%$ of residues exchange with $k_1 \approx 0.44$ min^{-1} and $a_2 = 48\%$ of residues exchange with $k_2 \approx 0.48$ min^{-1}. Clearly, the hIBΔN10 fragment is more resistant to amide HDX exchange and undergoes little changes in conformational dynamics upon membrane binding compared to the full-length PLA$_2$.
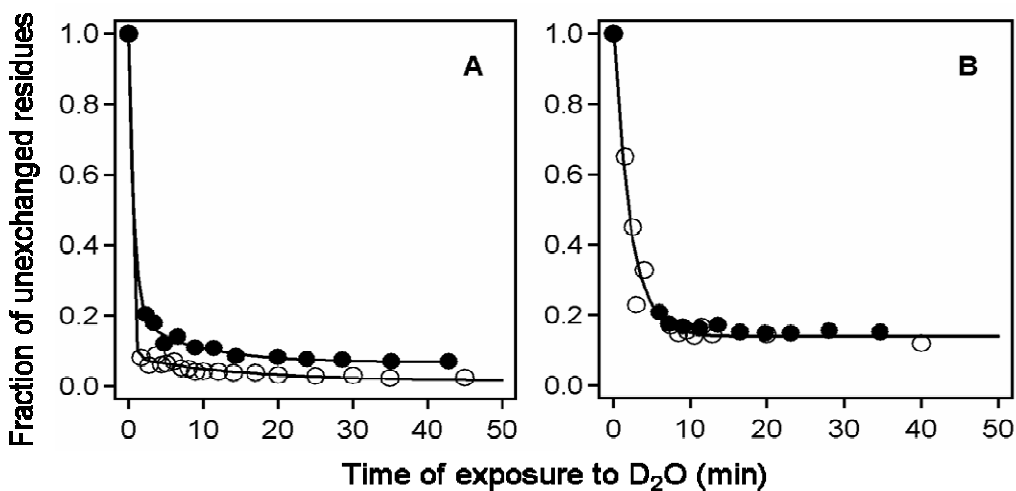
Figure 30 hIB PLA$_2$ HDX kinetics
Kinetics of amide hydrogen/deuterium exchange of the full-length hIB PLA$_2$ (A) and its hIBΔN10 fragment (B) free in buffer (open symbols) and membrane bound (closed symbols).

The major differences seen within the HDX results are between the dynamic nature of the hIIA and hIB PLA$_2$ isoforms. Where the dynamic structure of hIIA PLA$_2$ becomes more flexible upon membrane binding, the dynamic structure of hIB PLA$_2$ is stabilized by membrane binding.

PLA$_2$ Orientation to the membrane surface: R$_{ATR}$ In order to determine if the difference in catalytic activity upon substitution of Val[3] and Phe[5] for Tryptophan in the hIIA PLA$_2$ involves an element of different modes of membrane binding, we have directly assessed the orientations of the three membrane-bound hIIA PLA$_2$ proteins by polarized ATR-FTIR spectroscopy. In polarized ATR-FTIR experiments, bilayer membranes are being prepared at both surfaces of an internal reflection plate, such as germanium, and absorbance spectra are measured at two different plane-polarizations of the incoming infrared light, corresponding to the electric vector of the light parallel and perpendicular to the plane of incidence. The light enters the plate at a set angle (45° in these experiments) and travels inside the plate by means of multiple internal reflections, creating an evanescent field near the plate surface, which exponentially decays in intensity into the supported membrane and the aqueous phase with a decay length of approximately 300 nm. The membrane and the membrane-bound protein molecules absorb a fraction of the energy of the evanescent field, while the molecules far from the membrane do not contribute in the absorbance spectrum. Combination of the internal reflection effect with the aligned sample and polarized light allows one to obtain information of the molecular orientation in the sample due to the difference in absorbance efficiency between the two polarizations of the incident light. The ratio of the absorbance intensities measured at parallel and perpendicular polarizations of the incident light is called its ATR dichroic ratio, R^{ATR}. In order to obtain information on the relative orientation of various secondary structure elements of the proteins, dichroic spectra are generated by dividing the spectrum measured at parallel polarization by the spectrum measured at perpendicular polarization. The values of the dichroic ratios at a particular spectral region can be interpreted in terms of the spatial orientation of the corresponding secondary structure element. Because the alpha helix is the predominant

secondary structure in hIIA PLA$_2$, and is well characterized in terms of polarized ATR-FTIR, we will only consider the R^{ATR} for the alpha helical orientation. The physically meaningful limits of alpha helical R^{ATR} are between 1.3 and 3.6, (three-phase approximation) or between 1.4 and 4.5 (two-phase approximation). See Appendix A: R^{ATR}. The maximum values (3.6 and 4.5) are indicative of alpha helices that are perpendicular to the membrane surface, and the minimum values (1.3 and 1.4) are indicative of alpha helices that are parallel to the membrane surface. For isotropic samples with no defined orientation, the values of the dichroic ratios are R_{iso} = 1.72 or 2.0 for the three- or two-phase approximations, respectively, but these dichroic ratios can also correspond to a specific molecular orientation tilted away from the membrane normal by 54.7°.

Spectra of the three hIIA PLA$_2$ proteins, bound to supported bilayers composed of 70:30 POPC:POPG (30% PG), were measured at parallel and perpendicular polarizations of the incident light. The relative line-shapes of the amide I spectra are similar for hIIA PLA$_2$ and V3W, but are significantly different for the F5W mutant (Figure 31). The R^{ATR} in the alpha helical region for hIIA PLA$_2$ is 1.58-1.65 and 1.60-1.63 for V3W. Because PLA$_2$ consists of three different alpha helices, the dichroic ratio is the averaged ratios for all three, and therefore cannot be interpreted in a straightforward manner. However, a generalization can be made using the R_{iso} values as a reference: because the alpha helical R^{ATR} values for the hIIA PLA$_2$ and V3W are less than R_{iso}, it can be inferred that the helices are oriented more parallel to the planar surface of a 30% anionic bilayer.

As expected, the dichroic spectrum (Figure 31 D) of the F5W mutant strongly deviates from those of hIIA PLA$_2$ and V3W. The F5W alpha helical R^{ATR} is ~1.3, the minimum value for the three phase R^{ATR} approximation, indicating that the general orientation of the three helices of the F5W mutant lie nearly parallel to the membrane surface. The fact that the value of R^{ATR} is

beyond the lower limit set by the two-phase approximation for an alpha helix, reflects the distortion of the helical structure in the F5W during membrane binding. Altogether, these data clearly indicate that while hIIA PLA$_2$ and V3W adopt similar and apparently productive orientations at the membrane surface, the orientation of F5W is significantly different, which is in line with the above findings of substantial deviations of the secondary and dynamic structures of membrane-bound F5W as compared to hIIA PLA$_2$ and V3W.
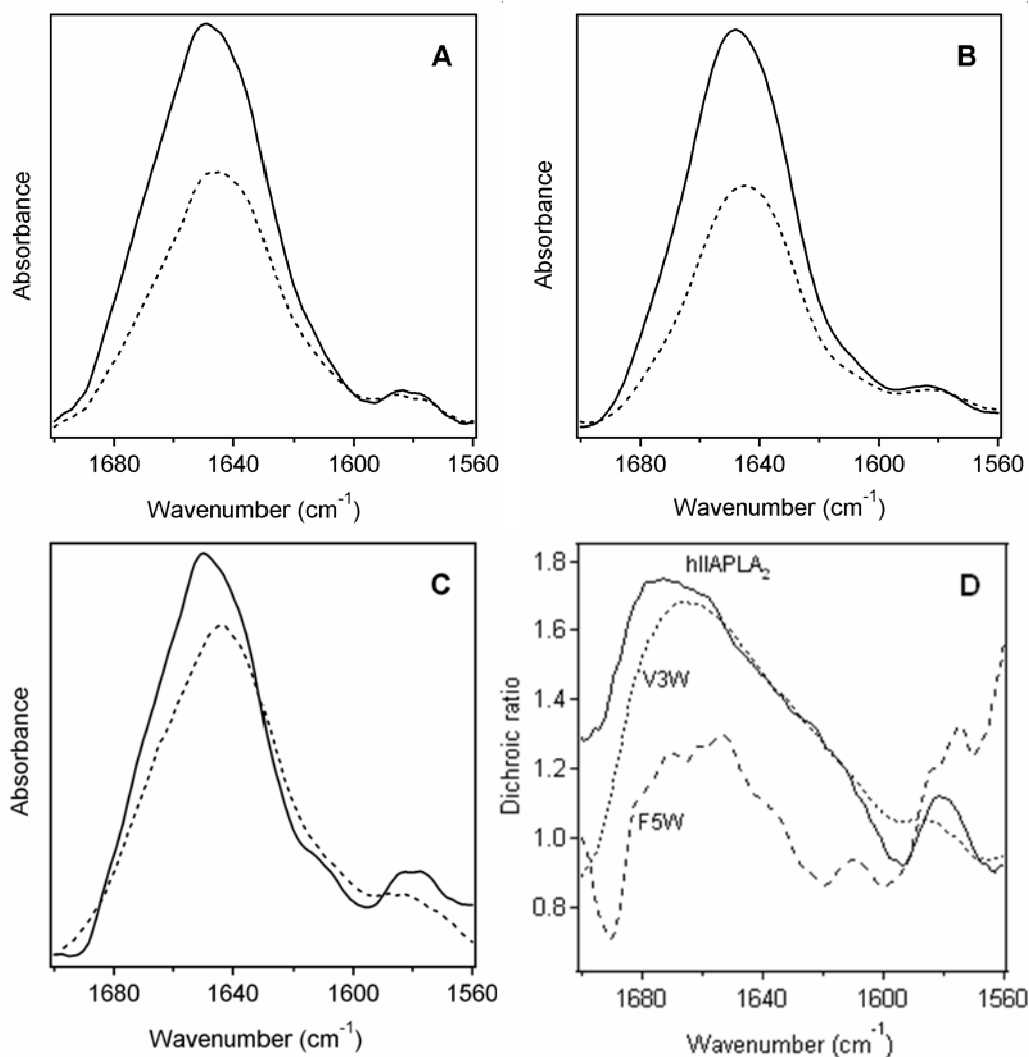
Figure 31 Polarized spectra
Amide I spectra at parallel (solid line) and perpendicular (dotted line) polarizations of the incident light of membrane-bound A) hIIA PLA$_2$, B) V3W and C) F5W; and D) the dichroic spectrum of each, as indicated

PLA$_2$ Orientation to the membrane surface: Algorithm We have determined the precise orientation of the hIB PLA$_2$ enzyme relative to the membrane surface, using a technique that exploits the unique data obtained from polarized FTIR spectroscopy, and depth dependent Trp quenching to use as fitting parameters for a novel analytical geometry algorithm detailed in Appendix B [82; 83]. Curve-fitted ATR-FTIR amide I spectra at parallel and perpendicular polarizations were used to determine the ATR dichroic ratio of the α-helical component of the membrane-bound N10-hIB peptide (R_α^{ATR}) The α-helical ATR dichroic ratio of the peptide was 1.51 ± 0.17. Values of R_α^{ATR} can be used to determine the α-helical order parameters, *S*, (Appendix A: Order parameter). The value of R_α^{ATR} = 1.51 ± 0.17 corresponds to an average order parameter for the membrane-bound N10-hIB peptide of –0.205, varying in the range between –0.033 and –0.405. The order parameter can be interpreted in terms of an average angle (θ) between the helical axis and the membrane normal (perpendicular to the membrane surface, see Appendix A: Figure 40), therefore, we find that the helical axis of the membrane-bound N10-hIB peptide is tilted from the membrane normal by ~64°, and the experimental error in the value of θ is approximately ±10°.

For the full-length hIB PLA$_2$, R_α^{ATR} was 1.36 ± 0.12. In contrast to peptides that comprise a single α-helix, like the N-terminal peptide, the helical dichroic ratio of a protein that has more than one helix cannot be readily interpreted in terms of helical orientation because at a given orientation of the protein with respect to the membrane, different helices may be oriented differently. However, in some specific cases, e.g., for a protein containing two helices, measurements of the helical dichroic ratios of one helix and of the entire molecule, bound to the membrane, can provide the orientations of both helices, which then can be used to position the protein molecule relative to the membrane [116; 125]. These procedures require information on the

number of helices and their relative arrangement within the protein molecule. Since the structure of hIB PLA_2 is not available, we have used the coordinates of the crystal structure of porcine IB PLA_2 (PDB code: 1P2P), which shares 88% sequence identity with its human counterpart. Analysis of the 1P2P structure identified three major (i.e., more than one turn) α-helices, residues 1-9 (H1), 39-55 (H2), and 91-105 (H3). We have used the C_α atom coordinates to determine the interhelical angles (Figure 32), using a newly developed algorithm [82].
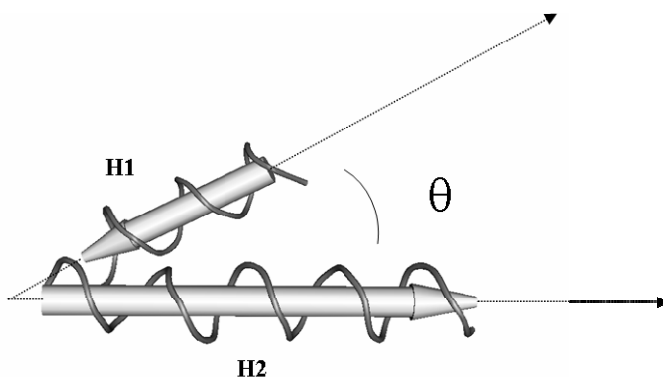
Figure 32 Interhelical angles
The angle between the axis of the N-terminal helix (H1) and helix 2 (H2) θ, is designated η_{12}. The angle between the N-terminal helix and helix 3 (H3) is η_{13}, and the angle between H2 and H3 is η_{23}.

Our calculations yielded the following angles: 37.2° between helices 1 and 2 (η_{12}), 37.7° between helices 1 and 3 η_{13}), and 4.2° between helices 2 and 3 (η_{23}). Here N-C or C-N directions of helices are not taken into consideration because helices at tilt angles θ or $\theta \pm 180°$ yield the same infrared dichroism. This indicates that H2 and H3 are virtually parallel to each other. Therefore, we can ascribe a single orientational order parameter to H2 and H3, which we define S_2. This specific situation allows us to use the α-helical order parameter of the hIB PLA_2 N-terminal α-helix (S_1 = -0.205) and the total α-helical dichroic ratio of the full-length hIB PLA_2 protein ($R_{\alpha T}^{ATR}$ = 1.36 ± 0.12) to determine the order parameter of H2-H3 (S_2) in the membrane-bound hIB PLA_2 molecule [125; 126]. We find then, that the order parameter of H2-H3 of the
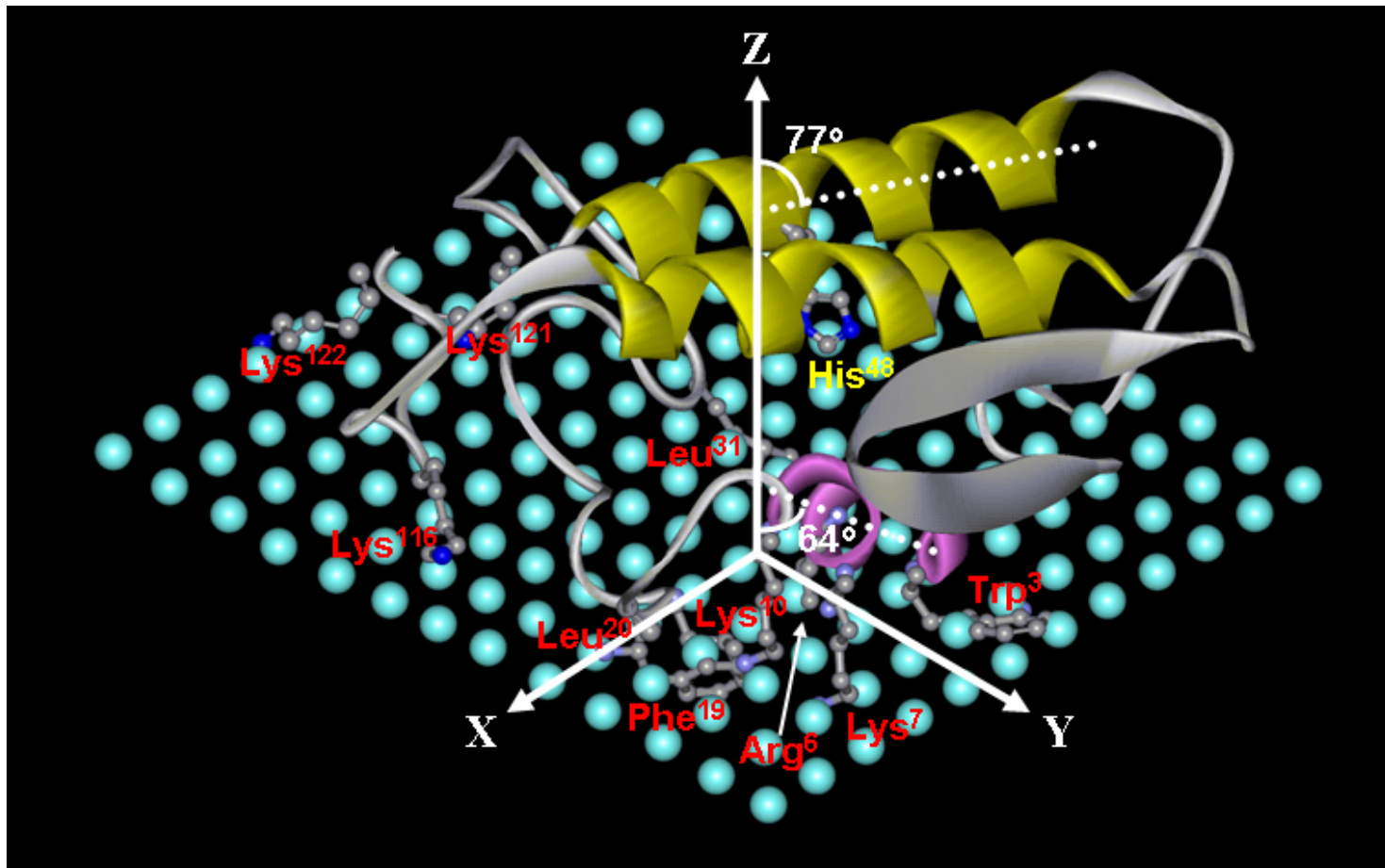
Figure 33 hIB PLA$_2$ quinary structure

A model for membrane binding of human pancreatic PLA$_2$ that emerges from determination of the orientation of the α-helices of the protein relative to the membrane normal. The protein backbone structure is based on the crystal structure of porcine pancreatic PLA$_2$ (PDB code: 1P2P), which shares identical function and 88% sequence identity with the human enzyme. The protein is shown in a ribbon format, with the N-terminal helix colored magenta and the other two helices colored yellow. The key residues of the interfacial binding surface, as well as the catalytic residue His[48], are shown in a ball and stick format. The membrane surface is in the XY plane and is shown by a mesh of sky-blue spheres. Z is the membrane normal. Each phospholipid polar headgroup can be imagined to consist of two spheres, which may represent, e.g., the phosphate and choline moieties of phosphatidylcholine. The angles that the Z axis makes with the N-terminal α-helix and with the other two helices are shown.

full length hIB PLA$_2$ is: S_2 = -0.43 ± 0.2, which indicates that the tilt angle of H2-H3 from the membrane normal is $\theta \approx 77°$ and varies within the range between 66 and 90°. This means that these helices are strongly tilted away from the membrane normal and are nearly parallel to the membrane surface. The knowledge of the orientations of the helices of hIB PLA$_2$ with respect to the membrane normal allowed us to position the protein at the membrane surface with a unique angular orientation, as shown in Figure 33.

Next, we used similar procedures to assess the orientation of the membrane-bound hIBΔN10 fragment. Here the simple one-helix approach is applicable because the two helices in the protein are parallel to each other. The α-helical ATR dichroic ratio of the hIBΔN10 fragment was 1.68 ± 0.13, which corresponds to an average order parameter for H2-H3 in the membrane-bound hIBΔN10 fragment of $S_{\alpha,fr.}$ = -0.033, with variation between -0.162 and +0.084. The variations of the estimated order parameters for all three molecules, i.e. the full-length hIB PLA$_2$, the N10-hIB peptide and the hIBΔN10 fragment, are likely to result from different sources, such as the fluid nature of POPC/POPG membranes, surface roughness of the internal reflection plate, and a certain distribution around an average molecular orientation [127]. In other words, the real fluctuations of the order parameters characterizing the orientations of the molecules relative to the membrane must be smaller than the limits of experimental uncertainties presented above.

The fact that the order parameter of the membrane-bound hIBΔN10 fragment is close to zero (-0.033) is very likely to indicate a random, isotropic orientation of the molecule at the membrane surface. The membrane binding isotherms of the hIBΔN10 fragment, which, unlike those of the full-length hIB PLA$_2$ and the N10-hIB peptide, are nearly linear and do not show a tendency to saturate (Figure 14), are also indicative of nonspecific binding. Taken together, the RET and ATR-FTIR data indicate that while the full-length hIB PLA$_2$ binds to the membrane

surface at a specific orientation, the binding of the hIBΔN10 fragment is weaker and nonspecific. This conclusion is further reinforced by the fact that the N10-hIB peptide itself binds to membranes with high affinity and at a defined orientation. Altogether, these data suggest that the role of the N-terminal α-helix of hIB PLA$_2$ is not only to increase the binding affinity of the enzyme for the membranes, but primarily to properly orient the hIB PLA$_2$ molecule and facilitate its productive mode interaction with the membrane.

PLA$_2$ Orientation to the membrane surface: segmental labeling We have also determined the orientation of a chimeric protein, in which the first 10 N-terminal residues of hIB PLA$_2$ have been substituted for the first 10 N-terminal residues of hIIA PLA$_2$. The experimentally derived membrane orientation of both hIB PLA$_2$ and hIIA/IB chimeric PLA$_2$ creates an unprecedented opportunity to evaluate the contribution of the N-terminal helices in positioning the enzyme relative to its aggregated substrate, providing a unique insight into the subtleties of structure function relationships. As the structure of the human IB PLA$_2$ has yet to be determined, the structure of the porcine IB PLA$_2$, which has a 88% sequence identity to the hIB PLA$_2$, was used as a template to obtain the hypothetical structure of the IIA/IB PLA$_2$ chimera from the internet based server Swiss-Model [128]. The model, as expected, had the same global structure as the IB PLA$_2$ enzyme but the interhelical angles, (Figure 32) for the chimera were slightly different from the IB PLA$_2$. The angles, η_{12}, η_{13}, and η_{23} were 35.5°, 36.6° and 6.2° for the chimera, and 37.2°, 37.7° and 4.2° for the hIB PLA$_2$, which is not surprising, considering the flexibility of the hIIA PLA$_2$ N-terminal helix to shift in or out by 1Å [117].

The other parameters used were the R_α^{ATR} values obtained by polarized FTIR of the hIIA/IB PLA$_2$ chimera and a peptide comprised of the first 10 N-terminal residues of hIIA PLA$_2$ (N10-hIIA peptide) under the same experimental conditions as the hIB PLA$_2$, and the depth of the hIB Trp^3 residue, translated to fit the smaller Val^3 of the IIA N-terminal helix (10 Å from the membrane center). The R_α^{ATR} values for H1 and H2-H3 were 1.45 and 1.35, obtained by differentially labeling the hIBΔN10 fragment before ligating it to the unlabeled N10-hIIA peptide, and yielded the order parameters of $S_{\alpha1}$ = ⁻0.268 and $S_{\alpha2,3}$ = -0.392 which in turn translate to angles of ~67° and 74° from the membrane normal. The complete description of the methods employed and resultant orientation including the positioning of key binding residues for
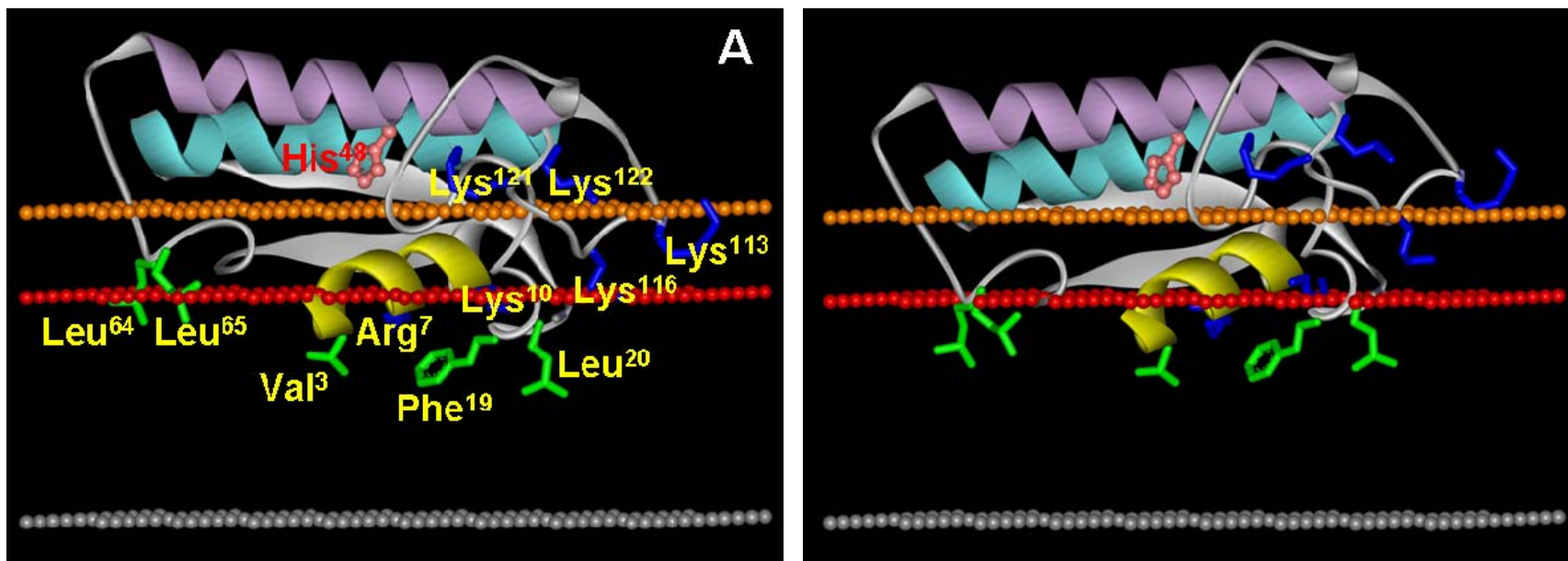
Figure 34 hIIA/IB PLA$_2$ chimera quinary structures

The hIIA/IB PLA$_2$ chimera is presented in a ribbon format, with the α-helices H1, H2, and H3 colored yellow, purple, and light blue, respectively. The side chains of amino acids directly involved in physical interactions with the membrane are shown, hydrophobic residues in green and the cationic residues in blue. The catalytic His[48] is shown (rose). The three layers of non-protein atoms are introduced to schematically show membrane sections corresponding to the acyl chain terminal methyl carbons (gray), the *sn*-1 carbonyl oxygens (red), and the phosphorus atoms (orange) of membrane glycerophospholipids. The *z*-coordinates of these layers are 0, 14.5 Å and 20 Å, respectively. In panel ***B***, the protein has been rotated by 10 degrees about an axis parallel to the X-axis, which results in immersion of Leu[64] and Leu[65] into the hydrophobic part of the membrane.

84

both enzymes can be found in Qin et al., 2004, 2005,[81; 83] and also in Tatulian, 2005[82].

The comparison of the two enzymes demonstrate the precise three dimensional orientation of chimeric IIA/IB PLA$_2$ relative to the surface of the membrane (Figure 34) is different than hIB PLA$_2$ (Figure 33), and that the orientational difference is mediated by the N-terminal alpha helix. The near complete loss of activity for hIBΔN10 fragment, coupled with the 60% reduction in activity for the hIIA/IB PLA$_2$ chimera, demonstrates the functional significance of orientation for these enzymes to facilitate its productive mode interaction with the membrane.

Ultimately, the precise orientation of hIB and hIIA/IB chimeric PLA$_2$ provides evidence that the N-terminal helix of group I/II PLA$_2$s acts as a regulatory domain to mediate and support interfacial activation of these enzymes by enhancing the membrane binding strength, conferring conformational integrity and plasticity to the enzyme, and ultimately facilitating a productive-mode orientation of shPLA$_2$ at the membrane surface.

CHAPTER FOUR: ORIENTATION AND ACTIVATION

Interfacial activation is the term initially used to describe the large rate differences observed between the minimal hydrolysis of soluble monomeric substrate (below the substrate's critical micellar concentration, CMC), and the rapid hydrolysis of aggregated substrate such as micelles or vesicles. The term also includes an apparent induced change in catalytic efficiency of the enzyme at some point after binding, characterized by a lag phase of relatively low catalytic activity followed by a burst of enhanced activity, an 'activation' of the enzyme mediated by interfacial binding. In order to elucidate the activating mechanism, many high resolution structures of these enzymes have been generated, both free in solution and bound to substrate mimics or inhibitors, with and without micelles [66; 68; 80; 104; 117]). Additionally, the kinetics of binding to aggregates has been effectively separated from the kinetics of the catalytic event by careful design of the experimental conditions, allowing independent evaluation of these two steps [60; 129; 130; 131].

Through these foundational experiments, interfacial activation has been solidly correlated to the physical state of the substrate: aggregate curvature and packing order (a determinant of membrane fluidity), and other morphological determinants, including surface charge and topology of the phospholipid head-groups, as well as lateral phase separation, and membrane disruption [89; 90; 102; 132; 133]. The lag phase is most pronounced on zwitterionic substrates, and has been observed to decrease with increasing concentrations of anionic components within the aggregate [55; 57; 118; 134]. However, the anionic activators, such as the phospholipids PG, PA, or PS, or the anionic amphiphile, cholesterol sulphate, vary in their ability to activate different phospholipase A_2 isoforms. For example, PA is an effective activator of group IB PLA_2 enzymes but is ineffective for hIIA PLA_2, and between the anionic equivalent phospholipids PG and PS,

only PG is an effective activator of hIIA PLA$_2$. The burst of activity was correlated to the time dependent buildup of anionic products within the aggregate, implying that the activating mechanism was simply a consequence of an increase in the number of enzymes bound. However, Burack et al., 1995 [92] demonstrated that most of the enzyme is bound to the substrate well before the burst of activity, implying the presence of a relatively inactive state.

Conformational changes within the enzyme were evaluated through atomic resolution methods. Crystal structures of the enzyme alone or bound to an inhibitor or substrate mimic, revealed no structural differences between the two conditions [135]. However these structures do not represent the conformation of the enzyme bound to substrate aggregates, only single substrates within the substrate binding site. A solution structure of the pIB PLA$_2$ isoform, bound to a substrate mimic in the presence of micelles, revealed an ordering of the first three residues of the N-terminal helix upon binding, which directly affected the hydrogen bonding network of the catalytic site, implying possible allosteric effects mediating interfacial activation [80; 106]. However, the solution structures of group IIA PLA$_2$ enzymes, which demonstrate the greatest change in catalytic rates, do not show any differences in the helical quality of N-terminal alpha helix between the bound and unbound states, but did demonstrate a 1Å shift of the whole helix between bound and unbound states [104].

Qualitative methods employed by our lab also revealed possible allosteric mediators, in that upon binding to supported bilayers, the secondary structures of a group IIA PLA$_2$ from the eastern cottonmouth, *Agkstrodon piscivorus piscivorus* (AppD49), were more dynamic than in solution [56; 119]. In this work, the HDX kinetics results from hIIA PLA$_2$ and V3W are in agreement with the AppD49 results, revealing a more dynamic structure upon membrane binding than in solution. However, the inverse was seen for hIB PLA$_2$, where the efficiency of HDX

exchange was reduced upon membrane binding, implying a stabilization of its secondary structure components. Interestingly, the results from the chimeric protein demonstrated a more rigid structure for helices 2 and 3, from hIB PLA$_2$, and a more flexible structure for the N-terminal helix, from hIIA PLA$_2$, than the native hIB PLA$_2$ enzyme.

Site directed mutation or labeling methods have been extensively employed, in order to determine the specific residues involved in binding, and the contribution of those residues to interfacial activation [57; 66; 72; 76; 136; 137]. These studies reveal not only group specific but species specific residues that are involved in substrate recognition, binding, and catalytic activity. These residues are most often lysines or arginines, hence the effects of the concentration of anions in the membrane. However, binding and activation can not be attributed to electrostatics alone, hydrophobic interactions, mediated especially by tryptophan or phenylalanine also play a significant role in the toxicity of the snake venom isoforms [67; 138]. Ultimately, these experiments produced a consensus of key substrate binding residues: hydrophobic residues surrounding the opening to the substrate binding site, key interfacial binding residues on the external face of the N-terminal helix, most notably in positions 2, 3, 7 and 10, with other species specific residues in various positions across the surface and along the edges of the IBS.

From the above results it is evident that interfacial activation is mediated by both enzyme and substrate associated factors. Other experiments reveal a third contributor: solvent interactions. It is understood that the single substrate must move from the confines of the aggregate into the substrate binding pocket of the enzyme. Though not directly addressed in most of the literature, it is implied that this transfer is mediated by diffusion; is considered either part of the catalytic step in the kinetic scheme or precedes the activation step; and is precluded by the enzyme binding to the aggregated substrate. In order for the single substrate to leave the

energetically favorable environment of the aggregate, it must not encounter any barriers to that migration. It is not surprising then, that the dehydration of the substrate interface in direct contact with the enzyme, was observed under kinetic conditions of constant, enhanced activity i.e. on 100% anionic substrate [129]. This observation was inferred from Trp[3] fluorescence quenching experiments on pIB PLA$_2$, similar to the experimental methods employed here which demonstrated an incomplete protection from the aqueous quencher, acrylamide, for V3W, F5W, hIB PLA$_2$, or N10-hIB peptide on 50% anionic lipid, or for hIB PLA$_2$ and N10-hIB peptide on 100% anionic lipids. Berg et al., 2004 [139] suggested that the allosteric activation of PLA$_2$ was a result of the dehydration of the interface upon binding of the enzyme to the aggregated substrate. In fact, ATR-FTIR methods revealed a conformational change of the supported bilayers induced by binding of AppD49, increasing the order parameter of fluid membranes and decreasing the order parameter of gel state membranes [56]. Interestingly, AppD49, upon covalent modification of the catalytic His[48] (an internal residue), demonstrated no such effects upon the membrane; nor did it undergo the dynamic structural changes noted with the unmodified enzyme [56]. These data suggest a dehydration of the membrane by PLA$_2$, with a concomitant formation of hydrogen bonds to the membrane. Although the work of Gadd and Biltonen, 2000, [140] neatly correlated an increase in activity and level of dehydration to the concentration of anionic phospholipids within the membrane, the precise mechanism has yet to be defined.

Because the conservative substitution of a single residue, Val[3] with Trp, resulted in a very large enhancement in the catalytic rate of the human IIA PLA$_2$ isoform, we focused our continued search for the mechanism of interfacial activation on this mutation. We also generated a novel conservative substitution, Phe[5] for Trp, in close proximity to the third position, only on the internal face of the key N-terminal helix. The only difference noted between hIIA PLA$_2$ and

89

V3W, was the level of activity. The rate difference was seen in a system of mixed micelles, on a substrate near the gel to fluid transition state, and in the initial phase of hydrolysis on 15% anionic substrate. There were no notable structural differences either in solution, or bound to 30% anionic supported bilayers, nor were there any differences in the dynamic structures in the same conditions. There weren't any major differences noted on the strength of binding, accessibility to solvent and membrane associated quenchers, or the depth of membrane insertion of the Trp^3 residue (compared to the native Trp^3 from hIB PLA_2).

The clues to the mechanism of interfacial activation were found in the surprising retention of activity of F5W on 15% anionic bilayers, and the reduction in activity of the chimeric enzyme, as well as the almost total loss of activity for the truncated hIBΔN10 fragment. If binding to the aggregated substrate and proximity of the active site to the monomeric substrate were the only two criteria for activity, the hIBΔN10 fragment should have demonstrated a greater level of activity than what was seen. If the presence of the N-terminal helix was crucial to activity, then the chimeric enzyme seemingly should have demonstrated a higher level of activity. The differences revealed in this work are in the results from the ATR-FTIR experiments of F5W upon binding to supported bilayers. Under conditions where the enzyme is presumed to be active, (F5W demonstrated activity on 15% anionic bilayers), there was a noticeable disruption in the dynamics and quality of the secondary structure, which was also associated with a change in orientation of the enzyme to the substrate,

While many groups have alluded to the orientation of the enzyme to its substrate as a possible factor in the mechanism of interfacial activation, only a few have postulated an orientation of the enzyme to its substrate [74; 94]. This was done by interpreting results from indirect methods, i.e. mutation of IBS residues and spin labeling experiments. We have oriented

the enzyme by applying the direct measurements of the enzyme's angular orientation, while bound to supported membranes, to a novel algorithm that exploits the intrinsic geometric nature of helices, translation dipole moments and electromagnetic vectors. The output of the algorithm is the translation of the established atomic coordinates of the enzyme to the coordinate system of the supported bilayer, specifically orienting the enzyme on its substrate.

It is evident that each homologous phospholipase A2 isoform has unique, group specific and also species specific residues that determine the isoform's functional specificity. One prime example is the distribution of positive charges over the entire surface of the human group IIA PLA$_2$ facilitating the enzyme's specific targeting of bacterial membranes, while effectively ignoring the PC rich plasma membranes of self cells. This residue mediated specificity can be viewed as an orchestrated combination of noncovalent bonding: hydrogen, ionic, hydrophobic and van der Waals interactions, which determine not only selectivity and affinity of the enzyme for the substrate aggregates, but also the orientation of the enzyme to the surface.

The conclusion most evident in the reconciliation of this work with the existing body of knowledge is that, the phenomenon of interfacial activation is mediated by simply optimizing the orientation of the enzyme to the interface. The accumulation of anionic product promotes a stronger interaction between the enzyme and aggregated substrate. This induces a dynamic conformational shift in the enzyme, accompanied by a topographical remodeling of the aggregate, resulting in a productive orientation of the enzyme to the interface. The tight binding induces a dehydration of the interface, allowing the monomeric substrate to enter the enzyme. It may seem that this is simply a statement of the obvious. It is. The mechanism for interfacial activation is revealed by a careful scrutiny of the obvious.

In order to definitively describe the mechanism of interfacial activation, the kinetic scheme proposed by Berg et al., 2001 [60] (Figure 6) must be rearranged, redefined and expanded to include the two binding states of the enzyme, the transfer of monomeric substrate to the enzyme, and the movement of the enzyme along the interface (Figure 35).

$$E+S \xrightarrow{K_D} E \cdot S \xrightarrow{K^\#} E^* + s \xrightarrow{K_1} E^* \cdot s \xrightarrow{K_{s^*}} E^* s \xrightarrow{K_{cat}} E^* P \xrightarrow{K_2} E^*$$
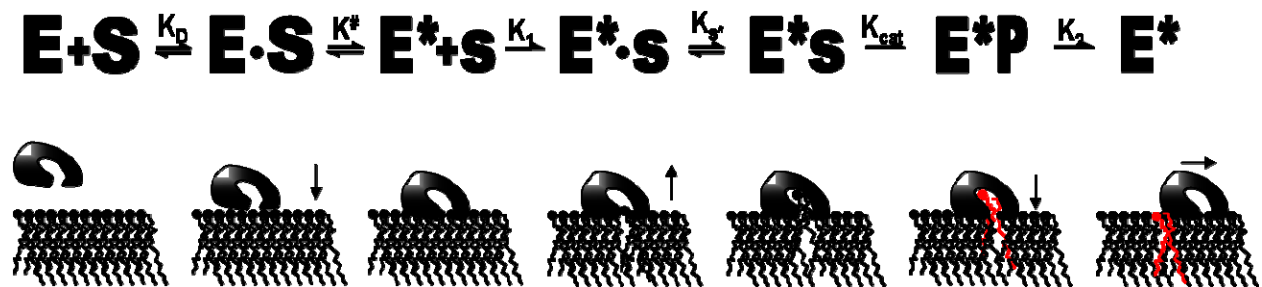
Figure 35 Expanded interfacial kinetic scheme
Expanded schematic diagram of the interaction between an interfacial enzyme and its aggregated substrate. E* denotes the membrane bound enzyme, S the aggregated substrate, s the single phospholipid substrate and P the products which are shown in red. The plus sign, (+) indicates separate entities, the dot indicates a loose association, the absence of either is the complex of either bound enzyme and substrate, or bound enzyme and product. The rate constants are: dissociation (K_D); interfacial activation ($K^\#$), which has been moved to an earlier point describing the change in enzyme-aggregate interaction from a loose association to a close dehydrated state; recognition of the substrate by the activated enzyme (K_1), movement of the momomeric substrate into the enzyme (Ks^*); the rate of catalysis (K_{cat}), which includes the dissociation of product back into the aggregate; and the movement of the enzyme across the interface (K_2).

The two bound states, inactive and active, have been clearly demonstrated by experimental and theoretical approaches. This certainly defines the first step in activation, hence the rearrangement of the activating step, and activating rate constant, $K^\#$.

K_1 describes the infinitely brief interval between the tightly bound enzyme without enzyme and the initial recognition of the monomeric substrate: E*+s → E*·s. The inclusion of this step is necessary, in order to isolate the transfer of the monomeric substrate from the aggregate into the enzyme, decoupling the rate constant constrained by the state of hydration between the enzyme and aggregated substrate, from the catalytic event. K_{s^*} is redefined as the

rate constant for the transfer of the substrate monomer as it moves from its energetically favorable environment in the aggregate across the interface into the hydrophobic environment of the enzyme. Factors which determine this rate are: i) the presence of the divalent cation, calcium within the binding cleft, evidenced by the dependence of calcium on substrate binding [71]; ii) the size of the opening to the cleft, evidenced by the differences seen between IB, IIA and group V [104; 141]; iii) key residues that interact with the headgroup of the substrate, Lys^{56} for group IB and Glu^{56} for group IIA [104; 142]; and iv) the distance which must be traversed, which determines the amount of water the substrate encounters in between the two hydrophobic environments, evidenced by the two bound states and the correlation of increased activity with increased dehydration resulting from the increase of anionic charge in the membrane reported by Gadd and Biltonen, 2000 [140].

In soluble enzymes, substrate binding is mediated by diffusion of the substrate into the binding pocket of the enzyme. The steady state rate, or v_{max} is attained, when the concentration of substrate is much greater than the concentration of enzyme, effectively eliminating the rate limiting constraint of diffusion. With interfacial enzymes, in theory, the concentration of monomeric substrate is at a maximum, as the nature of the aggregate provides maximum packing of the substrate, which in turn is in physical contact with the enzyme. The lateral movement of the enzyme across the interface is implicit in the catalytic turnover step, along with the product dissociation from the enzyme, defined by Jain et al., 1986 [143] as the "scooting mode". Therefore, in order for the enzyme to reach v_{max}, the accessibility of uncleaved substrate by movement of the enzyme across the aggregate must be unimpeded. Therefore, I include the contribution of lateral movement of the enzyme as a separate event with a unique rate constant, k_2. The maximum facilitated transfer of substrate into the catalytic cleft, combined with the rapid

replenishment of uncleaved substrate seen in the 'scooting mode' is analogous to supersaturating solution enzymes, and true v_{max} is revealed.

The final piece to the puzzle clearly defining the mechanism of interfacial activation is found in an obscure work in the early development of molecular dynamics (MD), a simulation of the interaction between separate molecular entities, such as PLA$_2$ and its aggregated substrate [144]. The molecular dynamics study entailed simulating the binding of hIIA PLA$_2$ onto dilauryl-phosphatidylethanolamine (DLPE) *in silico*. The conformation, dynamics and energetics of the enzyme both in solution and bound to DLPE in two different modes: loose and tight were evaluated. The interactions between protein and lipid molecules were analyzed and the free energies of solvation for the lipids at the interface, as well as dielectric susceptibilities at the interface, were calculated. The results clearly show a dehydration of the headgroup region of the membrane only in the tight configuration, and reveal a thin layer of water molecules between the enzyme and substrate interface in the loose configuration. The elusive mechanism of interfacial activation was revealed in the calculations of the free energies of solvation, a measure of the energy barrier required to cross in order for a substrate monomer to transfer from the stable environment of aggregated lipids into the enzyme. The required lowering of the energy barrier was localized <u>only</u> to the lipids interacting with the hydrophobic residues surrounding the opening to the active site, the hydrophobic collar, making them "ideally situated to induce an accelerated diffusion of lipids into the enzyme". This accelerated diffusion enables the realization of the enzyme's true v_{max}, and because it is inextricably tied to the state of dehydration, has only been indirectly detected as interfacial activation.

The clear dependence of interfacial activation on the orientation of the enzyme to the substrate can now be demonstrated. Beers et al., 2003 [74], individually mutated each of the

hydrophobic collar residues found in hIIA PLA$_2$ to Trp, including Val^3. The results from the activity and binding assays were seemingly inconsistent, most notably with the V3W mutation. However a Val^3, Val^{31} double mutant, (V3,31W), consistently demonstrated the highest rate of activity on either 100% DOPG vesicles in a high salt buffer, or on 100% DOPC vesicles with 0.1 M NaCl in the buffer. They noted that the double mutant displayed a similar ability to effectively catalyze either zwitterionic or anionic substrate demonstrated by group V PLA$_2$, but could not offer a definitive explanation for the seeming lack of specificity (group V has a native Trp^{31}, but not Trp^3, it has a Leu^3 instead). It is now necessary to look at the tertiary structure of hIIA PLA$_2$ to understand the consequence of the V3,31W double mutant as it pertains to orientation and interfacial activation. Several atomic resolution structures have been determined, 1N29 [117] is the solution structure of the N1A mutant hIIA PLA$_2$ used in this work, but we will also use 1POD [104], used by Canaan et al., 2002 [94], to orient the molecule to micelles spin labeling results, and 1BBC [145] used by beers to model the 15 degree difference in orientation on 20% or 100% DOPG^{74}. Both 1POD and 1BBC are wild type hIIA PLA$_2$ structures determined by X-ray crystallography. In all three structures, it is clearly evident that the Val^3 and Val^{31} residues reside on opposite sides of a 'hinge' created by Phe^{24} and Phe^{70}. A similar hinge was described by Canaan et al., 2002,[94] across Lys^{10} and Phe^{63} (Phe^{70} by the core numbering system) but was based on 1POD, with the stated assumption that the conformation of the enzyme does not change significantly upon interfacial binding.
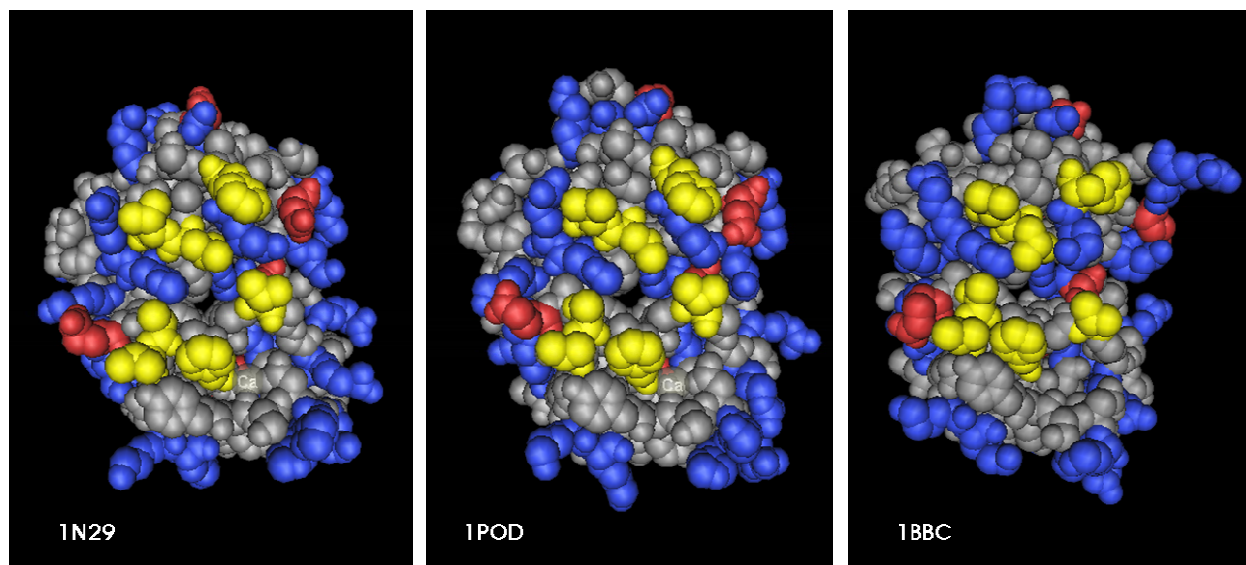
Figure 36 Space filled models of hIIA PLA$_2$
Comparison of three atomic resolution structures of hIIA PLA$_2$, demonstrating motional flexibility of surface residues. hydrophobic collar residues are in yellow, cationic residues blue and anionic residues red. Structures rendered with CN3D, NCBI's structure visualization program [146].

There is no doubt that the tertiary structure is relatively rigid, as it is held together by disulfide bonding, but the sidechains, which are exposed to solvent, are not constrained, so should be quite flexible. A side by side examination of space filling models of 1N29, 1BBC and 1POD, reveals very different conformations for every external residue (Figure 36).

In addition, preliminary results from NMR spectra of $^{15}N^{13}C$ labeled hIIA PLA$_2$ both free in solution and membrane bound, determined by our collaborators, Jeffery Urbauer at the University of Georgia, reveal significant structural changes that occur in the presence of d38-dodecylphosphocholine (DPC) micelles, as is indicated by chemical shift changes of many of the observed peaks (Figure 37, Table 12).
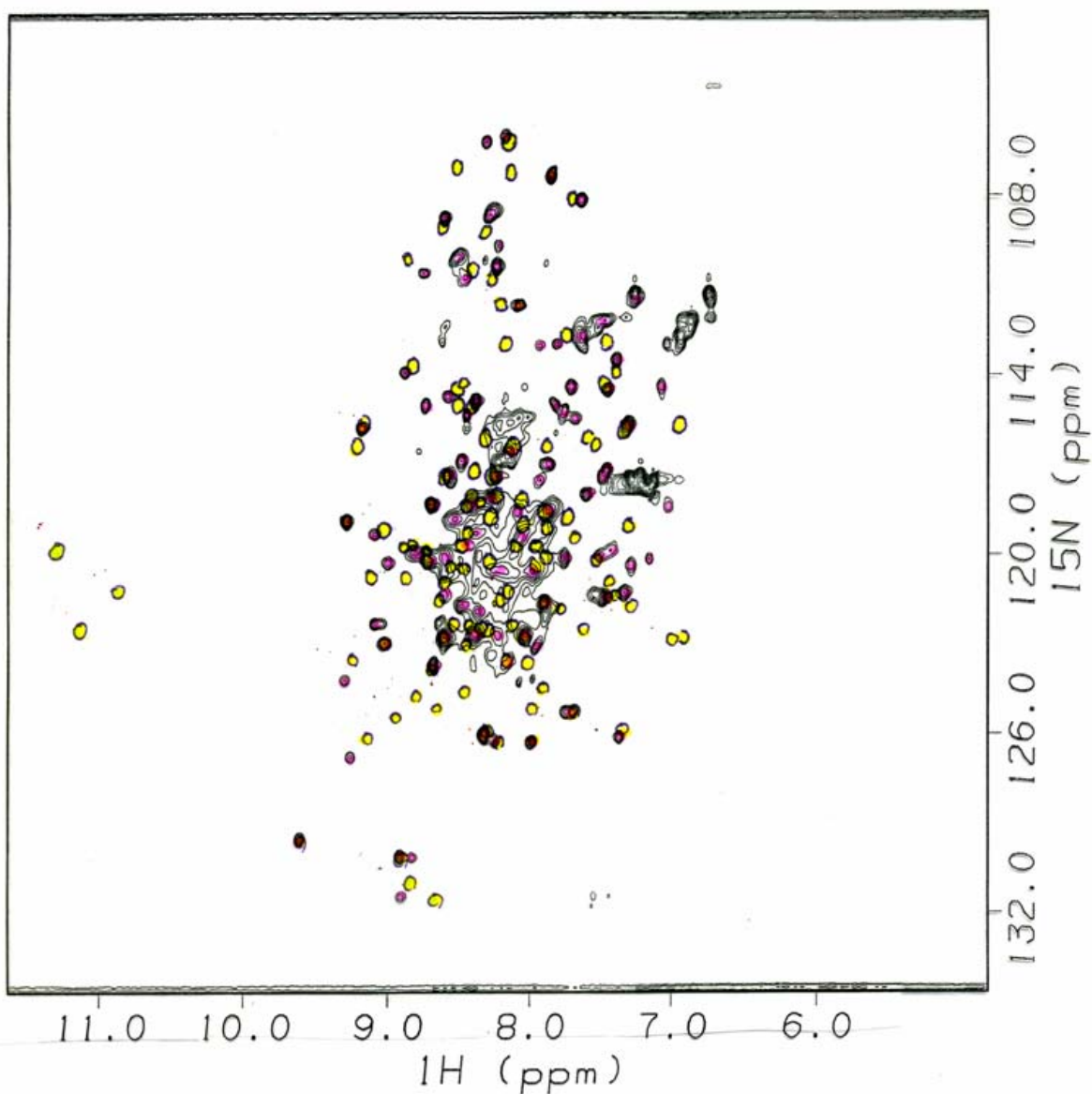
Figure 37 NMR 2D spectra of hIIA PLA$_2$

Overlay of 2D ^{1}H, ^{15}N-HSQC NMR spectra of calcium loaded human group IIA phospholipase A2. Final protein concentration was ~1 mM [U-^{13}C, ^{15}N] hIIA PLA$_2$, in the presence (red) and absence (yellow) of 100 mM d38-dodecylphosphocholine (DPC). The spectrum were acquired at 600 MHz, 25 ºC, in a buffer containing 50 mM NaCl, 5 mM EGTA, 25 mM CaCl$_2$, 5 mM d4-imidazole and 0.02 % sodium azide in 93 % H$_2$O, 7 % D$_2$O, pH 6.5 (pH reading not corrected for D$_2$O isotope effect). The main chain resonance assignments have been completed, following a standard triple resonance approach.

Peaks that did not move		peaks that have shifted			Peaks that have moved completely			
G14	S69	E16	K67	Y111	L2	G25	V45	Q86
	N70	A17	F68	Y112	V3	C26	T46	C88
R57	S71	A18	S73	S113	N4	H27	H47	E89
G58	G72	G34	R84	R118	F5	C28	A48	C90
C59	R74	D38	S85	G119	H6	G29	C50	K92
	I75	A39	A93	S120	R7	V30	Y51	T96
	T76	D41	A94	T121	M8	G32	K52	F98
	C77	R42	A95	P122	I9	R33	R53	N101
	A78	C43	A99	R123	K10	S35	G60	K102
	K79	C44	R100		L11	K37	T61	T103
	Q80	C49	T104		T12	K40	R62	K107
	D81	L54	Y105		T13		F63	Y109
	C83	E55	N106		K15		L64	Q110
	L87	K56	K108		L19		S65	N114
	D91				S20		Y66	K115
	C97							H116
	C124							C117

Table 12 Assigned peaks from NMR spectra overlay
Out of a total of 116 assigned peaks, 21 did not move, 37 shifted and 58 moved completely, giving 18, 32 and 50%, respectively. The residues are clustered according to sequence.

According to Dr Urbauer, these results demonstrate a strong, dynamic interaction of the enzyme with the micelles.

An inspection of the Cartesian coordinates for the hydrophobic collar residues reveal a planar topology for Phe[24] and Phe[70] residues, which sits above another plane, in which lie the smaller Val[3] and Val[31] residues (Figure 38). The hinge relationship of these four residues can be described as a four legged table with two shorter legs on diagonal corners. Replacing both valines, the shorter legs, with tryptophans (V3, 31W) would effectively eliminate the ability of the table to wobble back and forth (the hinge effect) about the line connecting the two longer legs. Thus the balancing of the bulkier Phe residues with residues that demonstrate an affinity to

sit at a specific depth in the interface would facilitate and induce the localized dehydration which mediates interfacial activation.
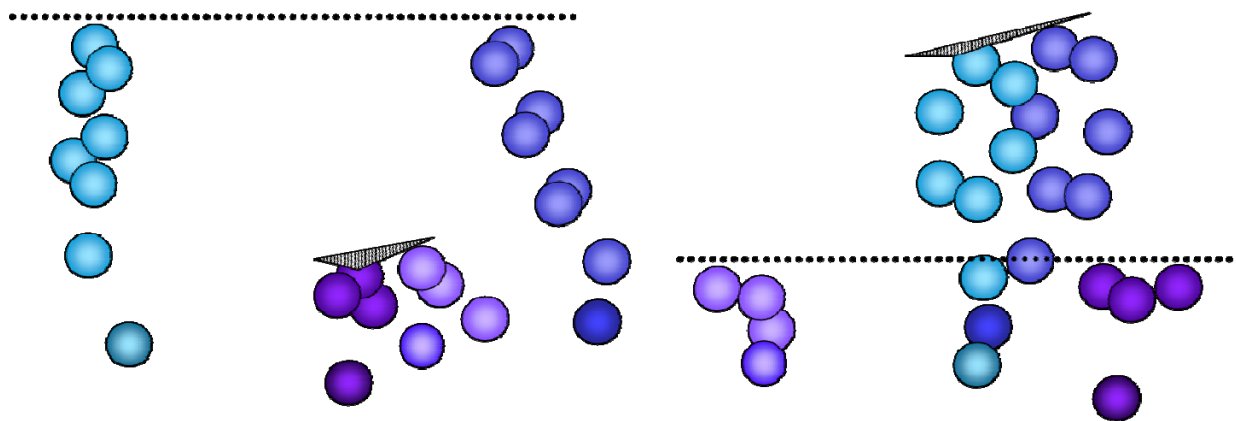
Figure 38 Two planes
The hydrophobic collar residues Phe[24] (light blue) and Phe[70] (dark blue), lie in one plane perpendicular to the page; while Val[3] (light purple) and Val[31] (dark purple) lie in a lower plane nearly parallel to the first. Each plane is defined by a third residue, Leu[19] and Ala[18], respectively, not shown for clarity. The view in the right panel is approximately 90°, rotated counter-clockwise, from the left panel.

Applying the same logic to the inconsistent rates exhibited by the single V3W mutation toward zwitterionic membranes, presented in the same work as V3,31W [73], reinforces the dependence of interfacial activation on orientation. The role Trp[3] in the ability of IB PLA$_2$ to hydrolyze zwitterionic membranes was clearly demonstrated by the reduction in catalytic activity by the Trp[3] to Phe mutation of hIB PLA$_2$ [147]. As Trp has been shown to specifically interact with hydrophobic interfaces, it can be assumed that the substitution of Val with Trp would induce a tighter interaction with the membrane, hence the observed catalysis of zwitterionic substrate by both the V3,31W and V3W mutant of hIIA PLA$_2$. However as noted by Diraviyam and Murray, 2006 [96], the apparent 'blindness' of the wild type hIIA PLA$_2$ can be solidly attributed to a repulsion of the cationic residues dispersed over the entire enzyme by the cationic charges in the zwitterionic substrate. These two diametrically opposite forces along the IBS of V3W, orient the

99

enzyme in such a way as to exploit the inherent dynamic nature of the N-terminal helix, as well as the flexibility of the same helix and at the same time optimize the hydrophobic interactions at the opening to the substrate binding pocket. The result of this unique orientation of V3W is seen in the exceedingly large rate enhancement, and subsequent 'deactivation' in the activity profile on 15% PG presented in this work. The large rate reduction seen here can be attributed to the accumulation of the anionic products, which effectively reverses the electrostatic repulsion effects, and consequently reorients V3W in a manner similar to the wild type, and therefore, demonstrates a similar catalytic rate as the wild type. (This proposed similarity in orientation between V3W and hIIA PLA$_2$ on substrate aggregates with greater than 30% anionic substrate, is seen in the absence of any major differences detected by the variety of biophysical methods used in this work.) The dramatic change in the catalytic efficiency of hIIA PLA$_2$ by a single key interfacial binding residue change, can thus be attributed to the orientation of the enzyme to the aggregated substrate.

CHAPTER FIVE: CONCLUSIONS

We produced large quantities of labeled and unlabeled pure protein, suitable for structural determination, through calculated modifications of established protocols. We evaluated the biochemical and structural consequences of two conservative, single residue substitutions, located at key positions within the primary sequence of hIIA PLA_2. We also evaluated the hIBΔN10 fragment, missing the N-terminal alpha helix, as well as the substitution of that helix with the N-terminal alpha helix from hIIA PLA_2. We compared the engineered proteins against both the hIIA and hIB PLA_2 native enzymes and their N-terminal peptides, N10-hIB and N10-hIIA. We implemented a novel algorithm, in order to position the segmentally labeled hIB and hIIA/IB chimeric PLA_2 onto the aggregated substrate in an experimentally determined orientation. These results reveal subtle structure function relationships that contribute to the regulation of the specificity, allosteric modulation and catalytic rate of these very significant enzymes. This work clearly underscores the functional importance of the residues Trp^3 and Phe^5, in that Trp^3 in the V3W mutant facilitates the productive mode binding of hIIA PLA_2 to membranes where Trp^5 in the F5W mutant tends to interact with the membrane and hence causes conformational perturbation in the protein. In addition, this work provides evidence that structurally similar group hIB and hIIA PLA_2s, significantly penetrate into membranes and that membrane insertion is controlled by membrane fluidity and facilitates activation of hIIA and hIB PLA_2s. In addition, we show that the N-terminal helix of group I/II PLA_2s acts as a regulatory domain which mediates and supports interfacial activation of these enzymes by enhancing the membrane binding strength, conferring conformational integrity and plasticity to the enzyme and ultimately facilitating a productive-mode orientation of $shPLA_2$ at the membrane interface.

The major contribution of this work, is the reconciliation of the existing body of knowledge with our current work, yielding a comprehensive proposal for the mechanism of interfacial activation: i) the orientation of the enzyme to the substrate, mediated by specific IBS residues such as Trp³, determines the level of dehydration of the hydrophobic collar residues surrounding the opening to the catalytic cleft, ii) the level of dehydration modifies the energies of solvation, the energy barrier which must be crossed as the monomeric substrate is transferred from the aggregate to the interior of the enzyme. The lag phase on zwitterionic substrates is a result of this rate limiting state, iii) total dehydration of the interface, the result of a tight interaction induced by specific IBS residues such as cationic residues on an anionic surface, reduces the energy barrier to such an extent that the lowest energy state for the monomeric substrate is no longer in the aggregate but within the enzyme. The burst of activity induced by anionic product is a result of the interaction of this rate limiting condition. In short, the specific orientation, including the depth of membrane insertion, of the enzyme toward its aggregated substrate mediates the optimum activity of the enzyme, and by extension, is the mechanism for interfacial activation.

The future direction of this work will entail reinforcing the validity of our conclusion. The experimental design will incorporate ATR-FTIR methods in order to determine the relative orientation of the enzyme to its substrate, via R^{ATR} of the hIIA PLA$_2$, V3W and F5W enzymes on supported bilayers composed of varying concentrations of negative lipids. The base lipids will be POPC and DPPC to characterize the orientation on a liquid order or gel phase substrate. Additionally, segmental labeling of hIIA PLA$_2$ and V3W will yield the $R\alpha^{ATR}$ values, enabling the precise orientation of the N-terminal helices relative to H2 and H3 on different compositions of zwitterionic and anionic substrates such as DPPC, DPPG, POPC and POPG. The activity of

the three enzymes will be correlated to their orientation through BisPy-PC fluorescence based activity assays. The data will be compared to molecular dynamics simulations of the enzymes on respective lipid substrates, generated using the updated MD software package (which models atomic interactions, enabling a visualization of the movement of residues within the aqueous or nonpolar matrix).

A new hypothesis arising from these conclusions will also be tested using the above interdisciplinary experimental design: The translocation of the PLA_2 enzyme, across the surface of the aggregated substrate, is facilitated by the electrostatic repulsion of the single anionic residue on the IBS of the enzyme with the newly formed anionic product in the membrane.

APPENDIX A: EQUATIONS

Equations 1 Determination of extinction coefficients

Unique extinction coefficients for hIIA PLA$_2$, V3W, F5W and hIB PLA$_2$ were determined using the Beer-Lambert law:

$$A_\lambda = \varepsilon c l \qquad \text{(Eq. 1)}$$

Where A_λ is the measured absorbance at a specific wavelength (λ), ε the extinction coefficient, c is the molar concentration, and l the pathlength through the cuvette, 0.4 cm in these experiments. The molar concentration was determined using the molecular weights of the proteins based on the amino acid sequence.

Equations 2 Specific Activity

Phospholipase A$_2$ activity was recorded as the change in absorbance at 414nm (A_{414}) over a one minute interval and applied to Eq. 1 using the extinction coefficient of 5-thio-nitrobenzoic acid (ε_{414} = 13,600 M^{-1} cm^{-1}) and pathlength of 0.4cm. As the reaction progress is 1:1 (cleaved product:5-thio-nitrobenzoic acid), the concentration of 5-thio-nitrobenzoic acid equals the concentration of product. Dividing the concentration of product by the total amount of enzyme within the reaction gave the specific activity in moles of product released in one minute per mg of enzyme.

Equations 3 BisPy-PC

Phospholipase activity against bis-pyrene labeled LUVs. The hydrolysis of BisPy-PC by PLA$_2$ separates the two pyrene functional groups on the terminus of the *sn-1* and *sn-2* acyl chains of the phospholipid, resulting in a decrease in the excimer signal at 470 nm and an increase in the monomer signal at 380 nm. There is not a linear relationship between the eximer and monomeric signal therefore, the amount of BisPy-PC cleaved at any timepoint is expressed as the ratio of the monomeric signal to the eximer signal at time t:

$$R_t = \left(\frac{F_{380}}{F_{470}} \right)_t$$

And the rate of activity was graphically represented as

$$\frac{R_t}{R_0} - 1$$

over time, where R_0 is the ratio of fluorescence intensities at 380 and 470 nm before the addition of enzyme.

Equations 4 FPE

Membrane binding on vesicles labeled with 2 mol% N-(fluorescein-5-thiocarbamoyl)-1,2-dihexadecanoyl-*sn*-glycero-3-phosphoethanolamine (FPE). The fluorescence intensity of FPE is sensitive to the ionization state of the carboxyl group of fluorescein; the emission intensity increases with increasing deprotonation [81]. The fluorescein moiety of FPE is located at the interface of the negatively charged membrane, where the local environment is more acidic than the bulk phase because of electrostatic attraction of protons to the membrane. This causes partial protonation of the carboxyl group of fluorescein, resulting in a moderate level of fluorescence intensity. Adsorption of cationic protein or peptide molecules to the membrane reduces the negative surface charge of the membrane, which results in a protein (or peptide) dose-dependent deprotonation of fluorescein and increase in the fluorescence intensity. The protein is added to preformed lipid vesicles, resulting in binding of the protein to the external surface of vesicles. If one considers that only a fraction δ of the total lipid is accessible to the protein, and the binding of each protein molecule makes N lipid molecules inaccessible for other proteins, then the dissociation constant of the binding process can be presented as:

$$K_D = \frac{\left([P]-[P]_b\right)\left(\delta[L]-N[P]_b\right)}{N[P]_b}$$

(Eq. 2)

where $[P]$ and $[L]$ are the total concentrations of the protein and the lipid, respectively, and $[P]_b$ is the concentration of the membrane-bound protein. When the lipid fluorescence is monitored as the lipid is being titrated with the protein, the relative change in the fluorescence signal is:

$$\frac{\Delta F}{\Delta F_{\max}} = \frac{[L]_b}{\delta[L]}$$ (Eq. 3)

where ΔF is the change in fluorescence intensity at a given protein concentration, $\Delta F_{\max}$ is the saturating level of ΔF at high protein concentration, and $[L]_b$ is the concentration of protein-bound lipid. We have used ΔF values at 518 nm. Using:

$$[P]_b = [L]_b/N = \Delta F_{rel}\delta[L]/N$$

where $\Delta F_{rel} \equiv \Delta F/\Delta F_{\max}$, we convert Equation 2 into a quadratic equation with respect to ΔF_{rel} and solve as:

$$\Delta F_{rel} = a - \sqrt{a^2 - \frac{N[P]}{\delta[L]}}$$ (Eq.4)

where $a = \dfrac{1}{2}\left(\dfrac{N(K_D + [P])}{\delta[L]} + 1\right)$ (Eq.5)

The plus sign in front of the square root is useless because it results in values of $\Delta F_{rel} > 1$. It is seen from Equation 2 that at half-saturation of protein binding, when $\Delta F_{rel} = 0.5$:

$$K_D = [P]_{1/2} - \frac{\delta[L]}{2N}$$ (Eq. 6)

where $[P]_{1/2}$ is the protein concentration corresponding to $\Delta F_{rel} = 0.5$.

Changes in FPE fluorescence intensity, ΔF, were measured at various protein concentrations, $[P]$, and ΔF were plotted against $\Delta F/[P]$. These linear (Scatchard) plots were used to evaluate ΔF_{max} and $[P]_{1/2}$ from extrapolated intercept with the ΔF axis and from the slope, respectively. Experimental binding isotherms were constructed by plotting $\Delta F/\Delta F_{max}$ against $[P]$. The theoretical isotherms were simulated through Equation 4 using K_D and N as fitting parameters. In spite of two fitting parameters, determination of both K_D and N by this method is reliable. In Equation 6, $[P]_{1/2}$ can be determined using the experimental data, as described above, and δ is 0.52 for vesicles 100-nm in diameter, with membrane thickness of 4 nm [83]. Replacement of K_D in Equation 4 by the expression in equation 6 yields an equation with only one unknown, i.e. N. Hence, fitting of the experimental curves can be done by varying N in a physically reasonable range and, once a best fit is achieved, K_D can be calculated through Equation 6 using the heuristically determined best fit value of N.

Membrane binding on vesicles containing 2 mol% Py-PE. Fluorescence intensities obtained in RET experiments were corrected for dilution and for the increase in the fluorescence emission as measured in control experiments. This was followed by calculation of the changes in emission intensities at 330 nm for N10 peptide or full-length PLA_2 and at 304 nm for $\Delta N10$ fragment at each lipid concentration relative to the zero lipid level, ΔF. The first step of the data analysis was evaluation of the saturating value of ΔF at high lipid concentrations, i.e. ΔF_{max}, and the lipid concentration corresponding to half-saturation of binding, $[L]_{1/2}$, at which $\Delta F = \frac{1}{2}\Delta F_{max}$. In order to do this, binding data were presented using a simple, Langmuir-type formalism:

$$\Delta F = \Delta F_{max} \frac{[L]}{[L]_{1/2} + [L]} \qquad \text{(Eq. 7)}$$

where $[L]$ is the total lipid concentration. Equation 7 can be re-arranged to show that the plot of ΔF as a function of $\Delta F/[L]$ (Scatchard plot) is a straight line with a slope of $-[L]_{1/2}$ and a ΔF-axis intercept of ΔF_{max}. The Scatchard plots were constructed, using ΔF values at each $[L]$, and the parameters ΔF_{max} and $[L]_{1/2}$ were evaluated from the plots. Then, the values of ΔF_{max} were used to construct the experimental binding isotherms, i.e., the dependence of $\Delta F/\Delta F_{max}$ as a function of $[L]$. In order to describe the protein-lipid interaction, a bimolecular binding model was used[148; 149]. According to this model, each free protein molecule binds to an unoccupied binding site at the membrane surface. The lipid vesicles and the protein are mixed in a way that only a fraction

$\delta[L]$ of the total lipid (i.e., the external lipid leaflets of vesicles) is accessible for the binding of the peripheral protein. The bimolecular binding process can be described as:

$$P_f + \delta L_f \Leftrightarrow L_b \qquad \text{(Eq. 8)}$$

where the subscripts f and b indicate the free and bound state of the protein (P) or the lipid (L). The dissociation constant of this binding process is:

$$K_D = \frac{[P_f][\delta L_f]}{[L_b]} \qquad \text{(Eq. 9)}$$

where the brackets mean concentration. Also, since the area of the interfacial binding surface of PLA$_2$ (~1700 Å^2) [60] is much larger than the cross-sectional area of POPC or POPG (68 Å^2) [150], $N \gg 1$ lipid molecules are likely to be involved in formation of a binding site, i.e., $[L_b] = N[P_b]$. Additionally, the number of lipids that constitute a binding site (N) for group I/II PLA$_2$s was determined in several studies and varied between 28 and 48 [66; 151; 152]. The parameter N should not be interpreted as the number of lipids that physically interact with a PLA$_2$ molecule. Instead, this is the effective number of lipids that constitute a protein binding site and become inaccessible to other proteins upon binding of a PLA$_2$ molecule to the membrane surface.

Also, $[P_f] = [P] - [P_b]$, and $\delta[L_f] = \delta[L] - N[P_b]$. A key assumption of the model is that the change in the protein fluorescence intensity at each lipid concentration is proportional to the fraction of lipid-bound protein, i.e., $[P_b]/[P] = \Delta F/\Delta F_{max} \equiv \Delta F_{rel}$. Introducing all these into equation 9, we obtain:

$$K_D = \frac{([P] - \Delta F_{rel}[P])(\delta[L] - \Delta F_{rel}N[P])}{\Delta F_{rel}N[P]} \qquad \text{(Eq. 10)}$$

Equation (10) can be converted into a quadratic equation with respect to ΔF_{rel} and solved as:

$$\Delta F_{rel} = b - \sqrt{b^2 - \frac{\delta[L]}{N[P]}} \qquad \text{(Eq. 11)}$$

where $b \equiv \dfrac{1}{2}\left(1 + \dfrac{\delta[L]}{N[P]} + \dfrac{K_D}{[P]}\right)$.

In equation (11), the plus sign in front of the root is not used because it yields physically meaningless (i.e., > 1) values for ΔF_{rel}. At half-saturation of protein binding to membranes, $[L] = [L]_{1/2}$, $\Delta F_{rel} = 0.5$, and $[P_b] = \frac{1}{2}[P]$. Insertion of these in equation (10) yields:

$$K_D = \frac{\delta}{N}[L]_{1/2} - \frac{[P]}{2} \qquad \text{(Eq.12)}$$

In equation (12), the total protein concentration, $[P]$, is known, $[L]_{1/2}$ can be determined from the experimental binding isotherms, as described above, and the fraction of the protein-accessible lipid, δ, i.e., the fraction of the lipid in the external leaflet of 100-nm (in diameter) POPC/POPG vesicles with membrane thickness of 4 nm is ~0.52 [153]. Thus, the dissociation constant, K_D, can be determined based on an experimental binding isotherm provided the number of lipid molecules involved in a binding site, N, is known. We have used physically reasonable values for

N to calculate corresponding values for K_D through equation (12), and have used them to construct theoretical curves, using equation (11), until a best fit with the experimental binding isotherm was reached.

This is an accurate and stringent approach to determine binding parameters because it does not allow selection of any values of K_D and N for fitting the experimental results. There is only a unique pair of parameters K_D and N, which are interrelated through equation (12) that can provide a best fit with the experiment. Binding energies were deduced from dissociation constants as $\Delta G_b = -RT(\ln[W] - \ln K_D)$, where $[W]$ is the molar concentration of water (55.4 M at 25 °C), and $RT = 0.592$ kcal/mol at 25 °C.

Equations 6 DQ

Dual fluorescence quenching experiments with acrylamide and 10DN. Membrane insertion of Trp residues was determined by fluorescence spectroscopy. The samples were contained in a 4×4 mm^2 rectangular quartz cuvette, with constant stirring. Excitation and emission slits were 4 and 10 nm, respectively. Tryptophans were selectively excited at 290 nm, and the emission spectra were recorded between 300 and 400 nm, followed by spectral correction by subtracting the spectra measured under identical conditions but without the protein or peptide. In experiments of Trp fluorescence quenching with acrylamide, PLA$_2$ or peptide solutions were prepared in buffers that contained 1 mM EDTA, 50 mM HEPES (pH 7.4) and varying concentrations of acrylamide, emission spectra were measured, maximum fluorescence intensities without and with the quencher (F_0 and F respectively) were determined, and F_0/F values were plotted against the acrylamide concentration.

The slopes of the best-fit linear plots were used to determine the Stern-Volmer quenching constants (K_{SV}). The experimental data were fitted with the Stern-Volmer equation

$$\frac{F_0}{F} = 1 + K_{SV}[Q] \tag{Eq. 13}$$

where [Q] is the quencher concentration. The total concentration of the lipid, when present, was 0.5 mM.

In dual quenching experiments, Trp emission intensity was measured in the presence of lipid vesicles with no quencher (F_0), in the presence of vesicles and with 250 mM acrylamide in the

buffer (F_{acrly}), and in the presence of vesicles containing 10 mol% 10DN with no acrylamide in the buffer (F_{10DN}). The dual quenching ratio, R_{DQ}, was determined as described earlier [154; 155]:

$$R_{DQ} = \frac{F_0 / F_{acryl} - 1}{F_0 / F_{10DN} - 1}$$ (Eq. 14)

Values of $R_{DQ} < 1$ indicate that the fluorophore is efficiently shielded from the aqueous phase by membrane insertion, while exposure of the fluorophore to the aqueous phase yields $R_{DQ} \gg 1$.

Depth dependent Trp quenching by Br$_2$PC labeled vesicles. The depth of membrane insertion was quantitatively determined by using differential quenching of Trp fluorescence by Br$_2$PCs brominated at 6,7-, 9,10-, or 11,12-, positions of the *sn-2* acyl chain. Br$_2$PCs were incorporated in vesicles at 20 mol%. Initially, Trp fluorescence spectra of the protein or the peptide were measured in the presence of lipid vesicles composed of POPC and POPG, and the emission intensity at 350 nm was measured and designated F$_0$. Then, Trp emission intensities at 350 nm (F) were measured in the presence of vesicles in which 20 mol% of POPC was replaced by each of the three Br$_2$PCs. The values of ln(F$_0$/F) were calculated and plotted against the distance of the bromine atoms from the membrane center, i.e., 11.0, 8.3, and 6.5 Å for 6,7-, 9,10-, and 11,12- Br$_2$PCs, respectively [88]. The experimental data were described using the distribution analysis [156; 157]:

$$ln\frac{F_0}{F} = \frac{S}{\sigma\sqrt{2\pi}}exp\left[-\frac{(h-h_m)^2}{2\sigma^2}\right] \qquad \text{(Eq. 15)}$$

In Equation 15, S is the area under the distribution curve and is directly proportional to the degree of the exposure of the fluorophore to the quencher, σ is the dispersion of the distribution curve and is determined by the sizes of the fluorophore and the quencher, as well as by structural disorder and heterogeneity of the system, h is the distance from membrane center, and h$_m$ is the most probable location of the fluorophore with respect to the membrane center.

Equations 8 CD

Ten scans were averaged between 260 and 180 nm and corrected for the background signal by subtracting the spectra of the appropriate control samples without protein. The mean residue molar ellipticity, $[\theta]$, was calculated as:

$$[\theta] = \frac{\theta_{meas}}{c n_{res} l} \qquad \text{(Eq. 16)}$$

where θ_{meas} is the measured ellipticity in millidegrees, c is the molar concentration of the protein, n_{res} is the number of amino acid residues in the protein, and l is the optical path-length in mm.

Polarized amide I spectra cannot be used for determination of protein secondary structure, because the intensities of amide I components corresponding to different secondary structures depend not only on their content in the protein but also on their orientation relative to the electric vector of the plane-polarized light [116; 158]. Figure 39 illustrates the general relationship between an oriented membrane bound protein with two alpha helices to the ATR-FTIR system of polarized light, evanescent field and electric vector components E_x, E_y and E_z..
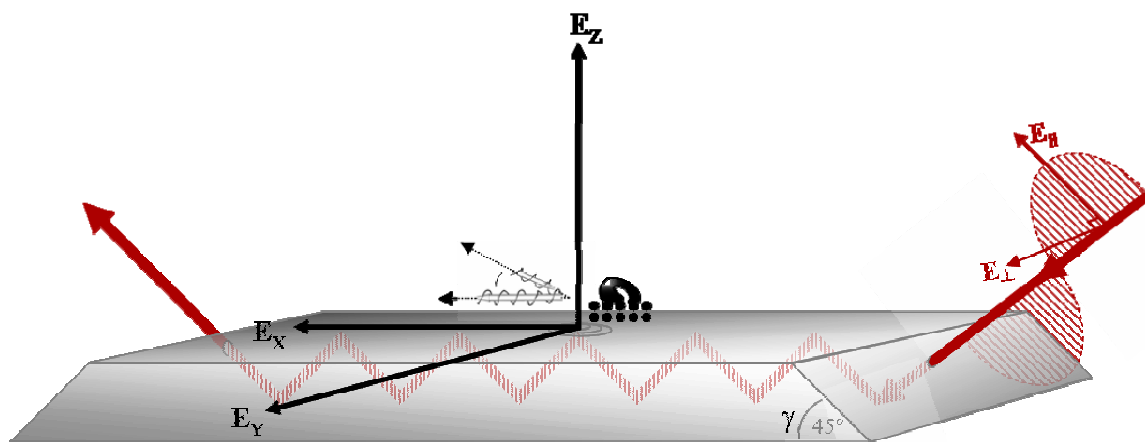
Figure 39 Internal reflection element
Illustration of the path of a single beam of parallel polarized infrared light reflected on the internal faces of a germanium plate: γ is incident angle of the incoming light; $E_{\parallel}$ and $E_{\perp}$ are the electric vectors for parallel and perpendicular polarizations, respectively. The orthogonal components of the electric vector of the evanescent field are E_x, E_y, and E_z. The evanescent field is generated at the point of internal reflection and exponentially decays in the E_z direction with a decay length of approximately 300 nm. A single enzyme is placed on the surface of the plate in order to demonstrate the relative orientation of the two helices to E_z.

The spectra measured at parallel and perpendicular polarizations can be used to obtain a "polarization-independent" spectrum:

$$A = A_{\parallel} + GA_{\perp} \tag{Eq. 17}$$

where G is a scaling factor and under our experimental conditions $G = 0.8$ (see Ref. [158] for more detail). Following spectral correction, the secondary structure content can be presented as a fraction of the total amide I area:

$$f_{ss} = A_{comp}/A_{total} \tag{Eq. 18}$$

where f_{ss} is the fraction of the secondary structure component, A_{comp} is the area of the amide I secondary structure component, while A_{total} is the total amide I area [116; 158].

Equations 10 HDX

Initiation of amide HDX by exposure of the protein to D_2O results in a shift of amide II band from ~1545 to ~1450 cm^{-1}, allowing determination of the HDX kinetics based on the gradual reduction in the intensity of amide II band around 1545 cm^{-1}. We have conducted the HDX experiments in the presence of EGTA to prevent lipid hydrolysis and the effect of continuously changing membrane structure on the HDX kinetics. The fraction of unexchanged amide protons at time t of exposure of the protein to D_2O is determined as:

$$\frac{H_t}{H_t + D_t} = \frac{A_t}{A_0}$$

(Eq. 19)

where H_t and D_t are the numbers of unexchanged and exchanged amide protons at time t, $A_{,0}$ and A_t are the normalized integrated amide II band areas measured at ~1545 cm^{-1} before and at time t of exposure to D_2O, respectively. In order to eliminate the effects of possible changes in the overall signal, e.g. due to protein adsorption or desorption, the amide II bands were normalized by dividing by the integrated amide I areas at corresponding time points:

$$A_t = \left(\frac{A_{amideII}}{A_{amideI}} \right)_t \quad , \quad A_0 = \left(\frac{A_{amideII}}{A_{amideI}} \right)_0$$

(Eq. 20)

Since the HDX kinetics reflect solvent accessibility and the strength of H-bonding in the protein, this implies that all protein residues can usually be divided into a small number of populations with similar dynamic properties therefore the HDX kinetics is described by a double-exponential function [116; 124]:

$$\frac{H_t}{H_t + D_t} = \frac{A_t}{A_0} = a_0 + a_1 e^{-k_1 t} + a_2 e^{-k_2 t} \qquad \text{(Eq. 21)}$$

where a_0, a_1, and a_2 are the fractions of exchange-resistant, slow exchanging, and fast exchanging residues; and k_1 and k_2 are the rate constants of the slow and fast exchanging populations, respectively.

Equations 11 ATR Dichroic Ratio

The ratio of absorbance intensities at parallel and perpendicular polarizations of the incident light yields the ATR dichroic ratio:

$$R_{AI}^{ATR} = \frac{A_{I\,II}}{A_{I\perp}}$$

which is determined by the orthogonal components of the electric vector of the evanescent field, E_x, E_y, E_z, and the orientational order parameter of the aligned sample (Figure 39). For an isotropic sample, one that is not oriented in a specific manner but is randomly oriented about the z axis, the dichroic ratio is:

$$R_{ISO} = \frac{E_X^2 + E_Z^2}{E_Y^2}$$

$R_{iso} \approx 1.72$ for a lipid membrane supported on a germanium plate in aqueous environment at an incident angle of the incoming light $\gamma = 45$ degrees [116] (Figure 39). If the effect of the lipid bilayer on the evanescent field is neglected, which may be justified because of its diminutive thickness [159], then $R_{iso} \approx 2.0$. This latter consideration is known as a two-phase approximation, while the one that takes the membrane refractive index into account is known as a three-phase approximation. For an α-helix, R_{ATR} values lower or higher than R_{iso} indicate horizontal or vertical orientation of the helix axis relative to the membrane plane, respectively. The physically meaningful limits of R_{ATR} are 1.3-3.6 and 1.4-4.5 for the three-phase and the two-phase approximations, respectively.

Equations 12 Order Parameter

S: Orientation of alpha helices to the membrane normal. Values of R_α^{ATR} can be used to determine the α-helical order parameters, S, by the equation:

$$S = \frac{2B}{(3\cos^2\alpha - 1)(B - 3E_z^2)}$$ (Eq. 22)

Where

$$B = E_x^2 - R_\alpha^{ATR} E_y^2 + E_z^2$$ (Eq. 23)

In these conditions, E_x = 1.9684, E_y = 2.25 and E_z = 1.8906. The angle α is the angle between the amide I transition dipole moment and the alpha helix axis = 38° [160; 161]. (Figure 40)
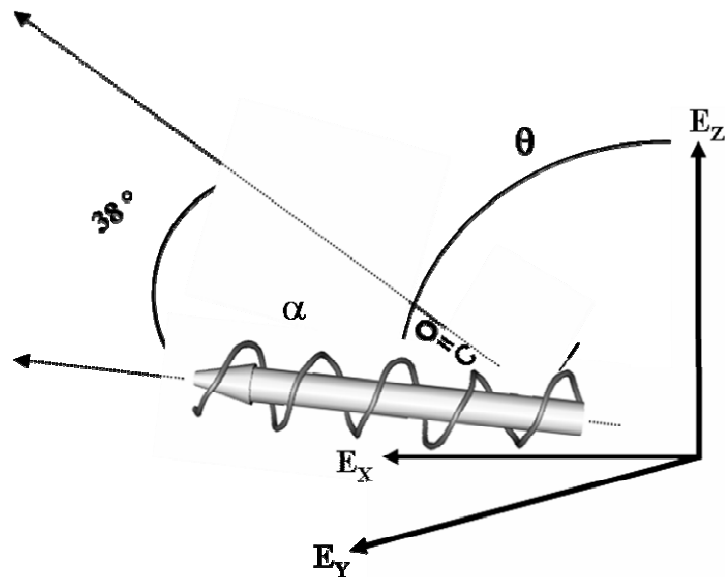
Figure 40 Order parameter
The relationship between an alpha helix, the amide I transition dipole moment and the orthogonal electric vector components, E_x; E_y and E_z. The transition dipole moment is generated by the characteristic alpha helical hydrogen bonding, illustrated by the carbonyl group, the amide group is not shown.

The order parameter can be interpreted in terms of an average angle, θ, (Figure 40) between the helical axis and the membrane normal (E_Z) using the equation:

$$S = \frac{1}{2}\left(3\langle\cos^2\theta\rangle - 1\right).$$

(Eq. 24)

Physically meaningful values of the order parameter (S) vary between -0.5 and $+1.0$, which correspond to orientations parallel and perpendicular to the membrane plane, i.e., $\theta = 90°$ and 0, respectively, while an order parameter close to zero may indicate either a random, isotropic orientational distribution or a fixed orientation at $\theta = 54.7°$.

APPENDIX B: ALGORITHM

Determination of interhelical angles

The main mathematical operation utilized in this algorithm is coordinate transformation between two orthogonal coordinate systems, the "protein" system Σ_p with axes X*Y*Z*, in which the protein atom coordinates are given, and the "intrinsic" helical coordinate system Σ_h with axes $X_H Y_H Z_H$ that are assigned to each helix, with Z_H being the helical axis. The backbone atom coordinates of an α-helix in the system Σ_h can be given as:

$$\left. \begin{aligned} x_{H_{ij}} &= a\cos[100(j-1)] \\ y_{H_{ij}} &= a\sin[100(j-1)] \\ z_{H_{ij}} &= b(j-1) \end{aligned} \right\} \tag{S1}$$

where a is the radius of the helical "cylinder" and b is the height per residue (in the following text, the upper case X, Y, and Z will denote the coordinate axes and the lower case x, y, and z will mean the coordinates). This applies to any set of backbone atoms, with corresponding parameter a (b is a constant for a given type of helix). For example, if C_α atoms are considered (C_α atoms are on the surface of the helical "cylinder"), then for an α-helix $a = 2.25$ Å and $b = 1.5$ Å. In the equation system (S1), the subscript i signifies a certain (ith) helix in the protein molecule and j signifies a certain (jth) amino acid residue in ith helix, moving in an N→C direction. First, we ascribe a "base" to all helices, i.e., a circle that constitutes the base of the helical "cylinder". We translationally move all helices so that the centers of all "bases" coincide with the origin of the Σ_p coordinate system. Note that the initial coordinates of these centers are

0, 0, 0 in the Σ_h system and x_{0i}, y_{0i}, z_{0i} in the Σ_p system. If the atom coordinates in the Σ_p system

originally were x^*_{ij}, y^*_{ij}, z^*_{ij}, now they become x^*_{ij}- x_{0i}, y^*_{ij}- y_{0i}, z^*_{ij} - z_{0i}. We express the

backbone atom coordinates in the intrinsic helical coordinate systems Σ_{hi} through the coordinates

in the protein system Σ_p by means of coordinate transformation:

$$
\left.
\begin{aligned}
x_{H_{ij}} &= (x^*_{ij} - x_{0i})\cos(X^*, X_{Hi}) + (y^*_{ij} - y_{0i})\cos(Y^*, X_{Hi}) + (z^*_{ij} - z_{0i})\cos(Z^*, X_{Hi}) \\
y_{H_{ij}} &= (x^*_{ij} - x_{0i})\cos(X^*, Y_{Hi}) + (y^*_{ij} - y_{0i})\cos(Y^*, Y_{Hi}) + (z^*_{ij} - z_{0i})\cos(Z^*, Y_{Hi}) \\
z_{H_{ij}} &= (x^*_{ij} - x_{0i})\cos(X^*, Z_{Hi}) + (y^*_{ij} - y_{0i})\cos(Y^*, Z_{Hi}) + (z^*_{ij} - z_{0i})\cos(Z^*, Z_{Hi})
\end{aligned}
\right\} \quad \text{(S2)}
$$

Here, cos(A,B) means the cosine of the angle between the positive directions of the axes A and

B. For a given helix, we can write each of the three equations of the system (S2) for four

consecutive residues, starting at the first residue in the helix. This, combined with the equation

system (S1), yields (S3):

$$
\left.
\begin{aligned}
a\cos[100(j-1)] &= (x^*_{ij} - x_{0i})\cos(X^*, X_{Hi}) + (y^*_{ij} - y_{0i})\cos(Y^*, X_{Hi}) + (z^*_{ij} - z_{0i})\cos(Z^*, X_{Hi}) \\
a\sin[100(j-1)] &= (x^*_{ij} - x_{0i})\cos(X^*, Y_{Hi}) + (y^*_{ij} - y_{0i})\cos(Y^*, Y_{Hi}) + (z^*_{ij} - z_{0i})\cos(Z^*, Y_{Hi}) \\
b(j-1) &= (x^*_{ij} - x_{0i})\cos(X^*, Z_{Hi}) + (y^*_{ij} - y_{0i})\cos(Y^*, Z_{Hi}) + (z^*_{ij} - z_{0i})\cos(Z^*, Z_{Hi}) \\
j &= k, k+1, k+2, k+3 \\
k &= 1, 2, ..., m-3
\end{aligned}
\right\}
$$

In the system (S3), m is the number of residues in the helix. If protein backbone atom

coordinates x^*_{ij}, y^*_{ij}, z^*_{ij} are known, for a given helix the system (S3) represents 12 equations

with 12 unknowns, i.e., the nine cosines and the coordinates x_{0i}, y_{0i}, z_{0i}. The system (S3) can be

solved as follows. Each of the three equations of the system can be written in quadruplet, i.e., for

consecutive residues $j = 1$ to 4, or $j = 2$ to 5 and so on up to the end of the helix. Note that this can only be done if the helix involves at least four residues. The equation corresponding to $j = k$ can then be subtracted from those corresponding to $j = k + 1$, $k + 2$, $k + 3$. This yields the following system (S4):

$$
\left.
\begin{aligned}
& 2a \sin \frac{100(j+k-2)}{2} \sin \frac{100(k-j)}{2} = \Delta x *_{ijk} \cos(X*,X_{H_i}) + \Delta y *_{ijk} \cos(Y*,X_{H_i}) + \Delta z *_{ijk} \cos(Z*,X_{H_i}) \\
& 2a \cos \frac{100(j+k-2)}{2} \sin \frac{100(j-k)}{2} = \Delta x *_{ijk} \cos(X*,Y_{H_i}) + \Delta y *_{ijk} \cos(Y*,Y_{H_i}) + \Delta z *_{ijk} \cos(Z*,Y_{H_i}) \\
& b(j-k) = \Delta x *_{ijk} \cos(X*,Z_{H_i}) + \Delta y *_{ijk} \cos(Y*,Z_{H_i}) + \Delta z *_{ijk} \cos(Z*,Z_{H_i}) \\
& k = 1,2,...m-3 \\
& j = k+1, k+2, k+3
\end{aligned}
\right\}
$$

In system (S4), $\Delta x *_{ijk} = x *_{ij} - x *_{ik}$, ($\Delta y *_{ijk}$ and $\Delta z *_{ijk}$ are given by similar expressions). Any of the three equations of the system (S4) then can be written in triplet, i.e., for $k = 1, 2, 3$, or $k = 2, 3, 4$ and so on, and each triplet can be solved to find the three cosines, using the C_α (or other backbone atom) coordinates and the corresponding parameter a or b of the helix. For example, completion of this procedure for an α-helix of the protein using the third equation of the system (S4) will yield cosines that describe the orientations of helical axes (Z_{Hi}) for overlapping stretches of that particular helix with respect to the protein coordinate system Σ_p. In other words, we will learn the orientations of helical segments formed by helical residues 1 to 4, 2 to 5, 3 to 6 and so on. Using the backbone atom coordinates of the protein, we solve the system (S4) for all helices of the protein.

This procedure allows characterization of helices in several respects. First, plots of $\cos(X^*,Z_{Hi})$, $\cos(Y^*,Z_{Hi})$, and $\cos(Z^*,Z_{Hi})$ against the number of residues in a helix will indicate the degree of deviation of the helical axis from linearity. Deviations of the cosines from a constant value will identify helix bending at certain positions and will quantitatively describe the bending. High degree of "noise" in these plots will indicate distorted helices, and vice versa. Second, the average values of the cosines obtained for all helical segments will indicate the average orientation of the entire helix within the protein molecule. If there is a major bend in the helix, averaging of the cosines for segments before and after the bend will provide the bending angle. Third, the data obtained for all helices of the protein will allow determination of the angles between any two helices or between their segments of interest, as described below. This will provide accurate quantitative information on the interhelical angles of the protein.

Besides orientational information, the algorithm also allows one to scan along the helix and gain structural information on any four-residue sections of helices. The quality of helical structure is determined by using the laws of direction-cosines for orthogonal concentric coordinate systems:

$$\cos\delta_i \cos\delta_k + \cos\varepsilon_i \cos\varepsilon_k + \cos\zeta_i \cos\zeta_k = \begin{cases} 0, i \neq k \\ 1, i = k \end{cases} \tag{S5}$$

where $\delta_{1,2,3}$ are the angles (X^*,X_H), (Y^*,X_H), (Z^*,X_H), $\varepsilon_{1,2,3}$ are the angles (X^*,Y_H), (Y^*, Y_H), (Z^*,Y_H), and $\zeta_{1,2,3}$ are the angles (X^*,Z_H), (Y^*,Z_H), (Z^*,Z_H), respectively. Deviations of the result from requirements of the equations (S5) will indicate deviations from a standard helical structure described by given parameters a and b. Also, by changing these parameters, for example, from those corresponding to α-helix to those corresponding to π- or 3_{10}- or other types

of helix, one can identify local conformational transformations in the protein.

Now we show how the angle between the helical axes of any two helices of the protein can be explicitly determined. Consider two helices, numbered $i = 1$ and $i = 2$. Following the procedures described above, we determine the angles $\zeta_{1,1}$, $\zeta_{2,1}$, $\zeta_{3,1}$, and $\zeta_{1,2}$, $\zeta_{2,2}$, $\zeta_{3,2}$ that the axes of these helices make with the axes X*, Y*, Z* of the protein coordinate system. We present each helical axis by a unit vector originating at X* = Y* = Z* = 0, and consider two planes perpendicular to these two unit vectors in a way that the tip of each unit vector is within corresponding perpendicular plane. Each plane can be presented in the three-dimensional space as:

$$A_i x + B_i y + C_i z + D_i = 0 \tag{S6}$$

where

$$A_i = \frac{1}{\cos \zeta_{2,i} \cos \zeta_{3,i}}, B_i = \frac{1}{\cos \zeta_{1,i} \cos \zeta_{3,i}}, C_i = \frac{1}{\cos \zeta_{1,i} \cos \zeta_{2,i}}, D_i = -\frac{1}{\cos \zeta_{1,i} \cos \zeta_{2,i} \cos \zeta_{3,i}}$$

The angle θ between the two helical axes is the same as the angle between the two perpendicular planes, which is given as:

$$\cos \theta = \frac{A_1 A_2 + B_1 B_2 + C_1 C_2}{\sqrt{\left(A_1^2 + B_1^2 + C_1^2\right)\left(A_2^2 + B_2^2 + C_2^2\right)}} \tag{S7}$$

Determination of angular orientation: RαATR

The best way of presenting the mode of membrane binding of a protein is providing a file in which the atom coordinates are given in an intrinsic "membrane" coordinate system Σ_m, such as a Cartesian system with its XY plane coinciding with the membrane central plane between the two lipid leaflets and with the Z axis perpendicular to the membrane surface. Here we describe how this can be achieved by segmental isotope labeling and polarized attenuated total reflection Fourier transform infrared (ATR-FTIR) spectroscopy. We consider two Cartesian coordinate systems, the "membrane" system Σ_m, as specified above, and the protein system Σ_p with axes X*Y*Z*, in which the protein atom coordinates are given. For determination of the angular orientation of the membrane-bound protein, we need the cosines of angles between the axes of the systems Σ_m and Σ_p when the protein is bound to the membrane. We used a PLA$_2$ molecule in which the N-terminal α-helix was not labeled whereas the two other helices H2 and H3, which are nearly parallel to each other, are ^{13}C-labeled. Segmental isotope labeling of PLA$_2$ resulted in a splitting of the infrared amide I band of the protein. The fact that H2 and H3 of the protein are nearly parallel to each other allows us to ascribe a common order parameter to H2/3. Spectrally separated amide I signals of the unlabeled H1 and the ^{13}C-labeled H2/3 at parallel and perpendicular polarizations of the infrared light were used to determine two order parameters, one for H1 and one for H2/3. This allowed determination of the cosines of angles between the helical axes and the membrane normal, $cos(ZZ_{H1}) = \pm\,0.489$ and $cos(ZZ_{H2}) = \pm\,0.252$, where Z_{H1} and Z_{H2} are the helical axis of H1 and an axis describing the orientation of H2/3. Because of the rotational freedom of the protein about the membrane normal (Z-axis), the plus and minus signs of the cosines are equivalent. Then, orientations of helices in the membrane system Σ_m, i.e.

131

cos(ZZ$_{H1}$) and *cos(ZZ$_{H2}$)*, were expressed through the cosines of angles between the coordinate

systems Σ_m and Σ_p and orientations of helices in the protein coordinate system Σ_p:

$$cos(ZZ_{H1}) = l_3 u_{11} + m_3 u_{21} + n_3 u_{31} \qquad \text{(S8}$$

and

$$cos(ZZ_{H2}) = l_3 u_{12} + m_3 u_{22} + n_3 u_{32} \qquad \text{(S9)}$$

where $l_3 = \cos(Z,X^*)$, $m_3 = \cos(Z,Y^*)$, $n_3 = \cos(Z,Z^*)$, $u_{1,i} = \cos(X^*,Z_{Hi})$, $u_{2,i} = \cos(Y^*,Z_{Hi})$, $u_{3,i}$

$= \cos(Z^*,Z_{Hi})$. All values of u_{ij}, i.e. the orientations of all helices relative to the axes of the

protein coordinate system Σ_p, were determined using the C_α atom coordinates of the protein, as

described in the preceding section. Equations (S8) and (S9) then contain three unknowns: l_3, m_3,

and n_3, i.e. a third equation is needed to find these cosines. The third equation is simply given by

the law of direction cosines: $l_3^2 + m_3^2 + n_3^2 = 1$. The three equations were solved together and

the values of cosines of the angles between the three axes of the protein coordinate system Σ_p and

the membrane normal were determined as $l_3 = -0.301$, $m_3 = -0.256$, $n_3 = 0.919$. These cosines

determine the orientation of the membrane-bound protein with respect to the membrane normal

with an accuracy of $\pm 180°$. This is because molecules oriented at an angle α or $\alpha \pm 180°$

generate the same infrared linear dichroic ratio and order parameter.

Our task is to obtain the coordinates of the membrane-bound protein in the "membrane"

coordinate system Σ_m. In order to do this, the other six cosines, i.e. those of the angles between

the X and Y axes and the axes X*, Y*, and Z*, were needed in addition to where l_3, m_3, and n_3.

Because of the rotational freedom of the membrane-bound protein about the Z-axis, all azimuthal

angles (determined by rotation about the Z axis) are equally valid. Therefore, one of the six cosines was arbitrarily selected [e.g., $\cos(Y,X^*) = 0.456$], and the other five cosines were found using the laws of direction cosines (equations S5). This yielded $l_1 \equiv \cos(X,X^*) = -0.837$, $l_2 \equiv \cos(Y,X^*) = 0.456$, $m_1 \equiv \cos(X,Y^*) = 0.532$, $m_2 \equiv \cos(Y,Y^*) = 0.807$, $n_1 \equiv \cos(X,Z^*) = -0.127$, $n_2 \equiv \cos(Y,Z^*) = 0.374$. The nine direction cosines between the membrane and protein coordinate systems, which were considered to be translationally co-centered, were used to transfer the protein atom coordinates from the protein system Σ_p (x_i^*, y_i^*, z_i^*) to the membrane system Σ_m (x_i, y_i, z_i):

$$
\left.\begin{aligned}
x_i &= l_1 x_i^* + m_1 y_i^* + n_1 z_i^* \\
y_i &= l_2 x_i^* + m_2 y_i^* + n_2 z_i^* \\
z_i &= l_3 x_i^* + m_3 y_i^* + n_3 z_i^*
\end{aligned}\right\}
\tag{S10}
$$

These coordinates present the structure of the membrane-bound protein with an angular orientation corresponding to the mode of membrane binding, but do not specify the translational location of the protein relative to the membrane normal (coordinate transformation was done suggesting that the systems Σ_m and Σ_p have a common origin). In order to locate the protein in the vertical dimension (the membrane normal Z-axis), we have measured membrane depth-dependent quenching of the single tryptophan (Trp[3]) of PLA$_2$, and have adjusted all z-coordinates of protein atoms by simple translation so the geometric center of the indole ring of Trp[3] was located as determined by fluorescence quenching experiments.

REFERENCES

1. Garrett, R. H. & Grisham, C. M. (1995). *Biochemistry*, Saunders College Publishing, Fort Worth.

2. Berg, O. G. & Jain, M. K. (2002). *Interfacial Enzyme Kinetics*, John Wiley & Sons, Ltd., West Sussex.

3. Jain, M. K., Rogers, J., Hendrickson, H. S. & Berg, O. G. (1993). The chemical step is not rate-limiting during the hydrolysis by phospholipase A2 of mixed micelles of phospholipid and detergent. *Biochemistry* **32**, 8360-7.

4. Boyanovsky, B. B., van der Westhuyzen, D. R. & Webb, N. R. (2005). Group V secretory phospholipase A2-modified low density lipoprotein promotes foam cell formation by a SR-A- and CD36-independent process that involves cellular proteoglycans. *J Biol Chem* **280**, 32746-52.

5. Gesquiere, L., Cho, W. & Subbaiah, P. V. (2002). Role of group IIA and group V secretory phospholipases A(2) in the metabolism of lipoproteins. Substrate specificities of the enzymes and the regulation of their activities by sphingomyelin. *Biochemistry* **41**, 4911-20.

6. Webb, N. R. (2005). Secretory phospholipase A2 enzymes in atherogenesis. *Curr Opin Lipidol* **16**, 341-4.

7. Atsumi, G., Murakami, M., Kojima, K., Hadano, A., Tajima, M. & Kudo, I. (2000). Distinct roles of two intracellular phospholipase A2s in fatty acid release in the cell death pathway. Proteolytic fragment of type IVA cytosolic phospholipase A2alpha inhibits stimulus-induced arachidonate release, whereas that of type VI Ca2+-independent phospholipase A2 augments spontaneous fatty acid release. *J Biol Chem* **275**, 18248-58.

8. Atsumi, G., Tajima, M., Hadano, A., Nakatani, Y., Murakami, M. & Kudo, I. (1998). Fas-induced arachidonic acid release is mediated by Ca2+-independent phospholipase A2 but not cytosolic phospholipase A2, which undergoes proteolytic inactivation. *J Biol Chem* **273**, 13870-7.

9. Kramer, R. M., Hession, C., Johansen, B., Hayes, G., McGray, P., Chow, E. P., Tizard, R. & Pepinsky, R. B. (1989). Structure and properties of a human non-pancreatic phospholipase A2. *J Biol Chem* **264**, 5768-75.

10. Davidson, F. F. & Dennis, E. A. (1990). Evolutionary relationships and implications for the regulation of phospholipase A2 from snake venom to human secreted forms. *J Mol Evol* **31**, 228-38.

11. Haapamaki, M. M., Gronroos, J. M., Nurmi, H., Alanen, K. & Nevalainen, T. J. (1999). Gene expression of group II phospholipase A2 in intestine in Crohn's disease. *Am J Gastroenterol* **94**, 713-20.

12. Muller, C. A., Autenrieth, I. B. & Peschel, A. (2005). Innate defenses of the intestinal epithelial barrier. *Cell Mol Life Sci* **62**, 1297-307.

13. Adamich, M. & Dennis, E. A. (1978). Exploring the action and specificity of cobra venom phospholipase A2 toward human erythrocytes, ghost membranes, and lipid mixtures. *J Biol Chem* **253**, 5121-5.

14. Adamich, M. & Dennis, E. A. (1979). Action of cobra venom phospholipase A2 toward lipids of erythrocyte membranes. *Prog Clin Biol Res* **30**, 515-21.

15. Beers, S. A., Buckland, A. G., Koduri, R. S., Cho, W., Gelb, M. H. & Wilton, D. C. (2002). The antibacterial properties of secreted phospholipases A2: a major physiological role for the group IIA enzyme that depends on the very high pI of the enzyme to allow penetration of the bacterial cell wall. *J Biol Chem* **277**, 1788-93.

16. Buckland, A. G., Heeley, E. L. & Wilton, D. C. (2000). Bacterial cell membrane hydrolysis by secreted phospholipases A(2): a major physiological role of human group IIa sPLA(2) involving both bacterial cell wall penetration and interfacial catalysis. *Biochim Biophys Acta* **1484**, 195-206.

17. Degousee, N., Ghomashchi, F., Stefanski, E., Singer, A., Smart, B. P., Borregaard, N., Reithmeier, R., Lindsay, T. F., Lichtenberger, C., Reinisch, W., Lambeau, G., Arm, J., Tischfield, J., Gelb, M. H. & Rubin, B. B. (2002). Groups IV, V, and X phospholipases A2s in human neutrophils: role in eicosanoid production and gram-negative bacterial phospholipid hydrolysis. *J Biol Chem* **277**, 5061-73.

18. Bahnson, B. J. (2005). Structure, function and interfacial allosterism in phospholipase A2: insight from the anion-assisted dimer. *Arch Biochem Biophys* **433**, 96-106.

19. Aufenanger, J., Samman, M., Quintel, M., Fassbender, K., Zimmer, W. & Bertsch, T. (2002). Pancreatic phospholipase A2 activity in acute pancreatitis: a prognostic marker for early identification of patients at risk. *Clin Chem Lab Med* **40**, 293-7.

20. Aho, V. V., Nevalainen, T. J. & Saari, K. M. (2002). Group IIA phospholipase A2 content of basal, nonstimulated and reflex tears. *Curr Eye Res* **24**, 224-7.

21. Saari, K. M., Aho, V., Paavilainen, V. & Nevalainen, T. J. (2001). Group II PLA(2) content of tears in normal subjects. *Invest Ophthalmol Vis Sci* **42**, 318-20.

22. Balboa, M. A., Balsinde, J. & Dennis, E. A. (2000). Phosphorylation of cytosolic group IV phospholipase A(2) is necessary but not sufficient for Arachidonic acid release in P388D(1) macrophages. *Biochem Biophys Res Commun* **267**, 145-8.

23.   Borsch-Haubold, A. G., Ghomashchi, F., Pasquet, S., Goedert, M., Cohen, P., Gelb, M. H. & Watson, S. P. (1999). Phosphorylation of cytosolic phospholipase A2 in platelets is mediated by multiple stress-activated protein kinase pathways. *Eur J Biochem* **265**, 195-203.

24.   de Carvalho, M. G., McCormack, A. L., Olson, E., Ghomashchi, F., Gelb, M. H., Yates, J. R., 3rd & Leslie, C. C. (1996). Identification of phosphorylation sites of human 85-kDa cytosolic phospholipase A2 expressed in insect cells and present in human monocytes. *J Biol Chem* **271**, 6987-97.

25.   Uehara, Y., Takada, S., Hirawa, N., Kawabata, Y., Nagata, T., Numabe, A., Hara, H., Kudo, I., Ikeda, T., Inoue, K. & et al. (1993). De novo synthesis of phospholipase A2 and prostacyclin production by proliferating rat smooth muscle cells. *Prostaglandins* **46**, 331-46.

26.   Murakami, M., Koduri, R. S., Enomoto, A., Shimbara, S., Seki, M., Yoshihara, K., Singer, A., Valentin, E., Ghomashchi, F., Lambeau, G., Gelb, M. H. & Kudo, I. (2001). Distinct arachidonate-releasing functions of mammalian secreted phospholipase A2s in human embryonic kidney 293 and rat mastocytoma RBL-2H3 cells through heparan sulfate shuttling and external plasma membrane mechanisms. *J Biol Chem* **276**, 10083-96.

27.   Enomoto, A., Murakami, M., Valentin, E., Lambeau, G., Gelb, M. H. & Kudo, I. (2000). Redundant and segregated functions of granule-associated heparin-binding group II subfamily of secretory phospholipases A2 in the regulation of degranulation and prostaglandin D2 synthesis in mast cells. *J Immunol* **165**, 4007-14.

28.   Balboa, M. A., Shirai, Y., Gaietta, G., Ellisman, M. H., Balsinde, J. & Dennis, E. A. (2003). Localization of group V phospholipase A2 in caveolin-enriched granules in activated P388D1 macrophage-like cells. *J Biol Chem* **278**, 48059-65.

29.   De Marino, V., Gentile, M., Granata, F., Marone, G. & Triggiani, M. (1999). Secretory phospholipase A2: a putative mediator of airway inflammation. *Int Arch Allergy Immunol* **118**, 200-1.

30.   Mitsuishi, M., Masuda, S., Kudo, I. & Murakami, M. (2006). Group V and X secretory phospholipase A2 prevents adenoviral infection in mammalian cells. *Biochem J* **393**, 97-106.

31.   Aho, H. J., Grenman, R., Sipila, J., Peuravuori, H., Hartikainen, J. & Nevalainen, T. J. (1997). Group II phospholipase A2 in nasal fluid, mucosa and paranasal sinuses. *Acta Otolaryngol* **117**, 860-3.

32.   Nevalainen, T. J., Gronroos, J. M. & Kallajoki, M. (1995). Expression of group II phospholipase A2 in the human gastrointestinal tract. *Lab Invest* **72**, 201-8.

33. Gurrieri, S., Furstenberger, G., Schadow, A., Haas, U., Singer, A. G., Ghomashchi, F., Pfeilschifter, J., Lambeau, G., Gelb, M. H. & Kaszkin, M. (2003). Differentiation-dependent regulation of secreted phospholipases A2 in murine epidermis. *J Invest Dermatol* **121**, 156-64.

34. Kim, D. K., Kudo, I. & Inoue, K. (1988). Detection in human platelets of phospholipase A2 activity which preferentially hydrolyzes an arachidonoyl residue. *J Biochem (Tokyo)* **104**, 492-4.

35. Kudo, I. (1991). [Mammalian cellular phospholipases A2 and their physiological roles]. *Yakugaku Zasshi* **111**, 488-98.

36. Masuda, S., Murakami, M., Matsumoto, S., Eguchi, N., Urade, Y., Lambeau, G., Gelb, M. H., Ishikawa, Y., Ishii, T. & Kudo, I. (2004). Localization of various secretory phospholipase A2 enzymes in male reproductive organs. *Biochim Biophys Acta* **1686**, 61-76.

37. Schror, K. (1992). Role of prostaglandins in the cardiovascular effects of bradykinin and angiotensin-converting enzyme inhibitors. *Journal of Cardiovascular Pharmacology* **20**, S68-73.

38. Clark, M. A., Bomalaski, J. S., Conway, T. M., Cook, M., Dispoto, J., Mong, S., Shorn, R. G., Stadell, J., Webb, L. & Crooke, S. T. (1990). The role of phospholipase A2 activating protein (PLAP) in regulating prostanoid production in smooth muscle and endothelial cells following leukotriene D4 treatment. *Adv Exp Med Biol* **275**, 125-44.

39. Jaulmes, A., Janvier, B., Andreani, M. & Raymondjean, M. (2005). Autocrine and paracrine transcriptional regulation of type IIA secretory phospholipase A2 gene in vascular smooth muscle cells. *Arterioscler Thromb Vasc Biol* **25**, 1161-7.

40. Morin, R. J. (1980). The role of phospholipids in platelet function. *Annals of clinical and laboratory science* **10**, 463-73.

41. Asaoka, Y., Yoshida, K., Sasaki, Y., Nishizuka, Y., Murakami, M., Kudo, I. & Inoue, K. (1993). Possible role of mammalian secretory group II phospholipase A2 in T-lymphocyte activation: implication in propagation of inflammatory reaction. *Proc Natl Acad Sci U S A* **90**, 716-9.

42. Gilroy, D. W., Newson, J., Sawmynaden, P., Willoughby, D. A. & Croxtall, J. D. (2004). A novel role for phospholipase A2 isoforms in the checkpoint control of acute inflammation. *Faseb J* **18**, 489-98.

43. Calabrese, C., Triggiani, M., Marone, G. & Mazzarella, G. (2000). Arachidonic acid metabolism in inflammatory cells of patients with bronchial asthma. *Allergy* **55 Suppl 61**, 27-30.

44. Hara, S., Kudo, I., Chang, H. W., Matsuta, K., Miyamoto, T. & Inoue, K. (1989). Purification and characterization of extracellular phospholipase A2 from human synovial fluid in rheumatoid arthritis. *J Biochem (Tokyo)* **105**, 395-9.

45. Haapamaki, M. M., Gronroos, J. M., Nurmi, H., Soderlund, K., Peuravuori, H., Alanen, K. & Nevalainen, T. J. (1998). Elevated group II phospholipase A2 mass concentration in serum and colonic mucosa in Crohn's disease. *Clin Chem Lab Med* **36**, 751-5.

46. Lilja, I., Gustafson-Svard, C., Franzen, L., Sjodahl, R., Andersen, S. & Johansen, B. (2000). Presence of group IIa secretory phospholipase A_2 in mast cells and macrophages in normal human ileal submucosa and in Crohn's disease. *Clin Chem Lab Med* **38**, 1231-6.

47. Koyama, M., Ito, S., Nakajima, A., Shimoya, K., Azuma, C., Suehara, N., Murata, Y. & Tojo, H. (2000). Elevations of group II phospholipase A2 concentrations in serum and amniotic fluid in association with preterm labor. *Am J Obstet Gynecol* **183**, 1537-43.

48. Dong, Q., Patel, M., Scott, K. F., Graham, G. G., Russell, P. J. & Sved, P. (2005). Oncogenic action of phospholipase A(2) in prostate cancer. *Cancer Lett*.

49. Sved, P., Scott, K. F., McLeod, D., King, N. J., Singh, J., Tsatralis, T., Nikolov, B., Boulas, J., Nallan, L., Gelb, M. H., Sajinovic, M., Graham, G. G., Russell, P. J. & Dong, Q. (2004). Oncogenic action of secreted phospholipase A2 in prostate cancer. *Cancer Res* **64**, 6934-40.

50. Sun, G. Y., Xu, J., Jensen, M. D. & Simonyi, A. (2004). Phospholipase A2 in the central nervous system: implications for neurodegenerative diseases. *J Lipid Res* **45**, 205-13.

51. Dennis, E. A. (2000). Phospholipase A2 in eicosanoid generation. *Am J Respir Crit Care Med* **161**, S32-5.

52. Singer, A. G., Ghomashchi, F., Le Calvez, C., Bollinger, J., Bezzine, S., Rouault, M., Sadilek, M., Nguyen, E., Lazdunski, M., Lambeau, G. & Gelb, M. H. (2002). Interfacial kinetic and binding properties of the complete set of human and mouse groups I, II, V, X, and XII secreted phospholipases A2. *J Biol Chem* **277**, 48535-49.

53. Murakami, M., Masuda, S., Shimbara, S., Bezzine, S., Lazdunski, M., Lambeau, G., Gelb, M. H., Matsukura, S., Kokubu, F., Adachi, M. & Kudo, I. (2003). Cellular Arachidonate-releasing Function of Novel Classes of Secretory Phospholipase A2s (Groups III and XII). *J. Biol. Chem.* **278**, 10657-10667.

54. Renetseder, R., Brunie, S., Dijkstra, B. W., Drenth, J. & Sigler, P. B. (1985). A comparison of the crystal structures of phospholipase A2 from bovine pancreas and Crotalus atrox venom. *J Biol Chem* **260**, 11627-34.

55. Berg, O. G., Rogers, J., Yu, B. Z., Yao, J., Romsted, L. S. & Jain, M. K. (1997). Thermodynamic and kinetic basis of interfacial activation: resolution of binding and allosteric effects on pancreatic phospholipase A2 at zwitterionic interfaces. *Biochemistry* **36**, 14512-30.

56. Tatulian, S. A. (2003). Structural effects of covalent inhibition of phospholipase A2 suggest allosteric coupling between membrane binding and catalytic sites. *Biophys J* **84**, 1773-83.

57. Snitko, Y., Koduri, R. S., Han, S. K., Othman, R., Baker, S. F., Molini, B. J., Wilton, D. C., Gelb, M. H. & Cho, W. (1997). Mapping the interfacial binding surface of human secretory group IIa phospholipase A2. *Biochemistry* **36**, 14325-33.

58. Verheij, H. M., Slotboom, A. J. & Haas, G. H. d. (1981). Structure and function of phospholiphase A2. In *Reviews of Physiology, Biochemistry and Pharmacology*, Vol. 91, pp. 91-203. Publisher: Springer Berlin / Heidelberg.

59. Yu, B. Z., Rogers, J., Nicol, G. R., Theopold, K. H., Seshadri, K., Vishweshwara, S. & Jain, M. K. (1998). Catalytic significance of the specificity of divalent cations as KS* and kcat* cofactors for secreted phospholipase A2. *Biochemistry* **37**, 12576-87.

60. Berg, O. G., Gelb, M. H., Tsai, M. D. & Jain, M. K. (2001). Interfacial enzymology: the secreted phospholipase A(2)-paradigm. *Chem Rev* **101**, 2613-54.

61. Hoyrup, P., Mouritsen, O. G. & Jorgensen, K. (2001). Phospholipase A(2) activity towards vesicles of DPPC and DMPC-DSPC containing small amounts of SMPC. *Biochim Biophys Acta* **1515**, 133-43.

62. He, Q. & Li, J. (2003). Dynamic and morphological investigation of phospholipid monolayer hydrolysis by phospholipase C. *Biochem Biophys Res Commun* **300**, 541-5.

63. Huang, H. W., Goldberg, E. M. & Zidovetzki, R. (1996). Ceramide induces structural defects into phosphatidylcholine bilayers and activates phospholipase A2. *Biochem Biophys Res Commun* **220**, 834-8.

64. Ho, C. L., Tsai, I. H. & Lee, C. Y. (1986). The role of enzyme activity and charge properties on the presynaptic neurotoxicity and the contracture-inducing activity of snake venom phospholipases A2. *Toxicon* **24**, 337-45.

65. Burack, W. R., Yuan, Q. & Biltonen, R. L. (1993). Role of lateral phase separation in the modulation of phospholipase A2 activity. *Biochemistry* **32**, 583-9.

66. Han, S. K., Yoon, E. T., Scott, D. L., Sigler, P. B. & Cho, W. (1997). Structural aspects of interfacial adsorption. A crystallographic and site-directed mutagenesis study of the phospholipase A2 from the venom of *Agkistrodon piscivorus piscivorus*. *J Biol Chem* **272**, 3573-82.

139

67. Janssen, M. J., Burghout, P. J., Verheij, H. M., Slotboom, A. J. & Egmond, M. R. (1999). Introduction of a C-terminal aromatic sequence from snake venom phospholipases A2 into the porcine pancreatic isozyme dramatically changes the interfacial kinetics. *Eur J Biochem* **263**, 782-8.

68. Jerala, R., Almeida, P. F., Ye, Q., Biltonen, R. L. & Rule, G. S. (1996). 1H, 15N and 13C resonance assignments and secondary structure of group II phospholipase A2 from *Agkistrodon piscivorus piscivorus*: presence of an amino-terminal helix in solution. *J Biomol NMR* **7**, 107-120.

69. van den Berg, B., Tessari, M., Boelens, R., Dijkman, R., de Haas, G. H., Kaptein, R. & Verheij, H. M. (1995). NMR structures of phospholipase A2 reveal conformational changes during interfacial activation. *Nat Struct Biol* **2**, 402-6.

70. Apitz-Castro, R., Jain, M. K. & De Haas, G. H. (1982). Origin of the latency phase during the action of phospholipase A2 on unmodified phosphatidylcholine vesicles. *Biochim Biophys Acta* **688**, 349-56.

71. Bayburt, T., Yu, B. Z., Lin, H. K., Browning, J., Jain, M. K. & Gelb, M. H. (1993). Human nonpancreatic secreted phospholipase A2: interfacial parameters, substrate specificities, and competitive inhibitors. *Biochemistry* **32**, 573-82.

72. Yu, B. Z., Rogers, J., Tsai, M. D., Pidgeon, C. & Jain, M. K. (1999). Contributions of residues of pancreatic phospholipase A2 to interfacial binding, catalysis, and activation. *Biochemistry* **38**, 4875-84.

73. Baker, S. F., Othman, R. & Wilton, D. C. (1998). Tryptophan-containing mutant of human (group IIa) secreted phospholipase A2 has a dramatically increased ability to hydrolyze phosphatidylcholine vesicles and cell membranes. *Biochemistry* **37**, 13203-11.

74. Beers, S. A., Buckland, A. G., Giles, N., Gelb, M. H. & Wilton, D. C. (2003). Effect of tryptophan insertions on the properties of the human group IIA phospholipase A2: mutagenesis produces an enzyme with characteristics similar to those of the human group V phospholipase A2. *Biochemistry* **42**, 7326-38.

75. Bezzine, S., Bollinger, J. G., Singer, A. G., Veatch, S. L., Keller, S. L. & Gelb, M. H. (2002). On the binding preference of human groups IIA and X phospholipases A2 for membranes with anionic phospholipids. *J Biol Chem* **277**, 48523-34.

76. Liu, X., Zhu, H., Huang, B., Rogers, J., Yu, B. Z., Kumar, A., Jain, M. K., Sundaralingam, M. & Tsai, M. D. (1995). Phospholipase A2 engineering. Probing the structural and functional roles of N-terminal residues with site-directed mutagenesis, X-ray, and NMR. *Biochemistry* **34**, 7322-34.

77.   Cha, S. S., Lee, D., Adams, J., Kurdyla, J. T., Jones, C. S., Marshall, L. A., Bolognese, B., Abdel-Meguid, S. S. & Oh, B. H. (1996). High-resolution X-ray crystallography reveals precise binding interactions between human nonpancreatic secreted phospholipase A2 and a highly potent inhibitor (FPL67047XX). *J Med Chem* **39**, 3878-81.

78.   Hansford, K. A., Reid, R. C., Clark, C. I., Tyndall, J. D., Whitehouse, M. W., Guthrie, T., McGeary, R. P., Schafer, K., Martin, J. L. & Fairlie, D. P. (2003). D-Tyrosine as a chiral precusor to potent inhibitors of human nonpancreatic secretory phospholipase A2 (IIa) with antiinflammatory activity. *Chembiochem* **4**, 181-5.

79.   Plesniak, L. A., Yu, L. & Dennis, E. A. (1995). Conformation of micellar phospholipid bound to the active site of phospholipase A2. *Biochemistry* **34**, 4943-51.

80.   van den Berg, B., Tessari, M., Boelens, R., Dijkman, R., Kaptein, R., de Haas, G. H. & Verheij, H. M. (1995). Solution structure of porcine pancreatic phospholipase A2 complexed with micelles and a competitive inhibitor. *J Biomol NMR* **5**, 110-21.

81.   Qin, S., Pande, A. H., Nemec, K. N., He, X. & Tatulian, S. A. (2005). Evidence for the regulatory role of the N-terminal helix of secretory phospholipase A(2) from studies on native and chimeric proteins. *J Biol Chem* **280**, 36773-83.

82.   Tatulian, S. A., Qin, S., Pande, A. H. & He, X. (2005). Positioning membrane proteins by novel protein engineering and biophysical approaches. *J Mol Biol* **351**, 939-47.

83.   Qin, S., Pande, A. H., Nemec, K. N. & Tatulian, S. A. (2004). The N-terminal alpha-helix of pancreatic phospholipase A2 determines productive-mode orientation of the enzyme at the membrane surface. *J Mol Biol* **344**, 71-89.

84.   Othman, R., Baker, S., Li, Y., Worrall, A. F. & Wilton, D. C. (1996). Human non-pancreatic (group II) secreted phospholipase A2 expressed from a synthetic gene in Escherichia coli: characterisation of N-terminal mutants. *Biochim Biophys Acta* **1303**, 92-102.

85.   Golding, C., Senior, S., Wilson, M. T. & O'Shea, P. (1996). Time Resolution of Binding and Membrane Insertion of a Mitochondrial Signal Peptide: Correlation with Structural Changes and Evidence for Cooperativity. *Biochemistry* **35**, 10931-10937.

86.   Wall, J., Golding, C. A., Van Veen, M. & O'Shea, P. (1995). The use of fluoresceinphosphatidylethanolamine (FPE) as a real-time probe for peptide-membrane interactions. *Molecular Membrane Biology* **12**, 183-92.

87.   Lakowicz, J. R. (1999). *Principles of fluorescence spectroscopy*. 2nd edit, Kluwer Academic/Plenum, New York.

88.   McIntosh, T. J. & Holloway, P. W. (1987). Determination of the depth of bromine atoms in bilayers formed from bromolipid probes. *Biochemistry* **26**, 1783-1788.

89.   Burack, W. R. & Biltonen, R. L. (1994). Lipid bilayer heterogeneities and modulation of phospholipase A2 activity. *Chem Phys Lipids* **73**, 209-22.

90.   Burack, W. R., Dibble, A. R., Allietta, M. M. & Biltonen, R. L. (1997). Changes in vesicle morphology induced by lateral phase separation modulate phospholipase A2 activity. *Biochemistry* **36**, 10551-7.

91.   Hønger, T., Jorgensen, K., Stokes, D., Biltonen, R. L. & Mouritsen, O. G. (1997). Phospholipase A2 activity and physical properties of lipid-bilayer substrates. *Methods Enzymol* **286**, 168-90.

92.   Burack, W. R., Gadd, M. E. & Biltonen, R. L. (1995). Modulation of phospholipase A2: identification of an inactive membrane-bound state. *Biochemistry* **34**, 14819-28.

93.   Leidy, C., Linderoth, L., Andresen, T. L., Mouritsen, O. G., Jorgensen, K. & Peters, G. H. (2006). Domain-Induced Activation of Human Phospholipase A2 Type IIA: Local versus Global Lipid Composition. *Biophys. J.* **90**, 3165-3175.

94.   Canaan, S., Nielsen, R., Ghomashchi, F., Robinson, B. H. & Gelb, M. H. (2002). Unusual mode of binding of human group IIA secreted phospholipase A2 to anionic interfaces as studied by continuous wave and time domain electron paramagnetic resonance spectroscopy. *J Biol Chem* **277**, 30984-90.

95.   de Sousa, M. V., Morhy, L., Arni, R. K., Ward, R. J., Diaz, C. & Gutierrez, J. M. (1998). Amino acid sequence of a myotoxic Lys49-phospholipase A2 homologue from the venom of Cerrophidion (Bothrops) godmani. *Biochim Biophys Acta* **1384**, 204-8.

96.   Diraviyam, K. & Murray, D. (2006). Computational analysis of the membrane association of group IIA secreted phospholipases A2: a differential role for electrostatics. *Biochemistry* **45**, 2584-98.

97.   Gelb, M. H., Cho, W. & Wilton, D. C. (1999). Interfacial binding of secreted phospholipases A(2): more than electrostatics and a major role for tryptophan. *Curr Opin Struct Biol* **9**, 428-32.

98.   Chothia, C. (1976). The nature of the accessible and buried surfaces in proteins. *J Mol Biol* **105**, 1-12.

99.   Kutateladze, T. G., Capelluto, D. G. S., Ferguson, C. G., Cheever, M. L., Kutateladze, A. G., Prestwich, G. D. & Overduin, M. (2004). Multivalent Mechanism of Membrane Insertion by the FYVE Domain. *J. Biol. Chem.* **279**, 3050-3057.

100. Malmberg, N. J. & Falke, J. J. (2005). USE OF EPR POWER SATURATION TO ANALYZE THE MEMBRANE-DOCKING GEOMETRIES OF PERIPHERAL PROTEINS: Applications to C2 Domains. *Annual Review of Biophysics and Biomolecular Structure* **34**, 71-90.

101. Nielsen, R. D., Che, K., Gelb, M. H. & Robinson, B. H. (2005). A Ruler for Determining the Position of Proteins in Membranes. *J. Am. Chem. Soc.* **127**, 6430-6442.

102. Pande, A. H., Qin, S. & Tatulian, S. A. (2005). Membrane fluidity is a key modulator of membrane binding, insertion, and activity of 5-lipoxygenase. *Biophys J* **88**, 4084-94.

103. Rufener, E., Frazier, A. A., Wieser, C. M., Hinderliter, A. & Cafiso, D. S. (2005). Membrane-Bound Orientation and Position of the Synaptotagmin C2B Domain Determined by Site-Directed Spin Labeling. *Biochemistry* **44**, 18-28.

104. Scott, D. L., White, S. P., Browning, J. L., Rosa, J. J., Gelb, M. H. & Sigler, P. B. (1991). Structures of free and inhibited human secretory phospholipase A2 from inflammatory exudate. *Science* **254**, 1007-10.

105. van den Berg, B., Tessari, M., de Haas, G. H., Verheij, H. M., Boelens, R. & Kaptein, R. (1995). Solution structure of porcine pancreatic phospholipase A2. *Embo J* **14**, 4123-31.

106. Peters, A. R., Dekker, N., van den Berg, L., Boelens, R., Kaptein, R., Slotboom, A. J. & de Haas, G. H. (1992). Conformational changes in phospholipase A2 upon binding to micellar interfaces in the absence and presence of competitive inhibitors. A 1H and 15N NMR study. *Biochemistry* **31**, 10024-30.

107. Cooper, T. M. & Woody, R. W. (1990). The effect of conformation on the CD of interacting helices: a theoretical study of tropomyosin. *Biopolymers* **30**, 657-76.

108. Zhou, N. E., Kay, C. M. & Hodges, R. S. (1992). Synthetic model proteins: the relative contribution of leucine residues at the nonequivalent positions of the 3-4 hydrophobic repeat to the stability of the two-stranded alpha-helical coiled-coil. *Biochemistry* **31**, 5739-46.

109. Kelly, S. M. & Price, N. C. (1997). The application of circular dichroism to studies of protein folding and unfolding. *Biochim Biophys Acta* **1338**, 161-85.

110. Luo, P. & Baldwin, R. L. (1997). Mechanism of Helix Induction by Trifluoroethanol: A Framework for Extrapolating the Helix-Forming Properties of Peptides from Trifluoroethanol/Water Mixtures Back to Water. *Biochemistry* **36**, 8413-8421.

111. Rohl, C. A. & Baldwin, R. L. (1997). Comparison of NH Exchange and Circular Dichroism as Techniques for Measuring the Parameters of the Helix-Coil Transition in Peptides. *Biochemistry* **36**, 8435-8442.

112.   Venyaminov, S. Y. & Yang, J. T. (1996). Determination of protein secondary structure. In *Circular Dichroism and the Conformational Analysis of Biomolecules* (Fasman, G. D., ed.), pp. 69-107. Plenum Press, New York and London.

113.   Arni, R. K. & Ward, R. J. (1996). Phospholipase A2--a structural review. *Toxicon* **34**, 827-41.

114.   Scott, D. L. & Sigler, P. B. (1994). Structure and catalytic mechanism of secretory phospholipases A2. *Adv Protein Chem* **45**, 53-88.

115.   Sreerama, N., Venyaminov, S. Y. & Woody, R. W. (1999). Estimation of the number of alpha-helical and beta-strand segments in proteins using circular dichroism spectroscopy. *Protein Sci* **8**, 370-80.

116.   Tatulian, S. A. (2003). Attenuated total reflection Fourier transform infrared spectroscopy: a method of choice for studying membrane proteins and lipids. *Biochemistry* **42**, 11898-907.

117.   Edwards, S. H., Thompson, D., Baker, S. F., Wood, S. P. & Wilton, D. C. (2002). The crystal structure of the H48Q active site mutant of human group IIA secreted phospholipase A2 at 1.5 A resolution provides an insight into the catalytic mechanism. *Biochemistry* **41**, 15468-76.

118.   Tatulian, S. A. (2001). Toward understanding interfacial activation of secretory phospholipase A2 (PLA2): membrane surface properties and membrane-induced structural changes in the enzyme contribute synergistically to PLA2 activation. *Biophys J* **80**, 789-800.

119.   Tatulian, S. A., Biltonen, R. L. & Tamm, L. K. (1997). Structural changes in a secretory phospholipase A2 induced by membrane binding: a clue to interfacial activation? *J Mol Biol* **268**, 809-15.

120.   Nemethy, G., Phillips, D. C., Leach, S. J. & Scheraga, H. A. (1967). A second right-handed helical structure with the parameters of the Pauling-Corey alpha-helix. *Nature* **214**, 363-5.

121.   Barnett, S. M., Edwards, C. M., Butler, I. S. & Levin, I. W. (1997). Pressure-Induced Transmembrane α_{II} to α_I-Helical Conversion in Bacteriorhodopsin: An Infrared Spectroscopic Study. *J. Phys. Chem. B* **101**, 9421-9424.

122.   Dwivedi, A. M. & Krimm, S. (1984). Vibrational analysis of peptides, polypeptides, and proteins. XVIII. Conformational sensitivity of the alpha-helix spectrum: alpha I- and alpha II-poly(L-alanine). *Biopolymers* **23**, 923-43.

123.   Rothschild, K. J. & Clark, N. A. (1979). Anomalous amide I infrared absorption of purple membrane. *Science* **204**, 311-2.

124. Tatulian, S. A., Cortes, D. M. & Perozo, E. (1998). Structural dynamics of the Streptomyces lividans K+ channel (SKC1): secondary structure characterization from FTIR spectroscopy. *FEBS Lett* **423**, 205-12.

125. Tatulian, S. A., Jones, L. R., Reddy, L. G., Stokes, D. L. & Tamm, L. K. (1995). Secondary structure and orientation of phospholamban reconstituted in supported bilayers from polarized attenuated total reflection FTIR spectroscopy. *Biochemistry* **34**, 4448-56.

126. Fringeli, U. P. (1993). In situ infrared attenuated total reflection membrane spectroscopy. In *Internal Reflection Spectroscopy: Theory and Application* (Mirabella, F. M., ed.), pp. 255-324. Marcel Dekker, New York.

127. Axelsen, P. H., Kaufman, B. K., McElhaney, R. N. & Lewis, R. N. (1995). The infrared dichroism of transmembrane helical polypeptides. *Biophsical Journal* **69**, 2770-2718.

128. Schwede, T., Kopp, J., Guex, N. & Peitsch, M. C. (2003). SWISS-MODEL: An automated protein homology-modeling server. *Nucleic Acids Res* **31**, 3381-5.

129. Jain, M. K. & Vaz, W. L. (1987). Dehydration of the lipid-protein microinterface on binding of phospholipase A2 to lipid bilayers. *Biochim Biophys Acta* **905**, 1-8.

130. Jain, M. K. & Berg, O. G. (1989). The kinetics of interfacial catalysis by phospholipase A2 and regulation of interfacial activation: hopping versus scooting. *Biochim Biophys Acta* **1002**, 127-56.

131. Berg, O. G., Yu, B. Z., Rogers, J. & Jain, M. K. (1991). Interfacial catalysis by phospholipase A2: determination of the interfacial kinetic rate constants. *Biochemistry* **30**, 7283-97.

132. Leidy, C., Mouritsen, O. G., Jorgensen, K. & Peters, G. H. (2004). Evolution of a rippled membrane during phospholipase A2 hydrolysis studied by time-resolved AFM. *Biophys J* **87**, 408-18.

133. Sanchez, S. A., Bagatolli, L. A., Gratton, E. & Hazlett, T. L. (2002). A Two-Photon View of an Enzyme at Work: Crotalus atrox Venom PLA2 Interaction with Single-Lipid and Mixed-Lipid Giant Unilamellar Vesicles. *Biophys. J.* **82**, 2232-2243.

134. Volwerk, J. J., Jost, P. C., de Haas, G. H. & Griffith, O. H. (1986). Activation of porcine pancreatic phospholipase A2 by the presence of negative charges at the lipid-water interface. *Biochemistry* **25**, 1726-33.

135. Scott, D. L., White, S. P., Otwinowski, Z., Yuan, W., Gelb, M. H. & Sigler, P. B. (1990). Interfacial catalysis: the mechanism of phospholipase A2. *Science* **250**, 1541-6.

136. Koduri, R. S., Baker, S. F., Snitko, Y., Han, S. K., Cho, W., Wilton, D. C. & Gelb, M. H. (1998). Action of human group IIa secreted phospholipase A2 on cell membranes.

Vesicle but not heparinoid binding determines rate of fatty acid release by exogenously added enzyme. *J Biol Chem* **273**, 32142-53.

137. Snitko, Y., Han, S. K., Lee, B. I. & Cho, W. (1999). Differential interfacial and substrate binding modes of mammalian pancreatic phospholipases A2: a comparison among human, bovine, and porcine enzymes. *Biochemistry* **38**, 7803-10.

138. Chang, L. S., Kuo, K. W. & Chang, C. C. (1993). Identification of functional involvement of tryptophan residues in phospholipase A2 from Naja naja atra (Taiwan cobra) snake venom. *Biochim Biophys Acta* **1202**, 216-20.

139. Berg, O. G., Yu, B. Z., Chang, C., Koehler, K. A. & Jain, M. K. (2004). Cooperative binding of monodisperse anionic amphiphiles to the i-face: phospholipase A2-paradigm for interfacial binding. *Biochemistry* **43**, 7999-8013.

140. Gadd, M. E. & Biltonen, R. L. (2000). Characterization of the interaction of phospholipase A(2) with phosphatidylcholine-phosphatidylglycerol mixed lipids. *Biochemistry* **39**, 9623-31.

141. Chandra, V., Jasti, J., Kaur, P., Srinivasan, A., Betzel, C. & Singh, T. P. (2002). Structural basis of phospholipase A2 inhibition for the synthesis of prostaglandins by the plant alkaloid aristolochic acid from a 1.7 A crystal structure. *Biochemistry* **41**, 10914-9.

142. Yu, B. Z., Poi, M. J., Ramagopal, U. A., Jain, R., Ramakumar, S., Berg, O. G., Tsai, M. D., Sekar, K. & Jain, M. K. (2000). Structural basis of the anionic interface preference and kcat* activation of pancreatic phospholipase A2. *Biochemistry* **39**, 12312-23.

143. Jain, M. K., Rogers, J., Jahagirdar, D. V., Marecek, J. F. & Ramirez, F. (1986). Kinetics of interfacial catalysis by phospholipase A2 in intravesicle scooting mode, and heterofusion of anionic and zwitterionic vesicles. *Biochim Biophys Acta* **860**, 435-47.

144. Zhou, F. & Schulten, K. (1996). Molecular dynamics study of phospholipase A2 on a membrane surface. *Proteins: Structure, Function, and Genetics* **25**, 12-27.

145. Wery, J. P., Schevitz, R. W., Clawson, D. K., Bobbitt, J. L., Dow, E. R., Gamboa, G., Goodson Jr, T., Hermann, R. B., Kramer, R. M., McClure, D. B., Mihelich, E. D., Putnam, J. E., Sharp, J. D., Stark, D. H., Teater, C., Warrick, M. W. & Jones, N. D. (1991). Structure of recombinant human rheumatoid arthritic synovial fluid phospholipase A2 at 2.2 A resolution. *Nature* **352**, 79.

146. Chen, J., Anderson, J. B., DeWeese-Scott, C., Fedorova, N. D., Geer, L. Y., He, S., Hurwitz, D. I., Jackson, J. D., Jacobs, A. R., Lanczycki, C. J., Liebert, C. A., Liu, C., Madej, T., Marchler-Bauer, A., Marchler, G. H., Mazumder, R., Nikolskaya, A. N., Rao, B. S., Panchenko, A. R., Shoemaker, B. A., Simonyan, V., Song, J. S., Thiessen, P. A.,

Vasudevan, S., Wang, Y., Yamashita, R. A., Yin, J. J. & Bryant, S. H. (2003). MMDB: Entrez's 3D-structure database. *Nucl. Acids Res.* **31**, 474-477.

147. Maliwal, B. P., Yu, B. Z., Szmacinski, H., Squier, T., van Binsbergen, J., Slotboom, A. J. & Jain, M. K. (1994). Functional significance of the conformational dynamics of the N-terminal segment of secreted phospholipase A_2 at the interface. *Biochemistry* **33**, 4509-16.

148. Heymann, J. B., Zakharov, S. D., Zhang, Y. L. & Cramer, W. A. (1996). Characterization of Electrostatic and Nonelectrostatic Components of Protein-Membrane Binding Interactions. *Biochemistry* **35**, 2717-2725.

149. Koppaka, V. & Lentz, B. R. (1996). Binding of bovine factor Vα to phosphatidylcholine membranes. *Biophys J* **70**, 2930-2937.

150. Seelig, J., Nebel, S., P.Ganz & Bruns, C. (1993). Electrostatic and nonpolar peptide-membrane interactions. Lipid binding and functional properties of somatostatin analogues of charge z = +1 to z = +3. *Biochemistry* **32**, 9714-21.

151. Sumandea, M., Das, S., Sumandea, C. & Cho, W. (1999). Roles of aromatic residues in high interfacial activity of Naja naja atra phospholipase A2. *Biochemistry* **38**, 16290-7.

152. Tatulian, S. A. (2002). Quantitative Characterization of Membrane Binding of Peripheral Proteins by Spin-Label EPR Spectroscopy. *J. Phys. Chem. B* **106**, 8870-8877.

153. Vogel, M., Münster, C., Fenzl, W. & Salditt, T. (2000). Thermal Unbinding of Highly Oriented Phospholipid Membranes. *Physical Review Letters* **84**, 390.

154. Caputo, G. A. & London, E. (2004). Position and Ionization State of Asp in the Core of Membrane-Inserted α Helices Control Both the Equilibrium between Transmembrane and Nontransmembrane Helix Topography and Transmembrane Helix Positioning. *Biochemistry* **43**, 8794-8806.

155. Caputo, G. A. & London, E. (2003). Using a novel dual fluorescence quenching assay for measurement of tryptophan depth within lipid bilayers to determine hydrophobic alpha-helix locations within membranes. *Biochemistry* **42**, 3265-74.

156. Ladokhin, A. S. (1997). Distribution analysis of depth-dependent fluorescence quenching in membranes: a practical guide. *Methods Enzymol* **278**, 462-473.

157. London, E. & Ladokhin, A. S. (2002). Measuring the depth of amino acid residues in membrane-inserted peptides by fluorescence quenching. *Curr. Topics Membr* **52**, 89-115.

158. Marsh, D. (1999). Quantitation of Secondary Structure in ATR Infrared Spectroscopy. *Biophys. J.* **77**, 2630-2637.

159.   Axelsen, P. H. & Citra, M. J. (1996). Orientational order determination by internal reflection infrared spectroscopy. *Prog Biophys Mol Biol* **66**, 227-53.

160.   Marsh, D. (2004). Infrared Dichroism of Isotope-edited α-Helices and β-Sheets. *Journal of Molecular Biology* **338**, 353-367.

161.   Marsh, D., Muller, M. & Schmitt, F.-J. (2000). Orientation of the Infrared Transition Moments for an alpha -Helix. *Biophys. J.* **78**, 2499-2510.